Search for anomalous couplings of Higgs bosons using events with electrons/muons and tau leptons in proton-proton collisions at $\sqrt{s} = 13$ TeV at the Large Hadron Collider

by

Tyler Mitchell

B.S., Kansas State University, 2012

AN ABSTRACT OF A DISSERTATION

submitted in partial fulfillment of the
requirements for the degree

DOCTOR OF PHILOSOPHY

Department of Physics
College of Arts and Sciences

KANSAS STATE UNIVERSITY
Manhattan, Kansas

2021

Abstract

A study of the Higgs boson coupling to gauge bosons is presented using the $\tau_e\tau_h$ and $\tau_\mu\tau_h$ decay channels. The effects of CP-violation and anomalous couplings in Higgs gluon-gluon fusion and vector boson fusion production mechanisms are analyzed using machine learning and matrix element techniques. These techniques take advantage of the correlations present between jets produced in association with the Higgs boson to produce the most sensitive analysis to date. The analysis is conducted using data collected by the CMS experiment at 13 TeV center-of-mass energy corresponding to an integrated luminosity of 139 fb^{-1}.

Search for anomalous couplings of Higgs bosons using events with electrons/muons and tau leptons in proton-proton collisions at $\sqrt{s} = 13$ TeV at the Large Hadron Collider

by

Tyler Mitchell

B.S., Kansas State University, 2012

A DISSERTATION

submitted in partial fulfillment of the
requirements for the degree

DOCTOR OF PHILOSOPHY

Department of Physics
College of Arts and Sciences

KANSAS STATE UNIVERSITY
Manhattan, Kansas

2021

Approved by:

Major Professor
Andrew Ivanov

Copyright

Abstract

A study of the Higgs boson coupling to gauge bosons is presented using the $\tau_e\tau_h$ and $\tau_\mu\tau_h$ decay channels. The effects of CP-violation and anomalous couplings in Higgs gluon-gluon fusion and vector boson fusion production mechanisms are analyzed using machine learning and matrix element techniques. These techniques take advantage of the correlations present between jets produced in association with the Higgs boson to produce the most sensitive analysis to date. The analysis is conducted using data collected by the CMS experiment at 13 TeV center-of-mass energy corresponding to an integrated luminosity of 139 fb^{-1}.

Table of Contents

List of Figures

List of Tables

Acknowledgments

I would like to start by thanking my wife, Randi, for the incredible amount of support she has shown me over the years. She has been through this entire journey with me and I am eternally grateful. Next, I would like to thank all of the friends that have stuck with me and supported me as I progressively got worse at responding to text messages and cancelling plans. Lastly, I want to thank my family for providing me the opportunity to pursue this goal and for believing in me the entire time.

I would also like to thank all of the professors at K-State that have guided me through my undergraduate and graduate career. I've recieved too much assistance from too many people to name everyone, but I'd like to specifically thank my advisor, Andrew Ivanov, along with professors Yurii Maravin and Keti Kaadze. I am so thankful to Andrew for giving me the opportunity to start working with the CMS group as a junior in undergrad. And, I appreciate Yurii and Keti for all their support leading the anlaysis that turned into this dissertation. Finally, I want to thank Kim Coy for everything she does. Every graduate student in the K-State physics department will know exactly what I mean. I've been extremely lucky to work with truly great people during my time at K-State.

Chapter 1

Introduction

On July 4, 2012, the Higgs boson was discovered by the ATLAS and CMS collaborations[16–18] confirming the mechanism by which particles gain mass and completing the Standard Model (SM) of physics. While the Standard Model has consistently withstood experimental scrutiny, there are many questions in physics that are not explained in the Standard Model. For instance, it is very natural to assume that both matter and antimatter were present in equal proportions at the beginning of the universe, but the world we interact with every day is composed entirely of matter. This apparent contradiction, known as the baryon asymmetry problem, is one of the biggest open questions in physics and the Standard Model does not offer a feasible explanation. The baryon asymmetry problem requires a level of CP-violation that is not present in the Standard Model and necessitates an additional explanation beyond the Standard Model (BSM). One path forward is to conduct searches for new particles which arise in extensions of the Standard Model and represent a more complete model. A complimentary path is to perform high precision measurements of the properties of known particles to test whether they are consistent with the Standard Model predictions. These high precision measurements can serve as an indirect search for physics beyond the Standard Model. In this case, the BSM model predicts small deviations from SM expectations which can be observed.

The Large Hadron Collider (LHC) provides an opportunity to conduct high precision measurements of Higgs boson's properties with the potential to observe deviations from the Standard Model. Although current measurements of the Higgs boson's properties are consistent with the Standard Model[16–34], the precision is not sufficiently high to exclude the possibility of anomalous couplings which are not predicted by the Standard Model. There are very tight constraints on the spin of the Higgs[28;34], spin-zero, but small anomalous couplings of the Higgs to two gauge bosons are still allowed within current experimental uncertainties. Observation of anomalous couplings will provide evidence for physics beyond the Standard Model.

In this analysis, the properties of the Higgs coupling to gauge bosons are studied using multiple production mechanisms: gluon-gluon fusion (ggH), vector boson fusion (VBF), and associated production (VH). A single Higgs decay mode, $H \rightarrow \tau\bar{\tau}$, is utilized to take advantage of useful properties unique to this decay mode. Because the tau lepton decays within the detector, multiple decay channels are available for study. This analysis focuses on events where one tau lepton decays leptonically while the other decays hadronically. These channels are referred to as $\tau_e\tau_h$ and $\tau_\mu\tau_h$ based on whether the leptonically decaying tau decays into $e\bar{\nu_e}\nu_\tau$ or $\mu\bar{\nu_\mu}\nu_\tau$.

This thesis begins with a discussion of the theory underpinning the analysis. Chapter 2 provides an introduction to the Standard Model and anomalous Higgs boson coupling is given in Chapter 3. The experimental details are then discussed in Chapter 4, Chapter 5, and Chapter 6 which address the Large Hadron Collider (LHC), the Compact Muon Solenoid (CMS) experiment, and the object reconstruction within the CMS experiment, respectively. This is followed by a description of the analysis specific details. The description starts in Chapter 7 which introduces the final states used in this analysis along with the dominant backgrounds and the event selection. This naturally leads to an explanation of the event categorization provided in Chapter 8. Next, Chapter 9 describes the methods used to estimate background contributions to the analysis. The datasets used in this analysis are described in Chapter 10 followed by an overview of the required corrections to those datasets in Chapter 11. An extensive discussion of the sensitive observables for the analysis is provided in Chapter 12 and the uncertainties are assessed in Chapter 13. This thesis concludes with the results of the analysis in Chapter 14 followed by a summary in Chapter 15.

Chapter 2

Standard Model

The Standard Model provides a framework for describing the interactions between all elementary particles. The Standard Model is split into two groups: the particles that make up ordinary matter and the force carriers that facilitate interaction between particles of the first group. The former group is comprised of fermions, particles with half-integer spin that obey Fermi-Dirac statistics, while the latter contains particles with integer spin known as bosons due to their obeying Bose-Einstein statistics. All elementary interactions are described in the Standard Model in terms of fermions interacting via the exchange of bosons.

2.1 Standard Model: A Qualitative Overview

This section provides a qualitative look into the structure of the Standard Model. The principal actors in the model are discussed while a slightly more rigorous mathematical description of the model is left for the next section.

2.1.1 Bosons

The fundamental forces are all characterized by the exchange of force-carrying bosons. The Standard Model incorporates the electromagnetic force, carried by photons, the strong nuclear force, carried by gluons, and the weak nuclear force carried by the $W^{\pm}$ and Z bosons.

Boson	Force	Mass	Width
Photon (γ)	Electromagnetic	-	-
Gluon (g)	Strong	-	-
$W^{\pm}$	Weak	80.4 GeV	2.09 GeV
Z^0	Weak	91.2 GeV	2.50 GeV
H^0	-	125.1 GeV	$<$ 0.013 GeV

Table 2.1: *The properties of all observed bosons. The photon and gluon are massless and therefore have no decay width. All listed bosons are neutrally charged except the* $W^{\pm}$ [14].

While gravity is not yet included in the Standard Model, it is hypothesized that a spin-2 boson called the graviton is responsible for the gravitational force. Additionally, the Higgs field, mediated by the Higgs boson, provides mass to the particles of the Standard Model. The $W^{\pm}$, Z, and Higgs bosons obtain a mass as a result of electroweak symmetry breaking (EWB) while the photon and gluons remain massless. The properties of the Standard Model bosons are listed in Table 2.1.

2.1.2 Fermions

There are twelve distinct fermions generally split into two groups of six based on their behavior under different interactions. Both groups are then sub-divided into three generations which have different masses, but are otherwise identical. Each fermion has an anti-particle with the all the same properties except for the opposite charge. Together these twenty-four fermions compose all known matter. Table 2.2 depicts the fermion groupings and gives their properties.

The first group of fermions, known as leptons, contains the negatively charged electron and its heavier cousins the muon and the tau lepton. Each of these leptons comes with an extremely light, neutrally charged neutrino. All leptons interact via the weak nuclear force and the charged leptons also participate in electromagnetic interactions.

The second group of fermions are the quarks: up, down, charm, strange, top, and bottom. The first generation consists of the fractionally charged up quark (+2/3) and down quark (-1/3) which make up the protons and neutrons of ordinary matter. The second and third generations have similar pairings with the charm and top quarks having (+2/3) charge

	Leptons			Quarks		
Generation	Particle	Mass (MeV)	Charge	Particle	Mass (MeV)	Charge
First	Electron	.511	-1	Up	2.16	1/3
	Electron Neutrino	$< 1.1 \times 10^{-6}$	0	Down	4.67	-2/3
Second	Muon	105.7	-1	Charm	1.27×10^3	1/3
	Muon Neutrino	< 0.19	0	Strange	93.0	-2/3
Third	Tau	1776.9	-1	Top	172.8×10^3	1/3
	Tau Neutrino	< 18.2	0	Bottom	4.18×10^3	-2/3

Table 2.2: *All observed fermions grouped by generation and split into leptons and quarks. The measured masses (in MeV) and charges are shown for each fermion*[14].

and the strange and bottom quarks having (-1/3) charge. In addition to being electrically charged, the quarks also carry the color charge of the strong interaction. The quarks are never observed in isolation, but instead are only seen in colorless bound states of two or three quarks referred to as mesons and baryons, respectively. The quarks also interact via the electromagnetic and weak nuclear forces.

All fermions interact with the Higgs field via a Yukawa coupling in order to gain mass.

2.2 Standard Model: A Mathematical Overview

The Standard Model is a quantum field theory with a Lagrangian density of the form

$$\mathcal{L} = \mathcal{L}(\phi_r, \partial_\mu \phi_r) \tag{2.1}$$

where ϕ_r is a set of fields and ∂_μ is the gradient generalized to four dimensions. The equations of motion for the fields are derived by applying the variational principle to the action integral defined in Eq. 2.2 where Ω is an arbitrary region of phase space.

$$S(\Omega) = \int_\Omega \mathcal{L}(\phi_r, \partial_\mu \phi_r) d^4x \tag{2.2}$$

By allowing the fields to vary as

$$\phi_r(x) \to \phi_r(x) + \delta\phi_r(x), \tag{2.3}$$

and requiring the action to be stationary, we arrive at the Euler-Lagrange equations of motion for the fields Eq. 2.4.

$$\frac{\partial \mathcal{L}}{\partial \phi_r} - \frac{\partial}{\partial x^\alpha}\left(\frac{\partial \mathcal{L}}{\partial \frac{\partial \phi_r}{\partial x^\alpha}}\right) = 0\ , \quad r = 1, \ldots, N. \tag{2.4}$$

The theory is then quantized by applying appropriate canonical commutation relations between the conjugate coordinates and momenta. All particles in the Standard Model correspond to an excitation in these fields.

From Noether's theorem, we know that if the action is invariant under a transformation there will be a corresponding conserved current. The same logic can be used in reverse to show that starting from conserved currents, we can find transformations under which the Lagrangian is invariant. As an example, consider the well-known conservation of electromagnetic charge. It is easy to show that by applying the global phase transformation Eq. 2.5 where α is a constant to the Dirac Lagrangian Eq. 2.6, we can derive a conserved charge. It is also obvious the Lagrangian will be invariant under this transformation.

$$\begin{cases} \psi(x) \to \psi'(x) = \psi e^{-i\alpha} \\ \bar{\psi}(x) \to \bar{\psi}'(x) = \bar{\psi} e^{i\alpha} \end{cases} \tag{2.5}$$

$$\mathcal{L} = \bar{\psi}(x)(i\gamma^\mu \partial_\mu - m)\psi(x) \tag{2.6}$$

The global phase transformation can then be generalized to a local phase transformation Eq. 2.7 along with a gauge transformation of the potential Eq. 2.8. The coupled transformations correspond to a transformation under the $U(1)$ symmetry group. This demonstrates how we can start from the observation of a conserved current, in this case the electromagnetic current, and discover a symmetry of the Lagrangian under $U(1)$ transformations. Using the same process, it can be shown that the Standard Model symmetry group is $SU(3) \otimes SU(2) \otimes U(1)$. The generators of these groups can be mapped to the force-carrying gauge bosons.

$$\begin{cases} \psi(x) \to \psi'(x) = \psi e^{-i\beta f(x)} \\ \bar{\psi}(x) \to \bar{\psi}'(x) = \bar{\psi} e^{i\beta f(x)} \end{cases} \tag{2.7}$$

$$A_\mu(x) \to A'_\mu(x) = A_\mu(x) + \partial_\mu f(x) \tag{2.8}$$

2.2.1 The Electroweak Interaction

The electroweak interaction represents the unification of the electromagnetic force and the weak nuclear force into a single interaction under the $SU(2)\otimes U(1)$ symmetry group. Starting from the free-lepton Lagrangian density with lepton masses set to zero, Eq. 2.9, we impose an odd feature of the weak interaction.

$$\mathcal{L}_0 = i\left[\bar{\psi}_\ell(x)\partial\!\!\!/\psi_\ell(x) + \bar{\psi}_{\nu_\ell}(x)\partial\!\!\!/\psi_{\nu_\ell}(x)\right] \tag{2.9}$$

From observation, we know that the weak interaction only involves left-handed particles and right-handed antiparticles so we can split the lepton fields

$$\frac{1}{2}(1 \pm \gamma_5)\psi(x) \equiv \begin{cases} \psi^L(x) = P_L\psi(x) \\ \psi^R(x) = P_R\psi(x) \end{cases} \tag{2.10}$$

then rewrite the fields as two-component fields

$$\Psi^L(x) = \begin{pmatrix} \psi^L_\ell(x) \\ \psi^L_{\nu_\ell}(x) \end{pmatrix};\ \bar{\Psi}^L(x) = \left(\bar{\psi}^L_\ell(x), \bar{\psi}^L_{\nu_\ell}(x)\right) \tag{2.11}$$

After rewriting Eq. 2.9 in terms of the two-component fields, we can apply the $SU(2)$ and $U(1)$ transformations enforcing local phase invariance. The transformations take the form

$$\begin{cases} \Psi^L_\ell(x) \to \Psi'^L_\ell(x) = \exp[ig\tau_j\omega_j(x)/2]\Psi^L_\ell(x) \\ \bar{\Psi}^L_\ell(x) \to \bar{\Psi}'^L_\ell(x) = \exp[ig\tau_j\omega_j(x)/2]\bar{\Psi}^L_\ell(x) \end{cases}$$

where g is the coupling constant, τ_j are the 3 Pauli matrices, and ω_j are 3 real, differentiable functions. Following the same procedure as before, we end up with four new fields: three from the $SU(2)$ transformations and one from $U(1)$. The photon, $W^{\pm}$ bosons, and Z boson are then identified as linear combinations of the four gauge fields.

We can now attempt to add mass terms to the Lagrangian density, but these terms break the $SU(2) \otimes U(1)$ symmetry and also lead to renormalization issues. The Glashow model proceeds with adding the mass terms and accepts the broken symmetry. While the Glashow model does provide decent agreement with experiment in first-order perturbation theory, it is not renormalizable. To maintain the gauge symmetry and renormalizability, all lepton and gauge boson masses must be set to zero.

2.2.2 Electroweak Symmetry Breaking

Electroweak symmetry breaking provides a mechanism to introduce non-zero masses to the Standard Model particles while maintaining renormalizability and gauge invariance. It is important to note that the symmetry breaking does not refer to a term in the Lagrangian that violates a previously imposed symmetry, but that it refers to the situation where the ground state of a system is degenerate. In this case, the arbitrary choice of one of the degenerate states results in a ground state that no longer shares the symmetries of the Lagrangian. The symmetry has been spontaneously broken by the choice of a ground state. For a field theory, the ground state corresponds to the vacuum expectation value (vev)

$$\langle 0|\phi(x)|0\rangle = \phi_0 \tag{2.12}$$

The Higgs mechanism builds on EWB to provide a way to introduce a complex scalar field to the Lagrangian along with the massless vector fields and produce a real scalar field and massive vector fields without breaking the gauge invariance of the Lagrangian density. A complex scalar field, ϕ, is introduced to the Lagrangian along with the Higgs potential $V(\phi)$ leading to a Higgs term in the Lagrangian

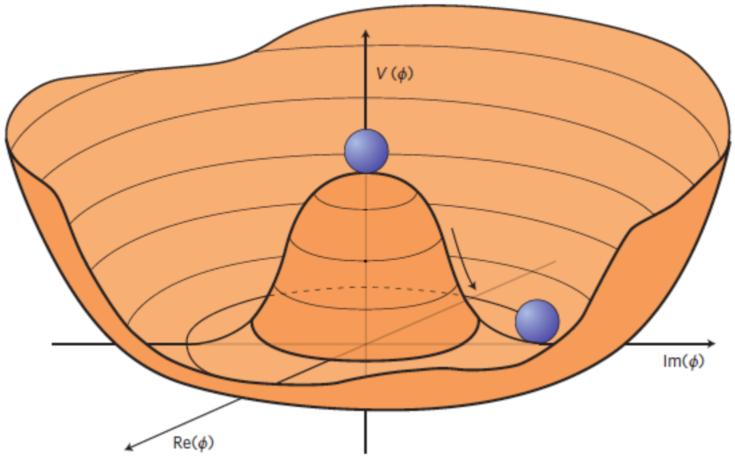

Figure 2.1: *The Higgs potential from Eq. 2.13 with $\mu^2 < 0$. The potential is symmetric about zero in the real-imaginary plane requiring spontaneous symmetry breaking to choose the ground state*[1].

$$\mathcal{L} = [D^\mu \phi(x)]^* [D^\mu \phi(x)] - \mu^2 |\phi(x)|^2 - \lambda |\phi(x)|^4 \tag{2.13}$$

where D^μ is the covariant derivative used to enforce gauge symmetry in the electroweak interaction and $\phi(x)$ is given by Eq. 2.14 with $\sigma(x)$ and $\eta_i(x)$ as real scalar fields.

$$\phi(x) = \frac{1}{\sqrt{2}} \begin{pmatrix} \eta_1(x) + i\eta_2(x) \\ v + \sigma(x) + i\eta_3(x) \end{pmatrix} \tag{2.14}$$

In order to put a lower bound on the potential, it must be that $\lambda > 0$ while μ^2 has no such constraint. In order to have EWB, the vev must be degenerate leading to the requirement that $\mu^2 < 0$. This potential is shown in Fig. 2.1. The arbitrary choice of ground state is made such that

$$\phi_0 = \begin{pmatrix} 0 \\ \frac{1}{\sqrt{2}} v \end{pmatrix} ;\ v = \left(\frac{-\mu^2}{2\lambda} \right) \tag{2.15}$$

Now that the ground state is chosen, we can write Eq. 2.14 in the unitary gauge as

$$\phi(x) = \frac{1}{\sqrt{2}} \begin{pmatrix} 0 \\ v + \sigma(x) \end{pmatrix} \tag{2.16}$$

by simply applying a $SU(2)$ transformation followed by a $U(1)$ transformation to Eq. 2.14.

The Higgs term, now written in the unitary gauge, can be added to the rest of the fields we have been building in the unitary gauge. Then, the full SM Lagrange density can be written in the unitary gauge by applying the same $SU(2) \otimes U(1)$ transformation resulting in four gauge fields just as in Sec. 2.2.1. The four resulting fields can be identified as the massive gauge bosons, $\mathrm{W}^{\pm}$ and Z^0, and the massless photon, A as shown in Eq. 2.17.

$$\begin{aligned} W_\mu^{\pm} &= \frac{1}{\sqrt{2}}\left(W_\mu^1 \mp iW_\mu^2\right) &&; \qquad m_W = \frac{1}{2}vg \\ Z_\mu^0 &= \frac{1}{\sqrt{g^2+g'^2}}\left(gW_\mu^3 - g'B_\mu\right) &&; \qquad m_Z = \frac{m_W}{cos\theta_W} \\ A_\mu^0 &= \frac{1}{\sqrt{g^2+g'^2}}\left(g'W_\mu^3 + gB_\mu\right) &&; \qquad m_A = 0 \end{aligned} \tag{2.17}$$

where W_μ^i are the three fields generated by $SU(2)$, B_μ is the field generated by $U(1)$, g is the coupling constant from the $SU(2)$ transformation, and g' is the coupling constant from the $U(1)$ transformation, and θ_W is the weak mixing angle.

Also, the Higgs boson appears as the quanta of the additional Higgs field added to the Lagrangian. The Higgs boson has mass given by Eq. 2.18.

$$m_H = \sqrt{-2\mu^2} \tag{2.18}$$

Because the Higgs boson is the quantum of a real scalar field, it is predicted to be a neutral, spin-zero particle which behaves like a scalar. This means the Standard Model Higgs boson will be an eigenstate of the CP transformation, Eq. 2.19, where C denotes charge conjugation and P denotes a parity transformation.

$$CP\left|\Psi\right\rangle = \lambda\left|\Psi\right\rangle \tag{2.19}$$

In particular, the Higgs boson will be a CP-even state, $\lambda = +1$, rather than a CP-odd state, $\lambda = -1$.

The Higgs mechanism also enables the fermions to gain mass terms in the Lagrangian via a Yukawa coupling with the Higgs field Eq. 2.20

$$\mathcal{L} = m_f \bar{\psi}_f \psi_f \tag{2.20}$$

where the fermion mass m_f is a function of the vev and the measured coupling strength.

2.2.3 The Strong Interaction

The theory describing the strong interaction is known as quantum chromodynamics (QCD) and is the result of imposing invariance of the SM Lagrangian under transformations from the $SU(3)$ symmetry group. Particles that participate in the strong interaction, quarks and gluons, carry color charge which is analogous in some ways to electric charge in the electroweak interaction. Unlike electric charge which comes in two forms, there are three different color charges: red, green, and blue. Each quark carries one color charge, while gluons carry a color-anticolor pair in order to change the color charge of the quarks involved in the interaction. For instance, a red-antigreen gluon may interact with a green quark to change the quark's charge to red. It is easy to see that a total of eight uniquely-charged gluons are required to mediate interactions between all possible color combinations of two quarks while conserving color charge.

The Lagrangian density for QCD is given by Eq. 2.21

$$\mathcal{L} = \bar{\psi}_a(x) \left[i \not{D}_{ab} - m \delta_{ab} \right] \psi_b(x) \tag{2.21}$$

with the covariant derivative given by Eq. 2.22 and the gluon field strength tensor Eq. 2.23.

$$D^{\mu}_{ab} = \delta_{ab} \partial^{\mu} + \frac{i}{2} g_s (\lambda_j)_{ab} A^{\mu}_j(x) - \frac{1}{4} G_{i\mu\nu}(x) G_i \mu\nu(x) \tag{2.22}$$

$$G^{\mu\nu}_i(x) = F^{\mu\nu}_i(x) + g_s f_{ijk} A^{\mu}_j(x) A^{\nu}_k(x) \tag{2.23}$$

In these equations, $F^{\mu\nu}_i$ are the gluon fields with $i = 1, \ldots, 8$, λ_j are the Gell-Mann matrices, g_s is the strong coupling strength, and f_{ijk} are the structure constants of the

$SU(3)$ symmetry group. The coupling strength g_s can be used to define the strong coupling constant $\alpha_s = g_s/4\pi$. The strong coupling constant is unique in the SM because it is a running coupling constant that depends on the momentum transfer in the process. This is reflected in the definition

$$\alpha_s(\mu^2) = \frac{\alpha_s(\mu_R^2)}{1 + \beta_0 \alpha_s(\mu_R^2) \ln(\mu^2/\mu_R^2)} \tag{2.24}$$

where μ^2 is the square of the momentum transfer, μ_R^2 is the renormalization scale where the coupling constant is known empirically, and β_0 relates the number of colors n_c and the number of quark flavors n_q as follows

$$\beta_0 = \frac{11n_c - 2n_q}{12\pi} \tag{2.25}$$

In the Standard Model, there are 3 known colors and 6 flavors of quarks leading to $\beta_0 > 0$. Taking the asymptotic limits of the strong coupling constant in the Standard Model leads to some strange features of QCD.

First, in the high momentum transfer limit ($\mu \to \infty$) the strong coupling constant approaches zero allowing perturbation theory to provide an accurate description of interactions. This is the only region in which we can accurately model QCD interactions. In contrast, at the low momentum transfer limit ($\mu \to 0$) the strong coupling strength explodes. This is easy to see because the coupling strength scales as the inverse of the natural log of the momentum transfer, which blows up as the momentum transfer approaches zero. The low energy limit can also be interpreted as the high separation limit meaning that the further apart two quarks are separated, the stronger the coupling strength. This result is reflected by the fact that quarks are never observed in isolation, but are only seen in colorless pairs or triplets (mesons and hadrons). As a pair of quarks are separated, energy builds in the system analogous to the stretching of a spring. At some point, enough potential is stored in the system that a quark-antiquark pair is created to form two colorless pairs. This phenomenon is known as quark confinement and results in another phenomenon, hadronization, at high energies where a single high energy quark can result in numerous pair productions leaving many outgoing hadrons.

2.3 Higgs Boson Production and Decay

Fig. 2.3 shows the four main processes by which the Higgs production can occur at the LHC and Table 2.3 shows the cross section of each production mode for $m_H = 125.09$ GeV. It is clear from the table that the process with the highest cross section is gluon-gluon fusion (ggH) in which a pair of high energy gluons merge to form a Higgs boson. Because the gluons do not couple directly to the Higgs, the production is enabled via a loop which is dominated in the Standard Model by top quarks. It is possible for additional jets to be radiated away during this production, but each additional jet is suppressed by a factor proportional to the strong coupling constant. An order of magnitude smaller in cross section, vector-boson fusion (VBF) provides the second highest cross section and is characterized by the two quarks produced in association with the Higgs. These quarks give a distinct signal as they generally appear in the far forward regions of the detector. Associated production with a W boson and associated production with a Z boson are referred to jointly as VH while production with top quarks is referred to as ttH. These processes have very small cross sections and are fairly rare at the LHC. ttH production is particularly interesting because it provides an avenue to study how fermions couple to the Higgs at tree-level. The ttH production channel is studied in a dedicated analysis not included in this thesis.

Production		Decay	
Process	XS (Pb^{-1})	Process	BR (%)
ggH	48.61	bb	58.09
VBF	3.766	$\tau\tau$	6.272
WH	1.358	$\mu\mu$	0.002
ZH	0.880	WW	21.52
ttH	0.6128	ZZ	2.641

Table 2.3: *Higgs production cross sections for various processes at* $\sqrt{s} = 13$ TeV *(left) and Higgs decay branching fraction (right). Both are shown for* $m_H = 125.09$ GeV[15].

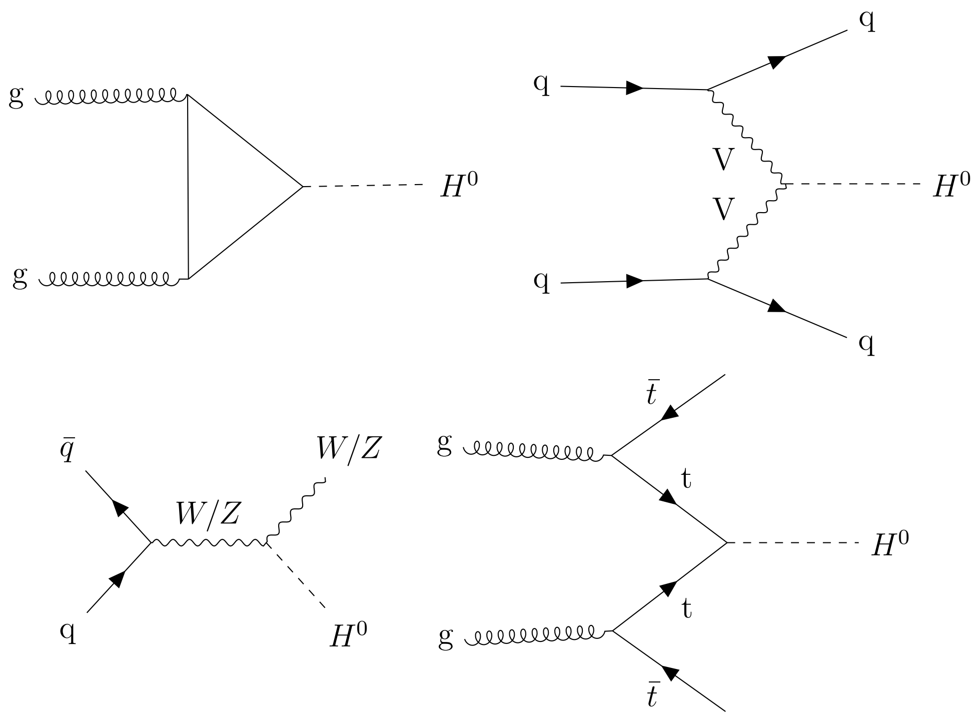

Figure 2.2: *The four main Higgs production mechanisms ordered by cross section. Gluon-gluon fusion (ggH) shown top-left has the highest cross section and corresponds to the majority of Higgs production. Vector boson fusion (VBF) shown top-right provides the second highest contribution with a cross section an order of magnitude smaller than ggH. Smaller still, associated production (VH) shown bottom-left and ttH production shown bottom-right provide the smallest contributions.*

The Higgs branching fractions are also shown in Table 2.3 for various decay channels. The branching fraction to fermions scales with the mass of the fermion whereas $H \to t\bar{t}$ is kinematically forbidden. The $H \to b\bar{b}$ decay has the highest branching fraction, but is in practice a very difficult analysis at the LHC due to the nature of hadron collisions. The $H \to b\bar{b}$ final state is accompanied by an overwhelming background of multijet events which occur frequently in hadron colliders. In contrast, the $H \to \mu\bar{\mu}$ decay is an exceptionally clean channel where exactly two muons can be clearly identified and the dimuon mass resonance will be very sharp. The difficulty with this channel is that the branching fraction is so small that the current integrated luminosity delivered by the LHC is not sufficient to construct an analysis sensitive to $H \to \mu\bar{\mu}$. $H \to \tau\bar{\tau}$ provides a great compromise with a cross section much larger than $H \to \mu\bar{\mu}$ and much smaller backgrounds than $H \to b\bar{b}$. The $H \to \tau\bar{\tau}$ decay has already been observed[35] by CMS and ATLAS with a significance $> 5\sigma$ implying that sufficient statistics has been collected to perform a sensitive analysis. The $H \to \tau\bar{\tau}$ decay requires two tau leptons to be present greatly suppressing the multijet background that plagues the $H \to b\bar{b}$ channel. The main difficulty in $H \to \tau\bar{\tau}$ comes from the fact that the tau lepton decays within the volume of the detector and can only be observed via its decay products.

Chapter 3

Phenomenology

In the Standard Model, the Higgs boson is a CP-even scalar: quantum numbers $J^{PC} = 0^{++}$. These quantum numbers can be measured experimentally by studying the Higgs coupling in both production and decay. The nature of the coupling produces noticeable effects in the kinematics of incoming and outgoing particles for production and decay, respectively. For example, in VBF production (Fig. 2.3) we can easily measure the azimuthal angle between the two associated quarks. The details of the HVV coupling determine the kinematic distribution of this angle over a set of events. This is shown in Fig. 3.1 where the red distribution shows the angle between the quarks in VBF (left) and ggH (right) production for the SM CP-even Higgs scalar. The other distributions show the angle under the hypothesis of a pseudoscalar Higgs (black) and in the presence of interference between a mixed scalar and pseudoscalar Higgs (green and blue). Clearly, different coupling scenarios produce drastically different distributions. It is also worth noticing that while pure CP-even and pure CP-odd states produce distribution symmetric about zero, the mixed states are strikingly asymmetric. This is a feature that is utilized later in the analysis.

Since the discovery of the Higgs boson, the Higgs coupling has been probed extensively to determine its quantum numbers. All current experimental evidence is consistent with the SM Higgs[16–34], but the measurement uncertainty is still too large to completely exclude small anomalous couplings. It is possible that there are CP-odd Higgs couplings the effects

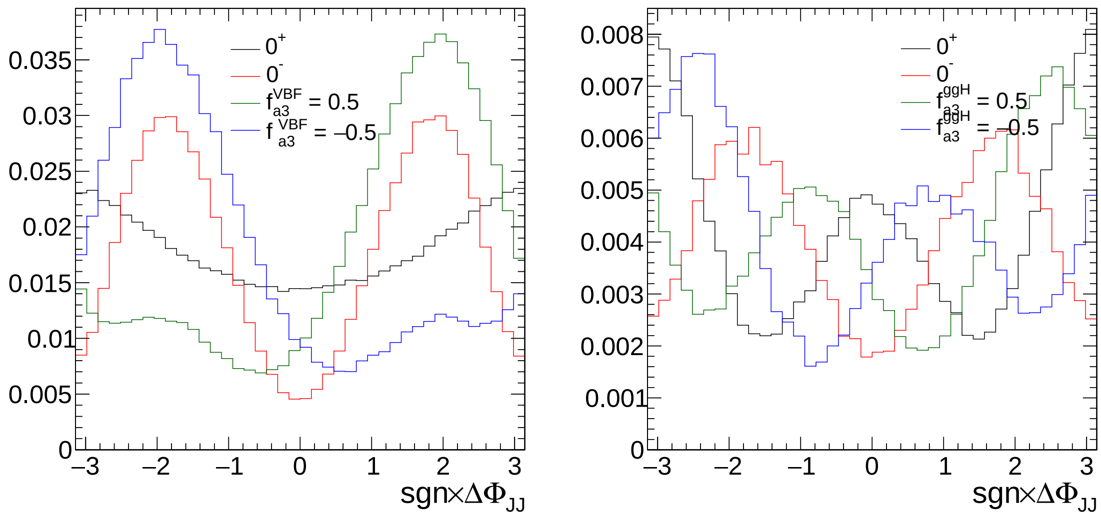

Figure 3.1: *The azimuthal angle between the two jets produced in association with the Higgs boson for VBF (left) and ggH (right) production. The correlation between jets produced in association with a scalar Higgs (red) and pseudoscalar Higgs (black) is shown in both plots. Different mixtures of CP-even and CP-odd states are also shown in blue and green.* [2;3]

of which, including interference with the CP-even state, are beyond the current experimental precision. The presence of anomalous couplings directly to gauge bosons would be proof of CP-odd Higgs couplings which are not expected in the Standard Model. These couplings are probed using the VBF and VH production mechanisms. Because ggH is a loop-induced process, anomalous couplings in ggH production can be caused by CP-odd couplings or by the presence of non-Standard Model particles. The contribution of all particles within a loop must be summed which means that a deviation from SM prediction could be the result of an undiscovered particle contributing to the loop. Because the anomalous couplings require new physics, measuring the Higgs couplings provides a strong test of the Standard Model and a probe for physics beyond the Standard Model.

We start by constructing the most general scattering amplitude possible for the interaction of a spin-zero particle (X) with two gauge bosons (V_1, V_2) [2]. First, we denote the momentum of X with q while q_1, q_2 are the momenta of the two gauge bosons. We assume the gauge bosons are transversely polarized: $q_i \epsilon_i = 0$ where ϵ_i is the gauge boson polarization vector. The gauge boson field strength tensor is then written as

$$f^{(i)\mu\nu} = \epsilon_i^\mu q_i^\nu - \epsilon_i^\nu q_i^\mu \tag{3.1}$$

with conjugate field strength tensor

$$\tilde{f}^{(i)}_{\mu\nu} = \frac{1}{2}\epsilon_{\mu\nu\rho\sigma} f^{(i)\rho\sigma} = \epsilon_{\mu\nu\rho\sigma}\epsilon_i^\rho q_i^\sigma \tag{3.2}$$

Then, the general scattering amplitude can be written as Eq. 3.3

$$A(X \to VV) = v^{-1}\left(g_1 m_V^2 \epsilon_1^* \epsilon_2^* + g_2 f^{*(1)\mu\nu} f^{*(2),\mu\nu} + g_3 f^{*(1),\mu\nu} f^{*(2)}_{\mu\alpha}\frac{q_\nu q^\alpha}{\Lambda^2} + g_4 f^{*(1)}_{\mu\nu}\tilde{f}^{*(2),\mu\nu}\right) \tag{3.3}$$

where v is the vacuum expectation value and Λ is the cutoff scale for BSM physics. The constants g_i can be thought of as effective coupling constants under the assumption that X, V_1, V_2 are all produced on-shell. This expression is kept general to account for coupling to massive and massless gauge bosons. For massless gauge bosons, the expression is simplified by imposing $m_V = 0$. Alternatively, the tree-level HZZ coupling can be recovered by assigning $X = H$ then setting $g_1 = 2i$ and $g_{i>1} = 0$.

Eq. 3.3 can be rewritten by factoring out the polarization vectors as follows

$$A(X \to VV) = v^{-1}\epsilon_1^{*\mu}\epsilon_2^{*\nu}\left(a_1 g_{\mu\nu} m_X^2 + a_2 q_\mu q_\nu + a_3 \epsilon_{\mu\nu\rho\sigma} q_1^\rho q_2^\sigma\right) \tag{3.4}$$

Here, the coefficients a_i are defined as follows

$$a_1 = g_1\frac{m_V^2}{m_X^2} + g_2\frac{2s}{m_X^2} + g_3 k\frac{s}{m_X^2}, \qquad a_2 = -2g_2 - g_3 k, \qquad a_3 = -2g_4 \tag{3.5}$$

with

$$s = q_1 q_2 = \frac{m_X^2 - 2m_V^2}{2}; \qquad k = \frac{s}{\Lambda^2} \tag{3.6}$$

At this point we focus on the HVV scattering amplitude which allows us to rewrite Eq. 3.4

in a more interprettable form

$$A(HVV) \sim \left[a_1^{VV} + \frac{\kappa_1^{VV} q_1^2 + \kappa_2^{VV} q_2^2}{(\Lambda_1^{VV})^2}\right] m_{V1}^2 \epsilon_{V1}^* \epsilon_{V2}^* + a_2^{VV} f_{\mu\nu}^{*(1)} f^{*(2)\mu\nu} + a_3^{VV} f_{\mu\nu}^{*(1)} \tilde{f}^{*(2)\mu\nu} \quad (3.7)$$

where κ_i are simply a phase factors for each gauge boson[28].

3.1 The HVV Vertex

The easiest way to start understanding this amplitude is to break it into terms and discuss each term individually. The first term, the one containing $m_{V1}^2 \epsilon_{V1}^* \epsilon_{V2}^*$, is responsible for CP-even, tree-level couplings. This is the only term that is nonzero in the case that no BSM physics is present in the Higgs coupling. The brackets in this term contain the Standard Model coupling, a_1, along with a coupling that scales as Λ^{-2}. The Λ term accounts for BSM physics that affect the CP-even tree-level couplings and is exactly zero in the Standard Model. In practice, we differentiate between two Λ terms while summing over all gauge bosons. The two Λ terms are: $\Lambda_{ZZ} = \Lambda_{WW} = \Lambda_1$ and $\Lambda_1^{Z\gamma}$. Because the kinematics for ZZ fusion and WW fusion are extremely similar, we choose to make the simplification $a_1^{ZZ} = a_1^{WW}$ and $\kappa_i^{WW}/(\Lambda_1^{WW}) = \kappa_i^{ZZ}/(\Lambda_1^{ZZ})$. This is just a choice to simplify the analysis and may be reinterpreted for any other ratio a_1^{WW}/a_1^{ZZ}.

The next term, proportional to a_2, provides CP-even loop-level couplings. In the SM, HVV coupling is only observed at the tree-level meaning that an observation $a_2 \neq 0$ hints at BSM physics, although it could also simply be caused by loop diagrams that are beyond the current precision. Under the assumption that a nonzero measurement of a_2 is caused by new physics, the most likely explanation is a heavy state that hasn't yet been observed. Aside from containing potential new physics, this term is also pure CP-even i.e. it is not sensitive to any CP-violation.

The last term includes the pure CP-odd coupling scaled by the coupling constant a_3. If CP-violation is present in the Higgs coupling, it will appear as a nonzero value for the parameter a_3. Of course the a_3 parameter can not provide information about the cause of the

CP-violation, but it would be a clear indication of a CP-odd Higgs coupling which requires BSM physics.

The interpretation of these coupling constants carries over directly to associated production where, again, two gauge bosons couple directly to the Higgs boson. As a result, four parameters are measured in the VBF and VH analysis. These include the parameter sensitive to CP-violation: a_3, the loop-level, CP-even BSM parameter: a_2, and the tree-level CP-even BSM parameters: $\Lambda_{WW} = \Lambda_{ZZ} = \Lambda_1$ and $\Lambda_1^{Z\gamma}$.

In order to cancel many systematic uncertainties involved in measuring the couplings directly, we choose to measure the ratio of effective cross sections. Each coupling constant is measured relative the the SM contribution a_1. The four ratios and related phases are shown in Eq. 3.8.

$$\begin{aligned}
f_{a3} &= \frac{|a_3|^2\sigma_3}{|a_1|^2\sigma_1 + |a_2|^2\sigma_2 + |a_3|^2\sigma_3 + \tilde{\sigma}_{\Lambda 1}/(\Lambda_1)^4 + \dots}; & \phi_{a3} &= arg(\frac{a_3}{a_1}) \\
f_{a2} &= \frac{|a_2|^2\sigma_2}{|a_1|^2\sigma_1 + |a_2|^2\sigma_2 + |a_3|^2\sigma_3 + \tilde{\sigma}_{\Lambda 1}/(\Lambda_1)^4 + \dots}; & \phi_{a2} &= arg(\frac{a_2}{a_1}) \\
f_{\Lambda 1} &= \frac{\tilde{\sigma}_{\Lambda 1}/(\Lambda_1)^4}{|a_1|^2\sigma_1 + |a_2|^2\sigma_2 + |a_3|^2\sigma_3 + \tilde{\sigma}_{\Lambda 1}/(\Lambda_1)^4 + \dots}; & & \phi_{\Lambda 1} \\
f_{\Lambda_1}^{Z\gamma} &= \frac{\tilde{\sigma}_{\Lambda 1}^{Z\gamma}/(\Lambda_1^{Z\gamma})^4}{|a_1|^2\sigma_1 + \tilde{\sigma}_{\Lambda 1}^{Z\gamma}/(\Lambda_1^{Z\gamma})^4 + \dots}; & & \phi_{\Lambda 1}^{Z\gamma}
\end{aligned} \tag{3.8}$$

The cross section, σ_i, corresponds to the case where the corresponding coupling, a_i, is set to one and all other couplings are set to zero. In this analysis, only $\phi_{ai} = 0$ or π are allowed in order to restrict the couplings in Eq. 3.7 to be constant and real. This corresponds to an effective Lagrangian notation.

3.2 The Hgg Vertex

The first term in Eq. 3.7 accounts for tree-level couplings and therefore must vanish for processes like gluon-gluon fusion where the gauge bosons do not couple directly to the Higgs, and must be mediated by a loop. In this case, a_2^{gg} accounts for Standard Model couplings while a_3^{gg} scales CP-odd contributions to the coupling. In the Standard Model, this loop is dominated by $t\bar{t}$ due to its large mass with a much smaller contribution from the next heaviest particle anti-particle pair: $b\bar{b}$. In order to remain agnostic to the existence of undiscovered particles, we do not make any assumptions about the content of the loop and write the scattering amplitude as

$$A(Hgg) = a_2^{ggH} f_{\mu\nu}^{*(1)} f^{*(2)\mu\nu} + a_3^{ggH} f_{\mu\nu}^{*(1)} \tilde{f}^{*(2)\mu\nu} \tag{3.9}$$

The effective cross section is then given in Eq. 3.10.

$$f_{a3}^{ggH} = \frac{|a_3^{\mathrm{ggH}}|^2}{|a_2^{\mathrm{ggH}}|^2 + |a_3^{\mathrm{ggH}}|^2} \tag{3.10}$$

In the end, this analysis places constraints on the five coupling constants in Eq. 3.11. Because the presence CP-violation in HVV will effect the measurement of CP in Hgg and vice versa, the CP-sensitive parameters f_{a3} and f_{a3}^{ggH} are left simultaneously unconstrained.

$$\begin{aligned} Hgg: &\quad \frac{|a_3^{\mathrm{ggH}}|^2}{|a_2^{\mathrm{ggH}}|^2 + |a_3^{\mathrm{ggH}}|^2} sign\left(\frac{a_3^{\mathrm{gg}}}{a_2^{\mathrm{gg}}}\right) \\ HVV: &\quad f_{ai} cos\left(\phi_{ai}\right) \end{aligned} \tag{3.11}$$

3.3 Comparison of HVV and Hgg

The sensitivity to CP-violation in the HVV and Hgg vertices are fundamentally different due to the differences in the Feynman diagrams. The HVV vertex is a tree-level process which always produces two easily identifiable jets. The correlation between these jets is the key to accessing the nature of the Higgs coupling in HVV. The left side of Fig. 3.1 shows that a very strong correlation is present in the quarks from VBF production. In contrast, the right side of Fig. 3.1 shows that the correlation between jets in ggH production is much weaker. This has to do with the fact that ggH production is a loop-induced process and, to first order, does not produce any additional jets. Two additional jets must be radiated during the production in order to access CP-violation via ggH production. The production of each of these jets is suppressed by a factor proportional to the strong coupling constant meaning that the majority of ggH events which do not have additional jets do not provide information needed for measuring CP-violation. The combination of lower acceptance and weaker correlation in ggH production results in much lower sensitivity to the Hgg vertex with respect to the HVV vertex.

Chapter 4

The Large Hadron Collider

The Large Hadron Collider (LHC)[36], built by the European Organization for Nuclear Research (CERN), is the largest, most powerful accelerator constructed to date. It is designed to accelerate two proton (or heavy ion) beams along a circular path to nearly the speed of light before colliding. The LHC is located in a 26.7 km circular tunnel 45 m below the CERN complex on the border between Switzerland and France. The tunnel was previously home to the Large Electron Positron (LEP) collider, which was decommissioned in November 2000 after operating for 11 years. Numerous experiments are located around the LHC to study a myriad of topics using the interactions produced by the accelerator. Of these experiments, four sit directly on the beamline - one at each interaction point. These experiments are ATLAS, CMS, ALICE, and LHCb.

As a circular collider, the maximum center of mass energy ($\sqrt{s}$) of the LHC is determined by the size of the ring and the power of the magnets responsible for keeping particles contained within the ring. The circumference of the ring is constrained by the previously dug tunnel to be 26.7 km. Currently, superconducting niobium-titanium magnets are used to create an 8.33 T field that contains the particles within the ring. The result is a maximum center of mass energy of 13 TeV with the capability to increase to 14 TeV in the future. To increase this energy, advances in magnet technology are required. For example, development of 16 T magnets for a future collider could be installed on the LHC to create the High-Energy

LHC (HE-LHC) with $\sqrt{s} = 27$ TeV.

The LHC is fed by a string of accelerators located within the CERN complex starting from a simple container of hydrogen gas[37]. The gas is passed through an electric field to isolate the protons. The Linear Accelerator 2 (LINAC2)[38] is the only linear accelerator feeding the LHC and provides the initial kick to accelerate the protons to 50 MeV. The protons are then fed to the Proton Synchrotron Booster (Booster)[39] which further accelerates the protons to 1.4 GeV. The Booster was installed because the 50 MeV energy coming from LINAC2 severely limited the number of protons the next stage of acceleration could accept. This next stage is the Proton Synchrotron (PS)[40] which is a 628 m ring with 100 dipole magnets allowing protons to be accelerated up to 25 GeV. The last stage of acceleration before entering the LHC occurs in the 7 km ring of the Super Proton Synchrotron (SPS)[41]. 744 dipole magnets allow the SPS to accelerate protons to 450 GeV before they encounter a kicker magnet which injects the protons into the two opposite-direction beams of the LHC.

4.1 The LHC Ring and Beam Dynamics

The LHC is responsible for accelerating the protons from 450 GeV up to the their final energy of 6.5 TeV. This is done using radio-frequency (RF) cavities which contain an electric field oscillating at 400 MHz created by a potential difference of 2 MV. The oscillation is timed precisely to create bunches of protons spaced by 25 ns by accelerating the slower protons in a bunch while simultaneously retarding the faster protons in the bunch. The accelerated protons are contained within the beam by a strong magnetic field generated using 1232 niobium-titanium dipole magnets cooled using superfluid liquid helium to 1.9 K. Each magnet is 15 meters long and creates an 8.33 T field.

To increase the number of interactions that occur at each interaction point, the beams must be focused in the $x - y$ plane. Quadrupole magnets provide the ability to focus the beam along one axis at the cost of defocusing in the other direction. By using multiple quadrupole magnets in alternating orientations, the beam can be focused in both x and y. The distribution of protons within each bunch can be assumed Gaussian with a standard deviation given by

$$\sigma_i = \sqrt{\epsilon\beta_i} \tag{4.1}$$

where i may be x or y, ϵ is the beam emittance, and β is a function that depends on the properties of the quadrupoles. The instantaneous luminosity can then be defined as

$$\mathcal{L} = \frac{f n_b n_1 n_2}{4\pi\sigma_x\sigma_y}\mathrm{F} \tag{4.2}$$

Here f is the frequency of revolution, n_b is the number of bunches, and n_i are the number of protons in each beam. The factor F accounts for a reduction in luminosity due to crossing angle, beam size, and other technical properties of the interaction. The total number of interactions can then easily be calculated by scaling the total integrated luminosity by the cross section for proton-proton collision, Eq. 4.3.

$$N_p = \sigma_p \int \mathcal{L} dt \tag{4.3}$$

The LHC is designed to deliver an instantaneous velocity of about $10^{-34} cm^{-2} s^{-1}$. This luminosity decreases as collisions occur, the beam disperses, and other issues occur throughout a run. Occasionally, the entire beam must be dumped and restarted for a variety of reasons. As a result, the LHC has been able to deliver a total integrated luminosity of nearly 160 fb^{-1} since 2016. Fig. 4.1 shows the integrated luminosity for each year. Fig. 4.2 shows the total integrated luminosity as a function of time. This analysis uses the data collected by the CMS detector during the years 2016, 2017, and 2018 amounting to 158.7 fb^{-1}.

Prior to 2015 the LHC was run at a lower center of mass energy. It started operation in 2010 at 7 TeV, continued operation in 2011 at 7 TeV with increased luminosity, then was upgraded to 8 TeV in 2012. In July 2012, observation of the Higgs boson was confirmed by both CMS and ATLAS experiments at 8 TeV using only about a quarter of the integrated luminosity collected in 2012 and the data collected at 7 TeV. The LHC then entered its first long shutdown from 2013 to 2015 to conduct many upgrades including those necessary to allow operation at the designed energy of 14 TeV. Now, the LHC is in the second long

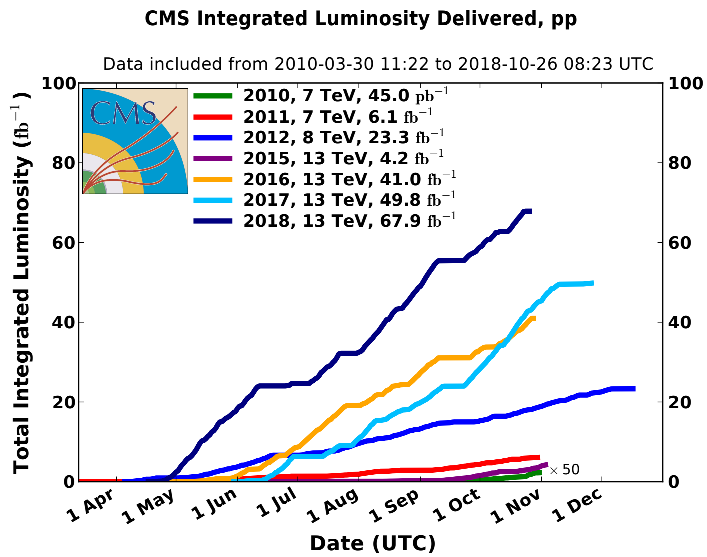

Figure 4.1: *The total integrated luminosity per year delivered to the CMS experiment as a function of time*[4].

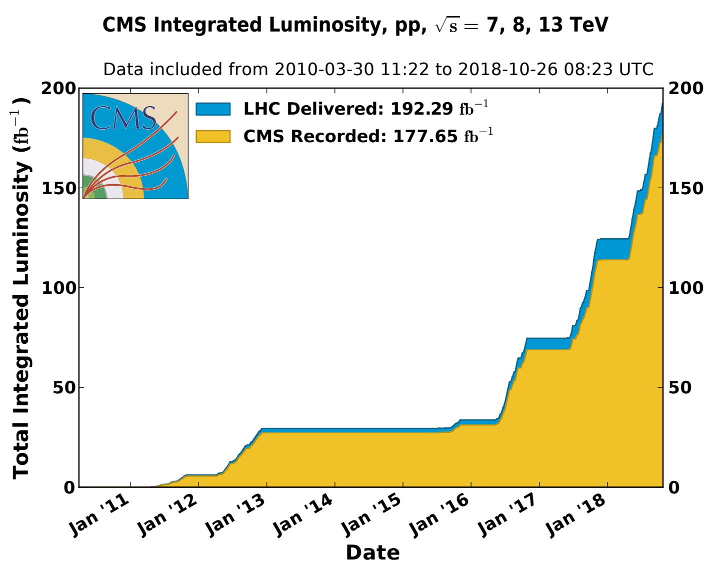

Figure 4.2: *The total integrated luminosity delivered to the CMS experiment as a function of time*[4].

shutdown following four years of data-taking from 2015 to 2018. The current shutdown is expected to last until 2021 and is part of the high luminosity LHC (HL-LHC) upgrade designed to allow operation at much higher instantaneous luminosities.

Chapter 5

The CMS Detector

The CMS detector[7;42–46] is one of the four detectors located at an interaction point along the LHC. It is designed to operate as a general purpose detector combining information from multiple subsystems to provide a comprehensive picture of every interaction that takes place within its volume. In order to produce a truly comprehensive picture of the interaction, the detector must be designed in such a way that it provides as close to a hermetic seal as possible, without blocking the beamline. To accomplish this, the detector is split into the cylindrically-shaped barrel region and two disc shaped endcap regions with each region composed of multiple layers containing the various subsystems.

The cylindrical shape of the detector lends itself to defining a cylindrical coordinate system for interactions. First, the rectangular coordinates (x, y, z) are defined to have x point directly toward the center of the LHC, y point directly upward, and z point along the tangent line starting at the CMS detector in the counterclockwise direction. The spherical coordinates (ρ, ϕ, θ) can then be defined with ρ as the radial distance from the beamline, ϕ as the azimuthal angle, and θ as the angle with respect to the z axis. Both coordinate systems are shown in Fig. 5.1. In practice, the angle θ is rarely used directly, but is instead replaced with the pseudorapidity η defined as

$$\eta = \ln\left[tan\left(\frac{\theta}{2}\right)\right] \tag{5.1}$$

η is referred to as the pseudorapidity because it approaches the rapidity

$$y = \frac{1}{2} \ln \left[\frac{E + p_z}{E - p_z} \right] \tag{5.2}$$

in the high energy limit. The four momentum can then be defined as

$$p_i^\mu = (p_T, \eta, \phi, m_i) \tag{5.3}$$

where p_T is the momentum in the transverse plane and m_i is the mass of the particle.

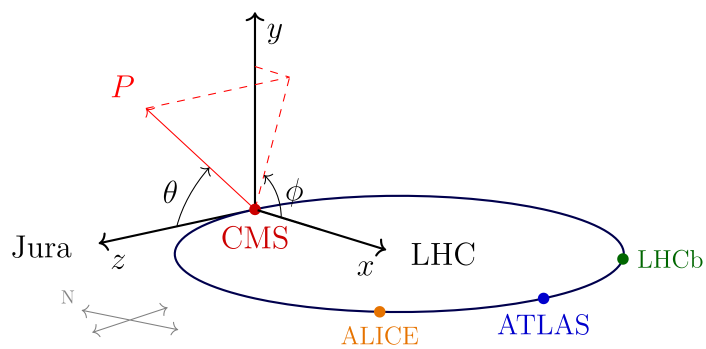

Figure 5.1: *The CMS coordinate system defined relative to the Jura mountains and LHC ring*[5].

The majority of the detector sits within the volume of a superconducting solenoid capable of producing a 4 T magnetic field. This solenoid is 6 m in internal diameter and weighs 12,000 tons. The solenoid is responsible for bending the trajectory of all charged particles within the detector allowing high momentum resolution. Within the solenoid lie the tracker, electromagnetic calorimeter, and the hadron calorimeter, listed in order from closest to the beam to furthest. Outside the solenoid lie the muon chambers, interleaved with the iron return yoke.[47] The following sections will discuss each subsystem in more detail. All together the detector measures 21.6 m long and 14.6 m in diameter weighing in at about 14,000 tons. Fig. 5.2 shows a cutout of the detector with the subsystems labelled.

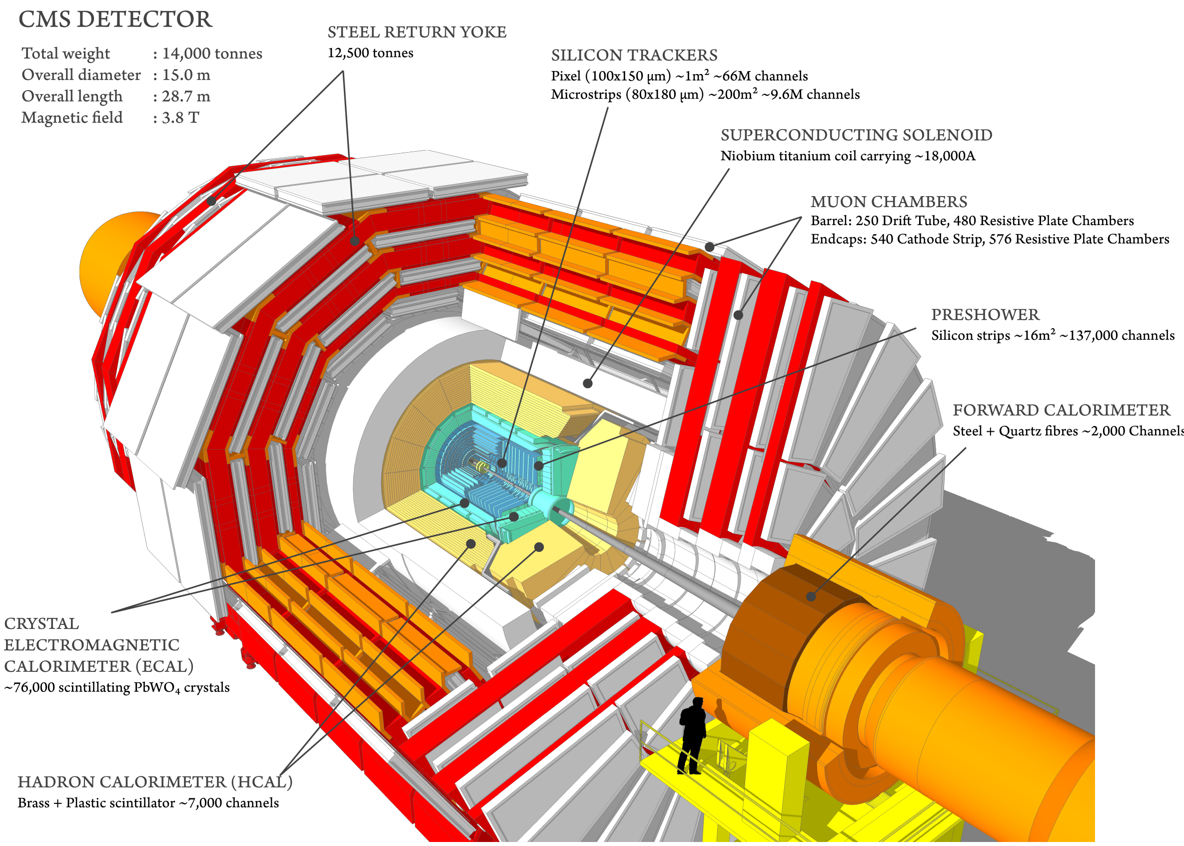

Figure 5.2: *A cross sectional cut out of the CMS detector including a human to show the relative size. The cross section shows the tracker (blue), ECAL (cyan), HCAL (yellow), and muon system (white) interleaved with the steel return yoke of the solenoid (red). The LHC beamline is shown passing through the detector in orange*[6].

5.1 Tracker

The tracker lies closest to the beamline and is responsible for detecting the trajectory of charged particles leaving the interaction point. These trajectories are crucial for both particle identification and momentum resolution. The tracker contains two subsystems, both made entirely of silicon, the pixel detector and the silicon strip detector covering the area $|\eta| < 2.5$.

The sensor modules in each subsystem contain a p-n junction between two silicon semiconductors which are connected to an anode and cathode. When a charged particle passes through the sensor material, it creates electron-hole pairs which are free to move in the electric field. The movement of electrons and holes produces a current which is amplified and then read out as a "hit" in the sensor. These sensors provide much better spatial resolution than detectors using other methods like gas ionization and are much faster allowing them to keep up with the 25 ns frequency of collisions.

Silicon detectors are generally more prone to radiation damage than gas ionization detectors and are also relatively more dense. Because the tracker is closest to the beamline, special consideration must be given to producing a radiation hard silicon detector. Additionally, a strict material budget must be imposed on the tracker such that particles are allowed to pass through the detector with minimal impediment.

The inner layers of the tracker are composed of 100 μm by 150 μm silicon pixels arranged in 3 layers for 2016 then upgraded to 4 layers during the 2016-2017 technical stop[45]. The layout of the pixel detector is shown in Fig. 5.3. Directly outside the pixel detector lies the silicon strip detector with 10 layers of silicon strips in the barrel region, 3 layers in the inner endcap region, and 9 layers in the outer endcap region. The silicon strips provide much coarser resolution than the silicon pixels, but are required to provide full coverage without gaps.

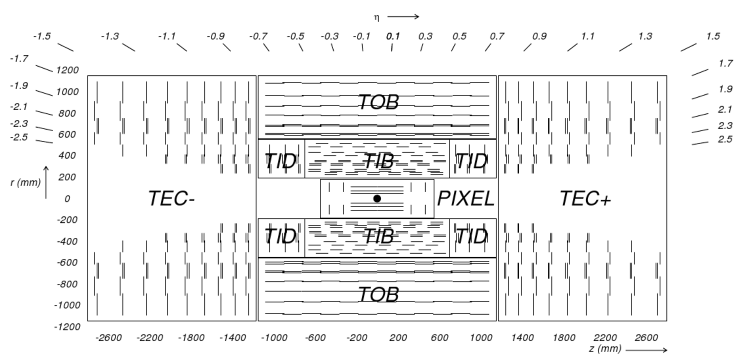

Figure 5.3: *Schematic of the CMS tracker in 2016 centered on the interaction point. The $z(mm)$ denotes the distance in mm along the beamline from the interaction point while $r(mm)$ denotes the distance from the interaction point in the radial direction. The pixel detector, shown here with three layers, was upgraded to contain four layers in 2017. The silicon tracker segments are labeled TIB (tracker inner barrel), TID (tracker inner disk), TOB (tracker outer barrel), and TEC (tracker endcap)*[7].

The combination of pixels and strips provides measurements along multiple points of each particle's trajectory. These measurements are used to accurately measure the particle's momentum and are used as seeds for reconstructing the path of multiple types of particles through the detector. Additionally, the layers facilitate high precision measurements of vertices which arise away from the primary interaction point, known as secondary or displaced vertices.

5.2 Electromagnetic Calorimeter

The electromagnetic calorimeter (ECAL) surrounds the tracker and is designed to measure the energy and position of particles which interact electromagnetically. It is constructed primarily from lead tungstate crystals and photo-detectors to measure electromagnetic energy via scintillation.

When a charged particle with high energy encounters a heavy nucleus, the particle will emit photons via bremsstrahlung (breaking) radiation. Provided the energy of the initial particle was large, the radiated photons will have enough energy to pair produce electrons and positrons which will also emit bremsstrahlung radiation. This process will continue until the emitted photons are no longer energetic enough to pair produce at which point they can be absorbed by a scintillating material. This processes is referred to as “showering”. The scintillator will emit light at a fixed wavelength which can be detected by photodetectors. The number of photons collected by the photodetector will be directly proportional to the energy of the initial particle. It is easy to see that photons are measured in the exact same manner starting from the pair production step.

The precise energy thresholds depend on the properties of the detector material. The lead tungstate crystals used in the ECAL have the following ideal properties: high density, heavy nuclei, short radiation length (X_0), and short scintillation time. The short radiation length (0.89 cm) allows the crystals to be small while still being able to completely absorb the incoming particle. The short scintillation time is vital to ensure the majority of scintillation is complete within the 25 ns interval between collisions.

The central region of the detector ($|\eta| < 1.479$) contains the barrel ECAL (EB). The EB is made of 61,200 crystals arranged into 36 supermodules of 1,700 crystals each. The crystals are designed to be $25.8 \cdot X_0$ to allow complete showering for high energy particles.

The crystals are shaped such that the area facing the interaction point is smaller (22 x 22 m^2) than the outer end (26 x 26 m^2). To avoid gaps between adjacent crystals, each crystal is skewed 3° with respect to the vector connecting the interaction point. Silicon avalanche photodiodes are used to detect the scintillation light.

The endcap ECAL (EE) extends $1.479 < |\eta| < 3$. Each side is split into two semicircles of 3662 crystals called "Dees". The crystals are shaped similar to those in the EB with a front area 28.62 x 28.62 m^2, a read area 30 x 30 m^2, and a length of $24.7 \cdot X_0$. The EE uses vacuum phototriodes instead of avalanche photodiodes to handle the increased radiation load.

Fig. 5.4 and Fig. 5.5 depict the layout of the ECAL subsystems and the components of those systems.

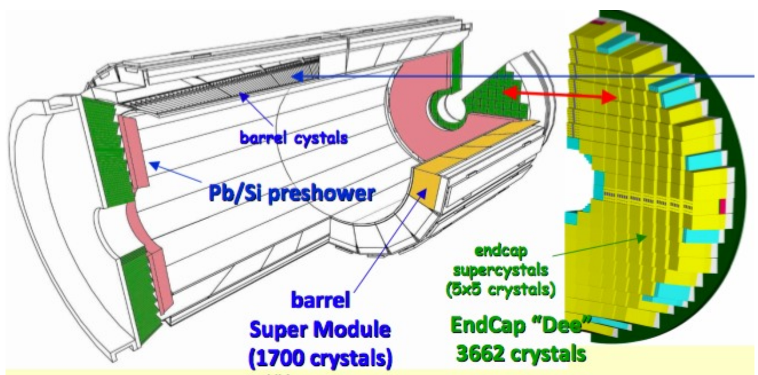

Figure 5.4: *A schematic of the ECAL showing the EB (yellow), EE (green), and ES (pink). The cutout shows a single "Dee" which makes up half of one endcap*[8].

Neutral pions are produced in abundance at the LHC and decay >98% of the time to a pair of photons. As $|\eta_{\pi^0}| \to \infty$, the pion's decay products become increasingly collinear and may begin appearing in the detector as a single, high energy photon. The ECAL preshower detector (ES) sits directly in front of the EE to help disentangle these two cases. The ES covers the region $1.653 < |\eta| < 3$. While the EB and EE are homogenous calorimeters, the ES is a sampling calorimeter containing alternating layers of lead and silicon strip detectors. The lead layers initiate showering while the silicon strip detectors measure the development of showers through the detector. Together, these layers provide the increased resolution necessary to greatly decrease the rate of misidentification.

The energy resolution of the ECAL can be modeled as three independent terms which

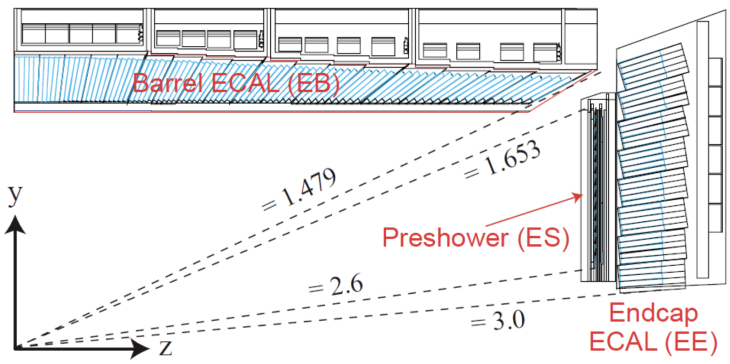

Figure 5.5: *A diagram showing the arrangement of crystals in the EB and EE with the ES sitting in front of the EE. Dashed lines are shown at multiple pseudorapidity values corresponding to to the cutoff of different subsystems. It can be seen that there is a gap between the EB and ES coverage from* $1.479 < |\eta| < 1.653$[9].

add in quadrature to give the overall energy resolution Eq. 5.4. The simplest term is the constant term (C) which is determined based on the calibration of the ECAL crystals. The noise term (N) accounts for the electronic noise in the readout chain which scales as 1/E in Eq. 5.4 because the noise is independent of the particle energy. The last term is called the stochastic (S) term. Because the measurement of energy in the ECAL comes down to counting photons, the resolution scales as any other Poisson process $\frac{1}{\sqrt{N_\gamma}}$ which is equivalent to $\frac{1}{\sqrt{E}}$ in Eq. 5.4. The values for C, S, and N are determined empirically to be $C = 0.003$, $S = 0.028$, and $N = 0.12$.

$$\left(\frac{\sigma}{E}\right)^2 = \left(\frac{S}{\sqrt{E}}\right)^2 + \left(\frac{N}{E}\right)^2 + C^2 \tag{5.4}$$

5.3 Hadron Calorimeter

The Hadron Calorimeter (HCAL) is a sampling calorimeter designed to measure the energy of charged and neutral hadrons. The HCAL operates on principles similar to the ECAL, but utilizing principles of QCD rather than QED. When a high energy hadron encounters a heavy nuclei, a showering process begins with gluons pair-producing quarks and quarks pair-producing more quarks due to the color confinement which arises in QCD. From this point, the showering progresses via numerous processes. Once the decay products drop below the energy threshold required to continue showering, they can be absorbed by scintillators and measured.

The HCAL is constructed of alternating layers of brass and plastic scintillator to account for the fact that the nuclear interaction length (λ_0) is much longer than the radiation length relevant in the ECAL. The brass layers have a short interaction length to help facilitate the completion of showering within the calorimeter while the plastic calorimeter layers provide the ability to sample the development of the showers through the calorimeter. As the scintillators absorb particles from the shower, they emit light which is collected and carried by wavelength shifting fibers to the electronic readout boxes. The light from each layer of scintillator is optically summed to construct an HCAL "tower". The tower can then be used to measure the energy of the particles which initiated the shower. Lastly, the towers are converted to electronic signals by special hybrid photodiodes.

The HCAL is split into a barrel (HB) and endcap (HE) just like the ECAL and is shown in Fig. 5.6. The HB covers the region $|\eta| < 1.4$ with 36 "wedges" parallel to the beam wrapping around in ϕ-space. Each wedge contains a 40 mm thick steel plate on the inside and a 75 mm steel plate on the outside to provide structural support. The total thickness of the HB is $5.82 \cdot \lambda_0$ in the central region and increases with pseudorapidity. To increase the HCAL thickness in the central region, an additional calorimeter called the outer calorimeter (HO) is placed outside the the solenoid. The HO contains a single layer of scintillator and uses the material of the solenoid as an absorber layer to initiate showering. The addition of the HO bring the total thickness of the HCAL in the central region to $11.8 \cdot \lambda_0$.

The HE is also composed of 36 azimuthally displaced wedges covering the region $1.3 < |\eta| < 3$. This design intentionally provides an overlap with the furthest forward region of the HB. While the HB contains eight 50.5 mm thick brass absorbers followed by six 56.5 mm thick brass absorbers, the HE contains consistent 79 mm thick brass absorbers leading to a thickness of $10\lambda_0$.

The HCAL has an additional responsibility to provide information about invisible particles. Provided the detector forms a hermetic seal, invisible particles can be detected by

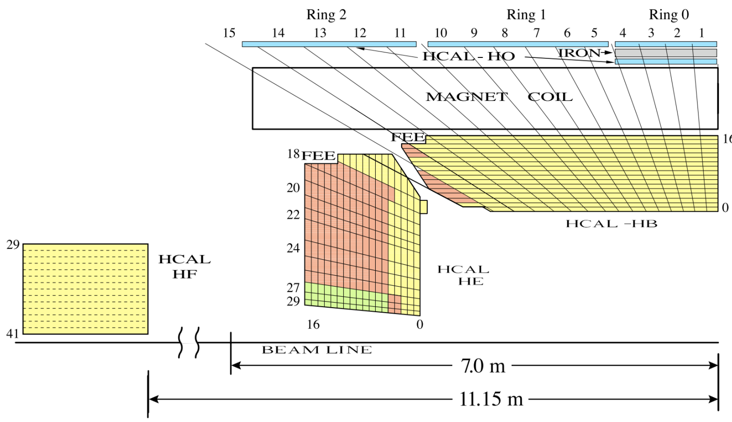

Figure 5.6: *A diagram showing one quarter of the HCAL with each subsystem included. The number on top and left denote η segmentation while the numbers on right and bottom label scintillator layers. The four colors denote differing thicknesses*[10].

the presence of "missing" energy. That is an energy imbalance when the momenta of all particles is summed. To improve the hermeticity of the HCAL, a very forward detector (HF) covers $3 < |\eta| < 5$. This region is constantly bombarded with radiation and the detector must be designed to be exceptionally radiation hard. For this reason, the HF is designed as a Cherenkov detector where quartz fibers are embedded in steel absorbers. Particles passing through the quartz faster than a photon travels in quartz will emit Cherenkov radiation. This radiation can be detected and provide a measurement of the initial particle's energy.

The energy resolution of the HCAL is

$$\left(\frac{\sigma}{E}\right)^2 = \left(\frac{S}{\sqrt{E}}\right)^2 + C^2 \tag{5.5}$$

where there is no noise term. Measured using cosmic rays, $S = 0.847\ \text{GeV}^{1/2}(1.98\ \text{GeV}^{1/2})$ and $C = 0.074\ \text{GeV}^{1/2}(0.09\ \text{GeV}^{1/2})$ for the HB/HE and HF respectively.

5.4 Solenoid

A superconducting solenoid magnet surrounds all previously described layers providing an exceptionally uniform magnetic field within the detector. The solenoid operates at 3.8 T while being capable of producing a full 4 T field. By running the solenoid slightly below it's maximum capability, the lifetime of the solenoid is extended. The solenoid is made of 4 layers of wound NbTi cables coated in pure aluminum and reinforced with an aluminum alloy. It is 12.5 m long, 6.3 m in diameter, and weighs 220 tons. A 10,000 ton iron return yoke guides the field outside the solenoid and acts as a filter to allow only muons and invisible particles into the muon system. The solenoid requires a nominal current of 19.14 kA and operates at 4.5 K.

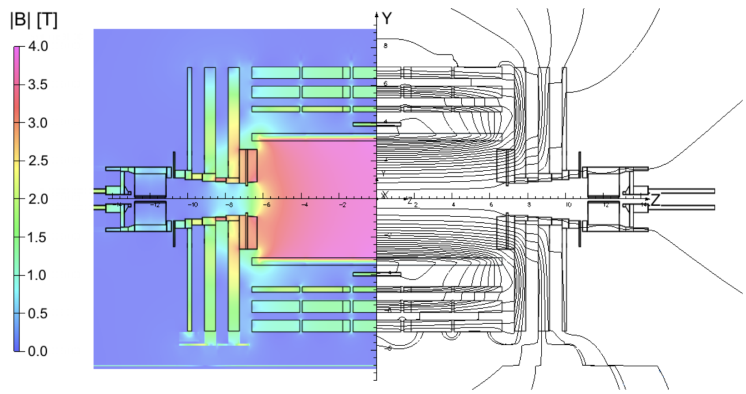

Figure 5.7: *Magnetic field strength (left) and predicted field lines (right) for the superconducting solenoid magnet in the CMS detector*[11].

The solenoid produces a uniform field along the beam line in order to bend the trajectory a charged particles. The benefit is two-fold. First, the direction a track is bent allows us to easily determine the charge of the particle. Second, the curvature of the particle's track provides a highly accurate measurement of the particle's momentum. Even with a 3.8 T field, most particles are so energetic that the observed curvatures can be quite small. This is one reason why a high precision tracker is really crucial.

5.5 Muon System

Because the rate of energy loss due to bremsstrahlung radiation scales as either m^{-4} or m^{-6}, most muons are able to escape the ECAL (and HCAL) without losing any noticeable amount of energy. Most other particles will be stopped by the calorimeters and the iron return yoke of the solenoid. The muon system, as the name suggests, is designed explicitly to handle the muons that punch through the rest of the detector. The muon system is interleaved with the iron return yoke. While some high energy particles may even punch through the first layer of the return yoke, it's very unlikely anything besides muons will traverse all layers of the muon system.

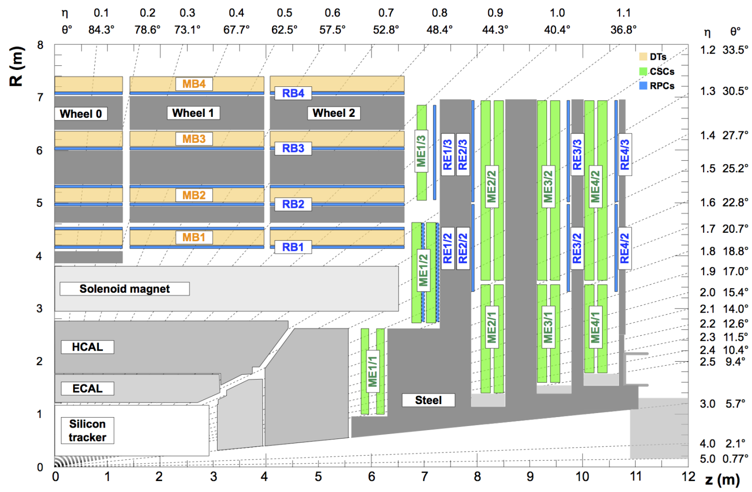

Figure 5.8: *Diagram showing the muon system in relation to the rest of the detector for one quadrant. The layering of DTs and RPCs in the barrel, labeled MB and RB, respectively, are shown between the wheels of the return yoke. In the endcap, CSCs and RPCs are layered up to* $|eta| < 1.9$ *and interleaved between the wheels of the steel return yoke*[12].

The muon system is composed of 3 different types of muon chambers for a total of 1400 chambers. Muon drift tubes (DT) are located only in the barrel $|\eta| < 1.2$, while cathode strip chambers (CSC) are located only in the endcaps $0.9 < |\eta| < 2.4$. Resistive plate chambers (RPC) are located throughout the entirety of the barrel extending partially into the endcap region $|\eta| < 1.9$. The RPCs are mixed in with the other chambers in each region. This layout is shown in Fig. 5.8.

Muon drift tubes provide a 2D image of the muon's trajectory through the barrel region of muon system. Each DT contains aluminum strips that are held at a constant 4800V potential difference with respect to a single 2.4 m long wire stretched down the middle of the tube. The remaining volume of the tube is filled with a mixture of argon and carbon dioxide. When a muon passes through the tube, the gas ionizes and the resulting charged particles are accelerated by the potential difference towards the wire. This creates a current in the wire that can be read to indicate a hit. DTs are an excellent choice for the barrel region where the muon rate is low and the magnetic field is uniform. The DTs are arranged into four stations between layers of the return yoke. The first three layers contain four DTs measuring in $r-\phi$-space and four DTs measuring in the z-direction. The fourth layer contains only DTs in the $r-\phi$-space orientation.

The drift tubes from the barrel region are a poor choice for the endcap where muon flux is much higher and the magnetic field becomes non-uniform. A faster, more radiation hard version of the drift tubes are the cathode strip chambers. Instead of a single wire stretched through the tube, CSCs contain closely spaced anode wires perpendicular to copper cathode strips. Now when a muon ionizes the gas, the free electrons will be collected by the anode while the ions are collected by the cathode strips. Because the wires can be placed very close together, the CSCs are more capable of handling the high muon flux in the endcaps.

Resistive plate chambers provide extremely fast measurements necessary for the trigger system. The chambers are constructed from two highly resistive plastic plates which are held at a large potential difference. The space between the plates is filled with gas that ionizes when a muon passes through the chamber. The free electrons are then accelerated through the gap and collected by an array of strips outside the plates. The RPCs in the muon system are operated in "avalanche mode" where the chamber is configured such that the freed electrons are able to ionize the gas freeing more electrons. The result is an avalanche of electrons caused by a single muon. While this provides an extremely fast measurement, the spatial resolution is lower than that of DTs and CSCs. For this reason, RPCs are generally utilized for triggering where speed is more important than precision.

The muon system does not contribute much to the energy resolution of low energy muons which can be handled with the tracker. At muon $p_T > 200$ GeV, the muon system significantly increases the tracker-only muon energy resolution from 10% to 6% at $p_T = 1000$ GeV.

5.6 Triggers

The LHC produces events at 40 MHz, a rate too high to process and which would result in much more data than could possibly be stored. Luckily, most events are relatively uninteresting and can be discarded by an intelligent triggering system. The CMS experiment consists of a level one (L1) trigger system designed to decrease the rate to 100 kHz followed by a high-level (HLT) trigger system which further reduces the rate to a manageable 1 kHz.

The L1 trigger combines low resolution calorimeter information with sparse information from the muon system to select events within a 4 μs interval. This is possible with the use of field programmable gate arrays (FPGA) and application specific integrated circuits (ASIC). Both FPGAs and ASICs provide a way implement algorithms in hardware allowing the system to perform a single task extremely efficiently.

The HLT is able to run a trimmed version of the full event reconstruction on a dedicated farm of computers. HLTs are implemented as HLT paths which define a set of reconstructions and basic selections to be performed in a specified order. The logical OR of all HLT paths is used to decide if an event should be kept. Provided the event is retained, a set of flags are stored indicating which paths were satisfied by the event.[48]

Chapter 6

Object Reconstruction

The particle flow[49] (PF) algorithm constructs PF candidates by combining the information from all detector subsystems. Physics objects can then be constructed using these PF candidates as building blocks. Because there can be multiple collisions within a single bunch crossing, it is important to define a primary pp vertex. When determining the primary vertex, we restrict our physics objects to only jets constructed by a clustering algorithm run over all charged tracks. The vertex with the highest summed p_T for all jets is designated the primary vertex. All other vertices are considered pileup vertices.

6.1 Triggers

The CMS experiment provides a robust menu of HLT trigger paths which determine whether an event is recorded or not. Each trigger path provides a set of events passing a predefined selection and can be used to select only the subset of all triggered events which are interesting for a given analysis. Because the final states of interest in this analysis contain either an electron or muon from a tau lepton decay, a logical choice of trigger path will be one that fires for events with an isolated muon or electron. These triggers are referred to as isolated, single lepton triggers. The trigger system is designed to maintain a set event rate which means that as luminosity increases, the selection applied by the trigger system must become more stringent. This usually takes the form of a higher p_T cut on the triggering objects. To recover some of the more interesting events below the p_T thresholds imposed by the single lepton triggers, more complex triggers, called cross-triggers, are developed. These cross triggers require multiple objects to be identified in an event allowing the p_T threshold on each object to be lowered while maintaining an acceptable event rate. For this analysis, cross-triggers requiring the identification of a hadronically-decaying tau lepton in addition to an isolated electron or muon allow for the recovery of events where the lepton p_T is below single lepton trigger thresholds. This is done by requiring that events fire a single lepton trigger OR the cross-trigger.

The HLT trigger system is required to run a faster, slimmer version of the full CMS reconstruction described below. As a result, the selection on fully reconstructed objects is required to be marginally tighter than the HLT trigger selection to account for any inefficiencies.

6.2 Electron

Electrons traveling through the detector leave hits in the silicon detector and then interact with the ECAL leaving clusters of energy surrounding the interaction point. To reconstruct the electron track, the energy clusters in the ECAL are matched to track seeds in the pixel detector. The seeds are constructed by grouping together hits in the pixel detector. Electrons can lose energy due to bremsstrahlung radiation while traversing the tracker material. While the Kalman[50] filter is used for for most track reconstruction, the Gaussian sum filter is used for reconstructing electron tracks to account for the energy lost due to bremsstrahlung. The Gaussian sum filter is a generalization of the Kalman filter in which the energy loss is modeled as a sum of Gaussians rather than a single Gaussian as is used in the Kalman filter. This has been shown to improve the momentum resolution of the reconstructed electrons.[51;52]

Multivariate techniques are utilized in order to further distinguish electrons from other charged particles which may behave similarly in the detector. These MVA techniques combine information about ECAL shower shapes, the impact parameter, the ratio of energy in the HCAL and ECAL, and additional information from the track reconstruction and matching to create a discriminant which efficiently identifies electrons.

The electron isolation, defined in Eq. 6.1, measures the amount of activity surrounding the electron in the detector using the ratio of the sum transverse momenta of all charged hadrons, neutral hadrons, and photons in a cone centered on the electron to the transverse momentum of the electron itself. The PU term is used to account for particles within the isolation cone that originate from pileup vertices and varies by analysis. If an electron is isolated, the electron's transverse momentum should be much larger than the sum of all surrounding momenta resulting in a small ratio.

$$I_e = \frac{\sum\limits_{i \in charged} p_{T_i} + \max\left(0, \sum\limits_{i \in neutral} p_{T_i} + \sum\limits_{i \in photon} p_{T_i} - PU\right)}{p_{T_e}} \tag{6.1}$$

For this analysis, electrons are selected to have p_T 1 GeV greater than the trigger threshold and to be in the central region of the detector $|\eta_e| < 2.1$. Although electrons can be reconstructed out to $|\eta_e| < 2.4$, the single electron triggers further restricts the available phase space. To ensure the electron is coming from the primary interaction, we require that the electron track is less than 0.2 mm removed from the primary vertex in the Z-direction (d_Z) and less than 0.45 mm in the X-Y plane (d_{XY}). Additionally, the electron is required to pass the MVA-based electron ID at a working point corresponding to 90% efficiency. Lastly, to avoid contamination from charged particles within jets faking electrons, we require the electron to be isolated, $I_e < 0.15$, using the rho-correction electron isolation ($PU = A \cdot \rho$). This isolation accounts for the effect of pileup vertices using the effective area of the isolation cone, A, and the average pileup energy density per unit area, ρ, which is measured per event.

6.3 Muon

Muons in the detector will leave hits in the silicon tracker and in the muon chambers. Muon track reconstruction involves a global fit using tracks in the silicon tracker and standalone muon tracks. The tracks are projected onto a common surface where the fit is performed with the Kalman filter. The tracks in the silicon tracker are formed using the standard, iterative method with a Kalman filter. The standalone muon tracks are constructed using only information in the muon system. A similar Kalman filter technique is used to combine information in the muon subsystems and construct the standalone muon track.

Muons are identified using information from the global fit including the χ^2, the number of hits in each track, and the muon segment compatibility. The segment compatibility is calculated by extrapolating the muon track from the pixel detector to the muon chambers. The compatibility is a value bound between 0 and 1 based on how compatible the extrapolated track is with the standalone muon track.[53;54]

Similar to the electrons, muons are selected to have p_T 1 GeV greater than the trigger threshold and must pass within the area of the tracker $|\eta_\mu| < 2.1$. The muon track must be within $d_{XY} < 0.45$ mm and $d_Z < 0.2$ mm of the primary vertex. The muon ID, which consists of multiple variables as previously described, is chosen to provide 99.5% efficiency while maintaining a $< 1\%$ fake rate. In addition to the muon ID, a muon isolation cut $I_\mu < 0.15$ is applied to reduce the contribution of muons coming from anything besides the tau decay. The muon isolation is defined using Eq. 6.1 with $PU = \frac{1}{2} \sum_{i \in PU} p_{T_i}$ where PU refers to particles coming from a pileup vertex.

6.4 Tau Leptons

Tau leptons are heavy enough to decay within the detector meaning they may be detected only through their decay products. The tau decays via the weak interaction meaning it is capable of decaying both leptonically ($\mathcal{B} \sim 1/3$) and hadronically ($\mathcal{B} \sim 2/3$). Individual methods are used to identify taus decaying in leptonically or hadronically.

Identifying leptonically decaying taus is simple by comparison and involves identifying the lighter lepton to which the tau decayed along with nonzero MET corresponding to the energy carried away by neutrinos. These taus can easily be faked by electrons or muons produced in other processes.[55]

Hadronically decaying taus are identified using the hadrons-plus-strips (HPS) algorithm which is seeded using jets. The HPS algorithm starts by identifying "strips" to take into account photon conversion in the material of the CMS detector. Strip construction starts by identifying the most highly energetic PF photon or electron in the event. The strip then iteratively grows to include the next most energetic particle within a window of size $\Delta\eta = 0.05$ and $\Delta\phi = 0.20$ until all particles satisfying the criteria are included. If the total transverse momentum of the strip is greater than 1 GeV, the strip is then combined with charged hadrons to reconstruct one of four possible tau decay modes: single hadron, single hadron plus one strip, single hadron plus two strips, or three hadrons. The terminology used in the rest of this thesis will refer to hadronic taus based on the number of charged hadrons called "prong". For example, a tau decaying to three charged hadrons will be referred to as a three-prong tau. The HPS algorithm is also capable of reconstructing taus which decay to two charged hadrons which isn't physically possible, but is included to help recover events where a tau decays to three charged hadrons and one hadron escapes detection. Once the matching is done, the τ_h four momentum is reconstructed assuming each hadron to be a pion and requiring the τ_h mass to fit within an appropriate mass window depending on the decay mode.[56;57]

Due to the nature of τ_h reconstruction, it is fairly easy for an electron, muon, or jet to be incorrectly identified as a τ_h candidate. In this instance, we say the object "fakes" a τ_h. The DeepTau algorithm[58] was created in order to efficiently identify isolated τ_h candidates while rejecting possible fakes. The DeepTau algorithm is implemented as a deep neural network trained using a large number of features including all the inputs to the HPS algorithm. The algorithm returns the probability that the τ_h candidate falls into each of the four possible classes: muons, electrons, quark or gluon jets, or real τ_h. Ratios of these output probabilities can be used to reject different sources of fakes τ_h's with different tolerances. For example, an anti-electron discriminator can be formed using the ratio of two the probabilities shown in Eq. 6.2.

$$\mathcal{D}_e = \frac{\mathcal{P}_\tau}{\mathcal{P}_\tau + \mathcal{P}_e} \tag{6.2}$$

In this analysis, hadronic taus are generally required to have $p_T > 30$ GeV and $|\eta_{\tau_h}| < 2.3$. For events that fire the cross-trigger, the hadronic tau selection is updated to be slightly tighter than the selection applied by the trigger to account for any inefficiency. Additionally, a selection is made on the tau impact parameter, $d_Z < 0.2$ mm. While the two-prong decay mode does recover some mis-reconstructed taus, it leads to a significant increase in the number of fake taus. For this reason, we reject events with two-prong taus in this analysis. To reduce the contamination by fake taus coming from jets, muons, and electrons, we require hadronic taus to be identified as genuine taus by the DeepTau algorithm.

6.5 Jets

Particle flow candidates are clustered into jets using the anti-kt algorithm[59;60] implemented in FastJet[61;62]. The anti-kt algorithm iteratively clusters neutral and charged particle flow candidates based on the transverse momentum of the candidates and the distance between candidates. The softest candidates are iteratively added to the closest hard candidate resulting in circularly shaped jets in the η-ϕ plane.

The momentum of each charged candidate is measured by the tracker and is matched to energy deposition in the ECAL and HCAL to measure the candidate's energy. Charged candidates not associated with the primary vertex are removed in order to reduce the effect of pileup. The tracker can not be used to measure the momentum of neutral candidates so the energy is taken directly from the corrected energy measured in the ECAL and HCAL. To reduce the effect of neutral hadrons coming from pileup, each jet's transverse momentum is corrected[63] based on the jet's area[64], A_j, and the amount of noise measured in the event, ρ. The correction is shown in Eq. 6.3

$$p_{T_j}^{corr} = p_{T_j} - A_j\rho \tag{6.3}$$

The jets are then corrected for residual differences observed between data and simulation.

During the 2017 run, large amounts of noise were observed in the ECAL endcaps leading to discrepancies between data and simulation. All jets with $p_T > 50$ GeV and $2.65 < \eta < 3.138$ must be removed as result of the observed discrepancies. This discrepancy is not observed in other runs and therefore no jets in those runs require removal.

Jets containing the decay products of a bottom quark (b-jets) are identified using the DeepCSV algorithm[65]. When the bottom quark decays, it first forms a neutral B meson, which will travel a detectable distance in the tracker before decaying. This results in a secondary vertex; a vertex, displaced by some distance from the primary vertex, from which a jet originates. The DeepCSV algorithm combines information about secondary vertices and candidate lifetimes in a neural network to give the probability that the jet originated from a bottom quark. Jets passing a chosen DeepCSV threshold are considered b-jets. In this analysis, events which have an identified b-jet are rejected to suppress the $t\bar{t}$ background.

6.6 MET

To account for energy carried away by undetectable particles, neutrinos for instance, the missing transverse energy (p_T^{miss}) is defined as the negative vector sum of all particle flow candidates.[66]. Because p_T^{miss} requires information about the entire event, it is sensitive to detector errors which lead to particles escaping detection. To ensure a proper description of p_T^{miss}, event filters are applied which remove events with known detector issues.

Chapter 7

Event Selection

7.1 Final States

Although this analysis probes four different Higgs production mechanisms, a single final state can be used to study all four mechanisms. Clearly, each final state will contain a ditau pair with invariant mass near the Higgs mass in which one tau lepton decays hadronically and the other decays leptonically producing an electron or muon. Because the Higgs will typically be produced with low momentum, it is reasonable to assume the tau decay products will frequently be produced back-to-back, meaning with momentum vectors pointing in nearly opposite directions. The tau leptons clearly must have opposite charges to have been produced by the neutrally-charged Higgs boson. Because the tau lepton decays weakly, there will also be a significant amount of missing transverse energy due to the presence of neutrinos.

The primary difference between the four production mechanisms is the multiplicity and type of particles produced in association with the Higgs. In the VBF production mode, the Higgs is produced in association with two jets. In the ggH production mode, the Higgs is produced with no additional particles. While this appears to lead to different final states, we know the couplings can only be probed using the correlation between particles produced in association with the Higgs. For VBF and ggH production, this means our final state is required to contain at least two additional jets in order to provide sensitivity to anomalous couplings. Because ggH production of the Higgs does not require any associated particles, only events in which two jets are radiated by initial state gluons will be sensitive to anomalous couplings in the Hgg vertex. In practice, we can squeeze additional sensitivity out of the analysis by retaining events with any jet multiplicity and then applying a categorization as described in Chapter 8. The additional jets will also be very far forward in the detector which can be expressed as a selection on the invariant mass of the dijet system. This fact is also used in the event categorization.

In summary, the final state which provides access to anomalous Higgs couplings will contain at least two jets, one hadronically decaying tau lepton, an electron or muon, and a non-zero amount of missing transverse energy. The hadronically decaying tau lepton will have opposite sign and be back-to-back to the electron or muon. The invariant mass of the hadronic tau, electron or muon, and missing energy should be consistent with the Higgs mass. The dijet system is expected to have a large invariant mass.

7.2 Background Processes

Different physics processes producing signatures similar to the final state, called background processes, can be split into two groups: reducible and irreducible. The reducible backgrounds are those that are expected to produce a different final state, but contribute to our final state of interest due to imperfect measurement of the event. These events are called reducible because the contribution of these processes could be further reduced by improving our measurements. The irreducible backgrounds are those which truly produce an identical final state and are therefore unable to be further reduced. The only way to decrease the contribution of irreducible backgrounds is to accept the loss of signal events as well.

This analysis is dominated by two backgrounds, one is reducible and the other is irreducible. The largest contribution comes from the irreducible background: Drell-Yan production of $Z \to \tau\bar{\tau}$ with two additional jets. In this case, the ditau pair is genuine and, while the ditau mass should peak near the Z boson mass, the mass resolution is not sufficiently high to avoid overlap between the Z boson and the Higgs boson events. Despite the overlap between these two processes, the ditau mass does provide the most separation power between $Z \to \tau\bar{\tau}$ and $H \to \tau\bar{\tau}$. As a result, advanced methods are necessary to provide a high resolution mass reconstruction.

The second largest background contribution comes from what is referred to as the QCD background. This process involves the production of numerous jets via the strong interaction. Because the hadronic tau reconstruction is seeded with jets, it is common for the QCD interaction to produce a jet which is misidentified as a hadronically decaying tau lepton. This is clearly a reducible background because as our hadronic tau identification improves, the contribution from this processes decreases. Provided we could perfectly identify tau leptons, the contribution from QCD processes could be reduced to zero. Due to imperfections in tau identification, we need additional selection to reduce this background. Because the jets produced by QCD are random, it is equally likely for the misidentified tau to have either charge. As a result, this background is reduced by a factor of two by requiring the ditau pair to have opposite charges. The ditau mass is also useful to distinguish QCD events in which the invariant mass does not have a resonant structure.

Other backgrounds, both reducible or irreducible, provide much smaller contributions. These include $t\bar{t}$ production in which a high energy gluon pair produces a top anti-top quark pair which decays to W bosons and b-quarks. One of the W bosons can decay leptonically producing an electron or muon and a neutrino similar to a leptonically decaying tau. The other W boson can decay hadronically producing a jet that can be misidentified as a hadronically decaying tau lepton. Rejecting events with a b-jet which are not expected in the signal process significantly reduces this background. The production of a single top provides an even smaller background contribution and is similarly rejected by vetoing events with b-jets. Diboson production can fake the final state in a way similar to $t\bar{t}$, but has much smaller contribution due to a lower cross section and is heavily suppressed by the event selection. Lastly, the production of a single W boson with additional jets when one of these jets is misidentified as a hadronic tau lepton. The W+jets contribution can be heavily suppressed by applying a cut on the transverse mass (m_T) Eq. 7.1 of the lepton and MET system. Be-

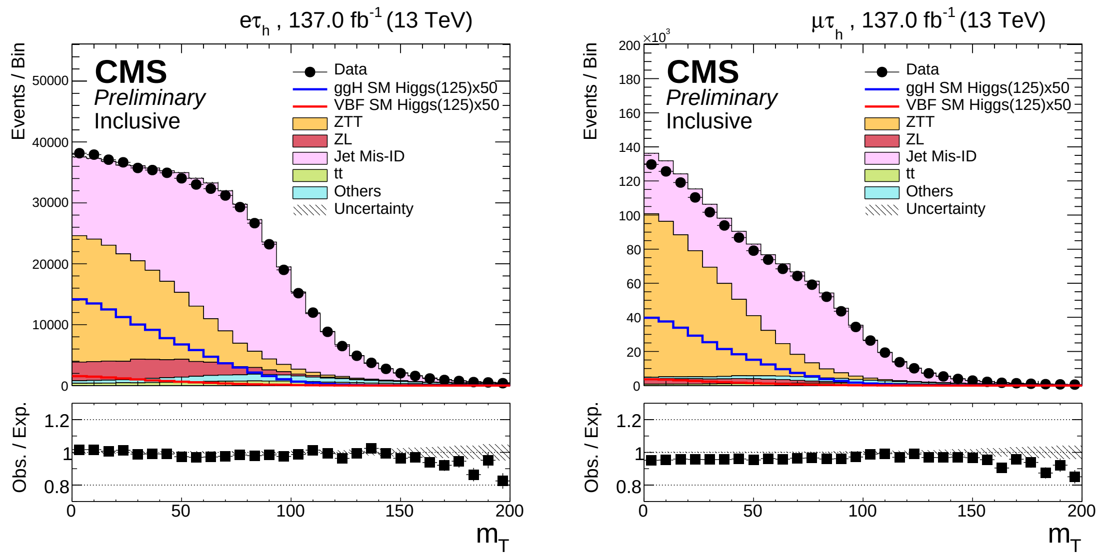

Figure 7.1: *The transverse mass in the $\tau_e\tau_h$ (left) and $\tau_\mu\tau_h$ (right) channels. A cut is placed at $m_T > 50$ GeV to reduce the contribution from the W+jets process which is the dominant contribution to the jet fakes background in this region.*

cause the W boson mass is roughly 45 times larger than the tau lepton mass, the m_T should be significantly larger for W+jets than for the signal processes.

$$m_T = \sqrt{(p_T^\ell + p_T^{miss})^2 - (p_x^\ell + p_x^{miss})^2 - (p_y^\ell + p_y^{miss})^2} \tag{7.1}$$

7.3 Selection

This section provides the exact values for the selection criteria discussed in the previous sections. For the motivation behind each criterion, refer to the corresponding section. The value for each cut was optimized to reduce background contributions while maintaining signal efficiency.

7.3.1 Triggers

The trigger menu evolved over time and, as a result, is different between three eras of data-taking used in this analysis. Table 7.1 lists online p_T thresholds for the single lepton triggers for each data period and channel while Table 7.2 shows the online p_T thresholds for each leg of the cross triggers. The offline p_T selection is chosen to be slightly higher than the online selection to account for inefficiencies in the triggers.

	Single Electron	Single Muon
2016	25	22
2017	32/35	24/27
2018	32/35	24/27

Table 7.1: *p_T thresholds for single lepton triggers. The single electron trigger is used in the $\tau_e\tau_h$ channel and the single muon trigger is used in the $\tau_\mu\tau_h$ channel. Because the trigger menu changed over time, the thresholds in 2017 and 2018 changed partially through data-taking.*

	$\tau_e\tau_h$ - lepton leg	$\tau_e\tau_h$ - tau leg	$\tau_\mu\tau_h$ - lepton leg	$\tau_\mu\tau_h$ - tau leg
2016	None	None	19	20
2017	24	30	20	27
2018	24	30	20	27

Table 7.2: *p_T thresholds for each leg of the cross triggers.*

7.3.2 Electron Selection

Electrons are required to have p_T slightly above the online threshold in the trigger system and are required to be within the region $\eta < 2.1$. The electrons are required to pass an MVA-based identification algorithm at a working point corresponding to 90% efficiency and are required to be well isolated, $I_e < 0.15$ using the definition in Eq. 6.1. The electron track must pass near the primary vertex: $d_Z < 0.2$ mm and $d_{XY} < 0.45$ mm.

7.3.3 Muon Selection

Muons are required to have p_T slightly above the online threshold in the trigger system and are required to be within the region $\eta < 2.1$. The electrons are required to pass an identification algorithm at a working point corresponding to $> 95\%$ efficiency and are required to be well isolated, $I_\mu < 0.15$ using the definition Eq. 6.1. The muon track must pass near the primary vertex: $d_Z < 0.2$ mm and $d_{XY} < 0.45$ mm.

7.3.4 Tau Selection

The hadronically decaying tau selection is nearly identical in both channels. The tau must have a small impact parameter, $d_Z < 0.2$ mm, and must pass the anti-jet discriminator from the DeepTau ID at 70% efficiency. The baseline tau selection requires $p_T > 30$ GeV and $|\eta| < 2.3$. The cross trigger requires a tighter selection $|\eta| < 2.1$ and a slightly higher p_T threshold in the $\tau_e\tau_h$ channel for 2017 and 2018: $p_T > 35$ GeV.

Selection criteria are applied to veto events with two-prong taus and events where the tau charge is mismeasured leading to $e_\tau \neq \pm 1$. The tau is also required to pass anti-electron and anti-muon discriminators from the DeepTau ID at different working points depending on the channel. For the $\tau_e\tau_h$ channel, the tau must pass the tight anti-electron working point and very loose anti-muon working point. In contrast, the tau must pass the tight anti-muon working point and very loose anti-electron working point for the $\tau_\mu\tau_h$ channel.

7.3.5 Event Selection

This subsection describes the selection applied to the event as a whole. Each event is required to have exactly one light lepton and at least one hadronic tau passing selection. The lepton and hadronic tau must be oppositely charged and be separated in $\eta - \phi$ space by $\Delta R > 0.5$ where ΔR is

$$\Delta R = \sqrt{(\Delta\eta)^2 + (\Delta\phi)^2} \tag{7.2}$$

In the case of multiple hadronic tau candidates, the sorting defined below is applied

1. Prefer the pair with the most isolated lepton.

2. If the isolation of the lepton candidates is the same, prefer the pair with the highest lepton p_T.

3. If the p_T of the lepton candidates is the same, prefer the pair with the most isolated tau lepton.

4. If the isolation of the tau leptons is the same, prefer the pair with the highest tau lepton p_T.

Any event containing a jet passing the medium working point of the DeepCSV algorithm is vetoed. To reject W+jets, we require $m_T < 50$ GeV with m_T defined in Eq. 7.1. As mentioned, no selection is applied to the jet multiplicity or dijet mass, but instead events are categorized based on these properties as discussed in Chapter 8.

Chapter 8

Categorization

Events are split into categories in order to maximize the overall sensitivity of the analysis. The categories are chosen to be exclusive to avoid any potential difficulties caused by having a single event fall into more than one categories. The combination of all categories covers all phase space preventing a decrease in statistics due to an event slipping between categories. The categories are defined Table 8.1 and the following sections provide a detailed description of each category.

Category	Selection
0-Jet	$N(jets) = 0$
VBF	$N(jets) > 1$ and $m_{JJ} > 300$ GeV
Boosted	all other events

Table 8.1: *Definition of categories.*

8.1 0-Jet Category

The 0-Jet category contains all events in which there is no jet activity aside from the hadronically decaying tau lepton. This region has very large statistics, but the lowest sensitivity because it is dominated by backgrounds. As a result, the 0-Jet region is very useful to constrain the background normalization in the fit. The observables in this region are chosen to give the best constraints on the background normalization. Those variables are the ditau mass and the transverse momentum of the τ_h.

8.2 VBF Category

The VBF category is chosen to target vector boson fusion. Vector boson fusion always produces two associated jets in the forward region; the invariant mass of which is typically larger than that of the jets that are produced in Drell-Yan events, as shown in Fig. 8.1. To target this production, the VBF category requires the event have two or more jets and requires the invariant mass of these two jets (m_{JJ}) to be above a threshold chosen to provide the highest sensitivity. The VBF category also provides sensitivity to gluon-gluon fusion events in which two jets are radiated by gluons. It has been shown that these are precisely the events that provide the highest sensitivity to the coupling of the Higgs. In this category, we utilize the MELA discriminants and neural networks described in Chapter 12.

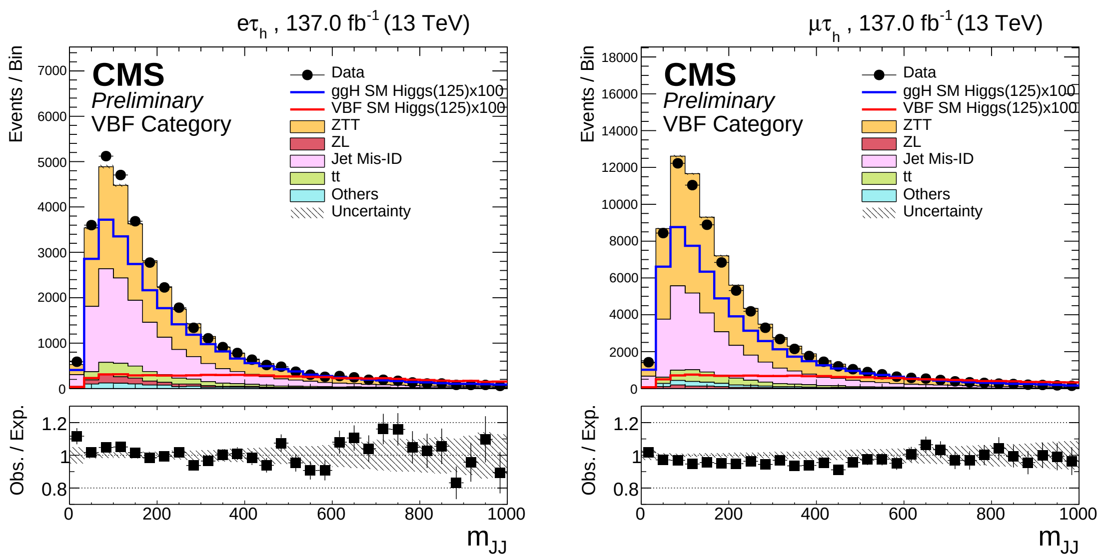

Figure 8.1: *The dijet invariant mass in the $\tau_e\tau_h$ (left) and $\tau_\mu\tau_h$ (right) channels. The VBF category requires $m_{JJ} > 300$ GeV to enhance the contribution of VBF and ggH production.*

8.3 Boosted Category

The boosted category contains all events that do not fit within the 0-Jet or VBF categories. This can include a small fraction of vector boson fusion events with low dijet mass, but provides virtually no sensitivity in the VBF analysis. The boosted category does add some sensitivity to the gluon gluon fusion analysis coming from events with a highly boosted Higgs boson recoiling against a jet. In order to try to access this sensitivity, we fit the visible Higgs p_T (p_T^H) and the ditau mass in the boosted category. The p_T^H distribution for events in the boosted category is shown in Fig. 8.2.

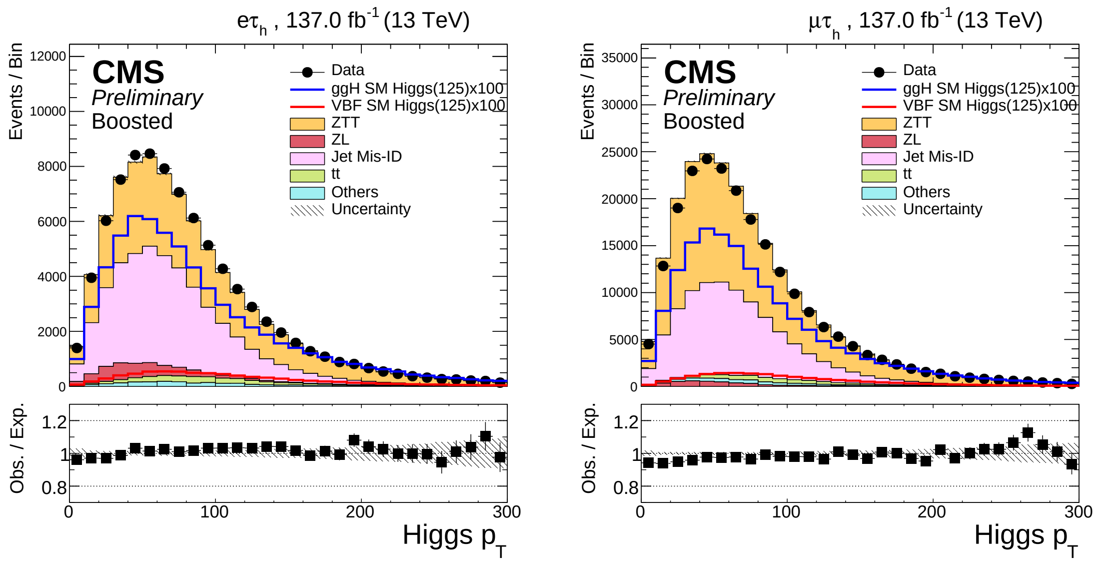

Figure 8.2: *The Higgs' transverse momentum for the boosted category in $\tau_e\tau_h$ (left) and $\tau_\mu\tau_h$ (right).*

Chapter 9

Background Estimation

9.1 $Z \to \tau\bar{\tau}$ Background

As stated in Sec. 7.1, the largest background contribution comes from the irreducible Drell-Yan production of two tau leptons making it crucial to properly model the $Z \to \tau\bar{\tau}$ process. The Drell-Yan production can be simulated fairly well, but difficulties arise as the number of additional jets increases. Because the correlation between two jets is required to access the Higgs coupling, $Z \to \tau\bar{\tau}$ events must be produced with at least two additional jets to populate the sensitive region of the analysis. The mismodeling introduced by including additional jets can be corrected by calculating correction factors, but this introduces additional systematic uncertainties which must be addressed. In addition to requiring excellent modeling, the $Z \to \tau\bar{\tau}$ dataset must have sufficiently high statistics to populate all categories without introducing large statistical uncertainties. Because $Z \to \tau\bar{\tau}$ provides the largest background contribution, a large statistical uncertainty on the $Z \to \tau\bar{\tau}$ prediction results in a large degradation in sensitivity.

The best way to handle both problems at once is to utilize a data-driven background estimation method. Data-driven techniques utilize genuine events collected during data taking to predict background contributions. This provides two excellent advantages: perfect background modeling and high statistics. Because the events are coming directly from data, no additional corrections are required which eliminates the necessity of adding new systematic uncertainties to the analysis. The other benefit relates to the fact that producing events using Monte Carlo simulation is a very time and CPU-intensive process. Data-driven background estimation provides a high-statistics background estimate (roughly the size of the collected dataset after some loose selection) without the need to do any time and resource expensive simulation. As a result, data-driven estimates typically provide much higher statistics than can be reasonably simulated.

The embedding technique[13] is designed to produce a data-driven estimate of the $Z \to \tau\bar{\tau}$ background using $Z \to \mu\bar{\mu}$ events collected by the CMS detector. The best way to explain the embedding technique is to explain the basic concept in steps and then expanding on each step in more detail. The embedding process, shown in Fig. 9.1, takes place in four main steps:

1. In a dedicated control region, $Z \to \mu\bar{\mu}$ events are selected in data.

2. Calorimeter deposits and tracks produced by the dimuon pair are removed.

3. The muon Lorentz vectors are used to simulate a ditau system with identical kinematics.

4. PYTHIA is used to model the decay of the tau leptons in the same way as a typical $Z \to \tau\bar{\tau}$ decay.

As can be seen in the previous description, the embedding technique is actually a hybrid approach where the tau leptons are simulated, but the rest of the event comes directly from data. This means that the description of jets, pileup, etc. is still coming directly from data and requires no corrections or additional systematic uncertainties. The $Z \to \tau\bar{\tau}$ decay is well understood and can be modeled very well. As a result, the embedding technique still has the advantage of much better modeling than Monte Carlo simulation. The embedding technique also retains the advantage of higher statistics due to the fact that only the tau decay must be simulated rather than the entire event. The size of the resulting embedded datasets is still much larger than could be reasonably generated from pure Monte Carlo simulation.

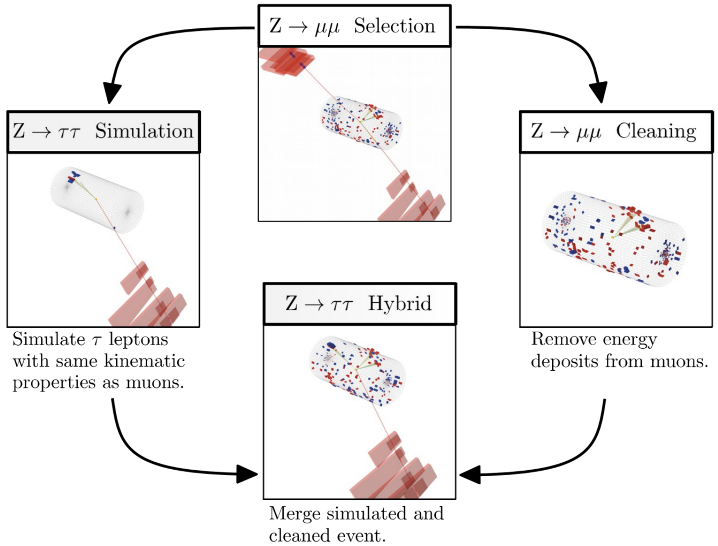

Figure 9.1: *The embedding procedure for producing a data-driven estimate of $Z \to \tau\bar{\tau}$ using $Z \to \mu\bar{\mu}$ events*[13].

The embedding procedure starts with the selection of genuine $Z \to \mu\bar{\mu}$ events in data. The selection must be as loose as possible because the accessible region of phase space will be determined by the kinematics of the selected events. First, events are required to fire at least one dimuon trigger. These triggers require the presence of two muons satisfying an extremely loose isolation requirement and very low p_T thresholds. The muons are required to be within the muon system $|\eta < 2.5$ and must be matched to the primary vertex. Additional selection criteria are applied to suppress dimuon pairs clearly not originating from a Z boson decay. The dimuon pair is required to have opposite charges, an invariant mass $m_{\mu\mu} > 20$ GeV, and, in the case of multiple potential pairs, the pair with the mass closest to the Z boson mass is selected. This selection results in about 1.5 million events per 1 fb^{-1} data collected while maintaining $> 97\%$ purity.

Once an event has been selected, all traces of the dimuon pair must be erased from the event record. The muon track from the global fit is used to remove hits in the inner and outer tracker. Any hit in the tracker system associated to the global muon track is simply removed from the record. The muons may also deposit energy while traversing the calorimeters. The global track is again used to identify clusters in the calorimeters which are intercepted by the interpolated track. The energy of the minimally ionizing particle is subtracted from the cluster to account for the presence of other objects in the vicinity of the muon. If the cluster energy drops below the calorimeter's noise threshold, the cluster is removed entirely. Now, the muons may be completely removed from the event record.

The dimuon pair is then used to simulate a ditau pair with the appropriate kinematics. A completely empty event record is created and then filled with only the kinematic information from the dimuon pair. The dimuon system is then transformed into the center-of-mass reference frame while fixing the dimuon invariant mass to the reconstructed value. In this frame, the lepton energy and momentum are given by

$$E^*_\ell = \frac{m_{\mu\mu}}{2}\ ; \qquad |\vec{p}^*_\ell| = \sqrt{E^{*2}_\ell - m^2_\ell}\ ; \qquad \ell = e, \mu \tag{9.1}$$

The transformed energy and momentum are then used to seed the simulation of tau leptons. The initial vertex for the simulated tau leptons is set to the primary vertex of the dimuon event. The tau leptons are simulated four times corresponding to four decay channels: $\tau_e\tau_h$, $\tau_\mu\tau_h$, $\tau_h\tau_h$, and $\tau_e\tau_\mu$. The reuse of a single dimuon event is valid provided the analysis of each channel remains orthogonal to every other channel.

The last step of the embedding procedure involves processing the decay of the simulated tau leptons. Because the tau lepton decay involves the production of neutrinos which carry away a fraction of the tau momentum, the visible decay products will be less energetic than the dimuon pair used to seed the taus. It is possible for the visible decay products end up in a region of phase space which cannot feasibly be triggered upon. To save time, a kinematic filter is applied remove events which will never be able to fire the required triggers. The filter is applied to the tau decay products before they enter the time consuming CMS detector simulation. Each decay is repeated 1000 times to increase the probability of passing the kinematic filter. If more than one simulation passes the filter, the most recently simulated event is fed to the detector simulation and the ratio of simulations passing the filter over 1000 is stored as an additional weight to be applied later.

Evaluated using the 2017 dataset, this procedure produces a sample of $Z \to \tau\bar{\tau}$ events roughly 14 (15) times larger than observed in the $\tau_e\tau_h$ ($\tau_\mu\tau_h$) channel. This is much larger than could be generated using pure Monte Carlo simulation in a reasonable amount of time and greatly reduces the statistical uncertainty of the analysis. Additionally, the embedded samples provide much better modeling than Drell-Yan Monte Carlo requiring fewer corrections and, as a result, reduces a number of sources of systematic uncertainty. A comparison of the visible ditau mass estimated using $Z \to \tau\bar{\tau}$ events from Monte Carlo versus events produced using the embedding technique is shown in Fig. 9.2.

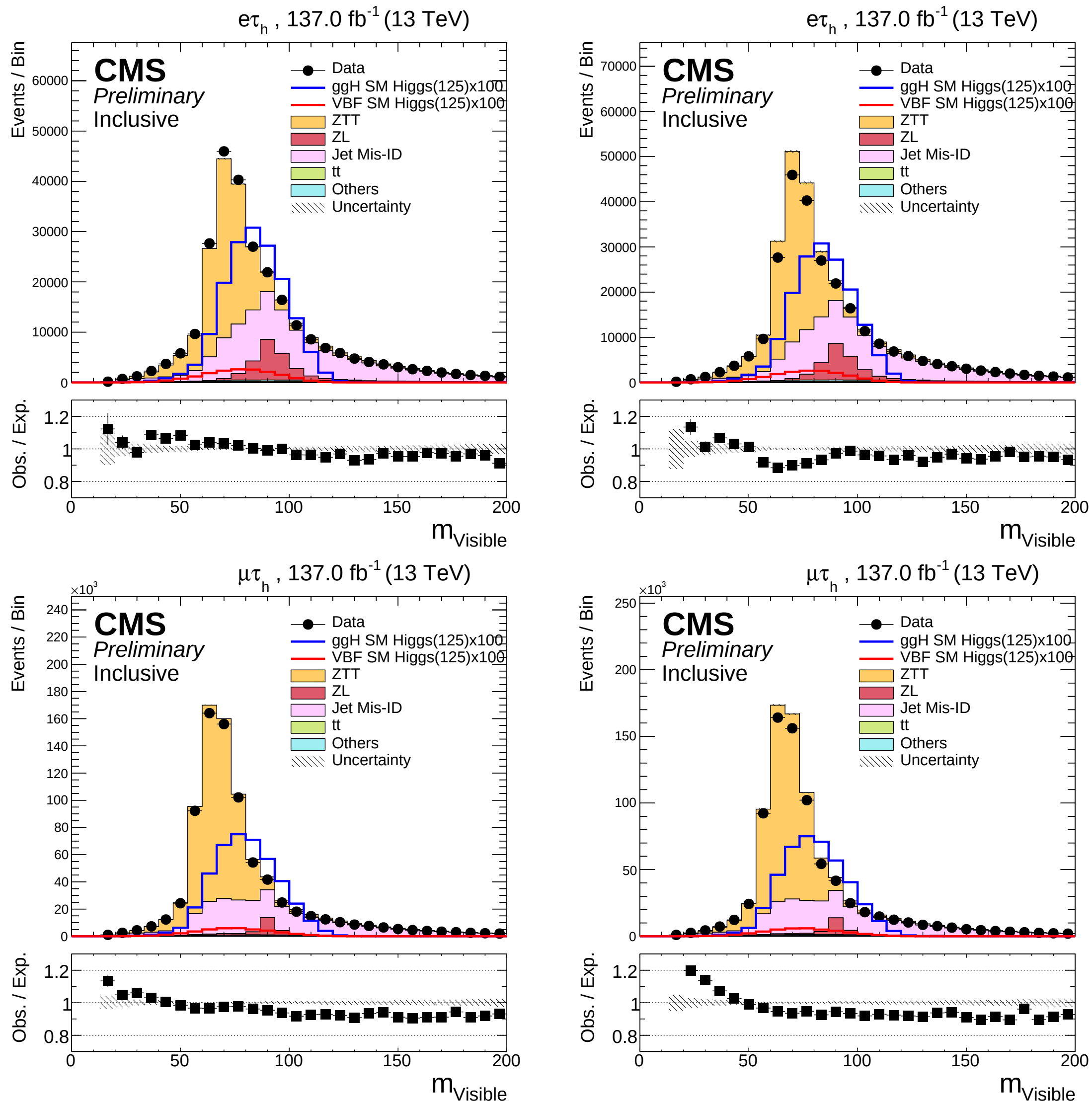

Figure 9.2: *A comparison of embedded (left) versus Monte Carlo (right) estimates in the* $\tau_e\tau_h$ *(top) and* $\tau_\mu\tau_h$ *(bottom) channels. The embedding procedure clearly provides a better description of the data in the region dominated by* $Z \to \tau\bar{\tau}$.

9.2 Jet→ τ_h Fake Background

The second largest background contribution comes from the reducible QCD background where quark or gluon jets are misidentified as hadronically decaying tau leptons. In addition to the QCD production of fake taus, W+jets, $t\bar{t}$, and other smaller processes may produce many jets which can be misidentified as a tau lepton. These processes are jointly referred to as the "jet fakes" background and provide a significant contribution to the total background. Many of the same problems which arise in simulating $Z \to \tau\bar{\tau}$ with additional jets appear again when attempting to simulate the jet fakes background. Modeling processes with many jets in Monte Carlo is difficult and requires many corrections and systematic uncertainties. This is particularly relevant for the QCD processes which are notoriously complicated to model and introduce many difficulties to the analysis. Also, similar to $Z \to \tau\bar{\tau}$, it is very difficult to produce Monte Carlo samples modeling fake tau backgrounds with sufficient statistics. The issue is that the tau identification algorithm has a very small fake rate, meaning it is very unlikely for a jet to be misidentified as a hadronic tau. As a result, extremely large Monte Carlo samples must be generated in order to have a workable number of events with misidentified jets. It is somewhat surprising upon first thought, but, as the algorithm improves, the contribution of jet fakes becomes smaller while the required number of generated events becomes larger.

Following the comparison to $Z \to \tau\bar{\tau}$, the best way to handle the jet fakes background is via a data-driven approach. In this way, we can produce large samples containing fake taus without introducing new corrections or systematic uncertainties. This analysis uses the fake factor method[67] to produce an estimate of the jet fakes background in the region of interest. The general idea behind the fake factor method is that a control region enriched in jets faking tau leptons can be defined by inverting the τ ID selection in the signal region to contain only events failing the ID. These events are still required to pass the loosest working point of the τ ID. The distributions in this control region can then be scaled by the ratio of isolated to non-isolated events (called the "fake factor") to give a reliable modeling of events with a jet faking a tau lepton in the signal region. This method relies on the assumption that the kinematics in the control region and the signal region are similar. Provided this assumption holds, the fake factors simply provide the correct normalization for those shapes in the signal region. In practice, the fake factor method has a few more components all relying on the same general idea and assumption. The extra components are included to increase the reliability of the estimate and account for small, understood differences in shape between signal and control regions.

9.2.1 Fake Factor Procedure

The fake factors are measured separately for each channel and data period and are also measured separately in QCD multijet, $t\bar{t}$, and W+jets events. For each process, a dedicated control region is constructed to be enriched with events from the given process. The fake factors will not be consistent between channels due to the differences in event selection. Generally, the trigger thresholds in the $\tau_e\tau_h$ channel are higher than in the $\tau_\mu\tau_h$ channel leading to harder tau leptons on average. The fake factors are measured separately for each data period because the trigger thresholds increase with each year leading again to harder tau leptons on average. The number of events passing any given τ isolation working point will obviously depend on the process that generated the fake tau. This explains why fake factors are measured separately for each of the main processes contributing to the jet$\rightarrow \tau_h$ fake background.

Because events are going to be categorized based primarily on the number of jets in the event, the fake factors are measured in the bins: zero jets, one jet, two or more jets. It is seen that the fake rates decease by about 10% when the jet multiplicity is increased by one. This is because the probability to find an isolated jet decreases as the event becomes more crowded with jets.

To account for the p_T dependence in the τ ID fake rates, the fake factors are measured as a function of the τp_T. The measured fake factors are then corrected as a function of the electron or muon p_T. Because the triggers split p_T-space into two regions (firing the cross-trigger or firing a single lepton trigger), the corrections are measured separately for these two regions. All three control regions contain slightly different kinematics than the control region due to the cuts used to define a particular region. The fake factors are corrected to account for the difference in kinematics.

To get an estimate of the jet$\rightarrow\tau_h$ background, we start with data events passing all selection criteria for the anti-isolated control region. The event kinematics are used to find the fake factor estimate from each background control region with all relevant corrections applied. The event is then scaled by the weighted average of the three fake factor estimates as follows

$$\mathrm{FF}_{tot} = \sum_{i=1}^{3} n_i \cdot \mathrm{FF}_i \tag{9.2}$$

where FF_i is the fake factor estimate for a given background control region and n_i is the fraction of background i events to the total number of background events. This provides an estimate of the jet$\rightarrow\tau_h$ background from data, but contains contamination from processes with real τ_h's that are not isolated. To account for this, the same procedure is applied to all background processes with real τ_h's and these events are subtracted from data. The result is a data-driven estimate of the jet$\rightarrow\tau_h$ background which is more reliable than could be estimated using Monte Carlo.

9.3 Monte Carlo Backgrounds

The remaining background processes are reasonably small when compared to $Z \rightarrow \tau\bar{\tau}$ and jet fakes. As a result, these processes are all simulated using Monte Carlo. These backgrounds include Drell-Yan processes where the Z boson decays to a di-muon or di-electron pair with one lepton misidentified as a tau lepton, $t\bar{t}$ production, single top production, and diboson production. To remove overlap with the jet fakes background, events with a generator-level quark or gluon jet misidentified as a tau lepton are removed from Monte Carlo samples. Similarly, Monte Carlo events with two genuine tau leptons are discarded to avoid overlap with the embedded samples. All Monte Carlo samples are scaled to their expected cross sections.

Chapter 10

Data Sets

10.1 Data

This analysis uses a combined 139 fb^{-1} of data collected by the CMS experiment during 2016, 2017, and 2018. The SingleMuon dataset is used for the $\tau_\mu\tau_h$ final state while the SingleElectron (2016 and 2017) and EGamma (2018) datasets are used for the $\tau_e\tau_h$ final state.

10.2 Embedded Samples

Embedded samples are used to model backgrounds with a Z boson decaying into a ditau pair in a data-driven manner. The embedding technique is discussed in detail in Chap 9. Separate samples are produced for $\tau_e\tau_h$ and $\tau_\mu\tau_h$ in each era resulting in six total embedded samples.

10.3 Background Monte Carlo

For backgrounds not modeled using a data-driven technique, Monte Carlo simulated samples are used. The PYTHIA[68;69] generator is used for parton showering in all Monte Carlo samples.

The PYTHIA configuration is consistent for 2017 and 2018, but a different configuration is used for 2016. In 2016, PYTHIA version 8.212 is used for parton showering, tune CUETP8M1[70] is used for describing the underlying event, and NNPDF[71;72] 3.0 parton distribution functions are used. In contrast, PYTHIA version 8.230, tune CP5[73], and NNPDF 3.1 are used in 2017 and 2018. All Monte Carlo samples include an estimate of additional pp interactions (pileup) which is reweighted to match the distribution in data. Lastly, GEANT4[74] is used to simulate the CMS detector. All Monte Carlo events are run through this simulation to model detector effects observed in data.

The MADGRAPH[75;76] and POWHEG[77–80] generators are used for modeling background processes. POWHEG is used to model the $t\bar{t}$ and single top backgrounds using versions 2.0 and 1.0, respectively. W+Jets and diboson are both modeled using MADGRAPH with different configurations. W+Jets is produced at leading order (LO) accuracy with MLM jet matching and merging, while diboson is produced at next-to-leading order (NLO) with FxFx jet matching and merging.

10.4 Signal

Anomalous ggH production is modeled using the MADGRAPH generator while VBF and VH production utilize a combination of the JHUGEN[81] and POWHEG generators. Independent samples are produced for each coupling scenario then a procedure has been developed to increase the number of events by combining all scenarios and using the matrix element method to reweight the full sample for each coupling. The scalar $H \to \tau\tau$ decay is modeled using the PYTHIA[68;69] generator. The interference between scalar and pseudoscalar decay was studied and found to have no effect on this analysis.

The MADGRAPH[75] generator is used to produce the Standard Model and anomalous coupling ggH samples at NLO accuracy with up to two additional jets. The samples with different numbers of additional jets are stitched together using appropriate cross sections. A weight is applied in order to match the Higgs p_T spectrum from MADGRAPH to the NNLO prediction. The number of ggH events produced per coupling scenario is roughly tripled by combining all coupling scenarios into a single sample and then using the matrix elements calculated at NLO to produce weights that reshape the merged sample to each coupling scenario.

The POWHEG[80] generator is used to model VBF and VH production at NLO accuracy in regions on phase space less sensitive to anomalous couplings. In the region sensitive to anomalous couplings, POWHEG is used for normalization, but the JHUGEN[2;3;81–83] generator is used to model the shape for different coupling scenarios at LO precision. The number of events per coupling is enhanced using a similar procedure of combining samples then reweighting to different coupling scenarios. The difference with respect to ggH production is that the weights used for VBF and VH reweighting are derived using the matrix elements in the MELA package. The JHUGEN samples are normalized to match the prediction from the POWHEG 2.0 generator. Additionally, the kinematic distributions from JHUGEN were compared to the NLO distributions from POWHEG and were seen to be in good agreement.

Chapter 11

Corrections

11.1 Tau Energy Scale

Commonly differences in τ_h energy scale are observed between Monte Carlo and data. This can occur due to mismodeling of the τ_h and detector effects. Similarly, the energy scale of light leptons faking a τ_h can be mismodeled in simulation leading to a difference between data and Monte Carlo. To correct the modeling in simulation, corrections must be applied directly to the τ_h four-vector. These corrections will vary based on the the τ_h decay mode and whether it is a genuine τ_h or an electron faking a τ_h. The energy scale for muon faking τ_h was found to be negligible.

11.1.1 Genuine Tau Energy Scale

The τ_h energy scale is measured in two regions of phase space based on τ_h p_T using two separate methods. The τ_h energy scale corrections are then applied to genuine τ_h based on decay mode. Because the measured energy scale for both regions is consistent within one standard deviation, only the corrections from the low p_T region are used. Chapter 13 will discuss the treatment of uncertainties from combining the two measurements.

For the low p_T correction, simulated $Z/\gamma^* \to \tau_h\tau_\mu$ are used to reconstruct the τ mass (m_{τ_h}) and the visible mass of the τ and muon (m_{vis}). The energy scale of each τ_h that can be matched to a generator-level τ is varied in steps of 0.2% to construct templates. A maximum likelihood fit is used to extract the most likely τ_h energy scale. The high p_T corrections are measured in largely the same manner using $W^* \to \tau\nu$ events and fitting the m_{τ_h} distribution.

11.1.2 Electron Faking Tau Energy Scale

The $e \to \tau$ energy scale is measured using $Z \to e\tau_h$ events along with the irreducible background $Z \to ee$. The visible mass of the $\tau_e\tau_h$ system is fit allowing the shape of $Z \to ee$ to float. This corresponds to varying the $e \to \tau$ energy scale to find the best fit value. This energy scale is measured separately for the barrel and endcap regions and is binned in τ_h decay mode bins.

11.2 Electron Energy Scale

The energy scale of genuine electrons can also be mismodeled in simulation and must be corrected. The four momentum of all genuine electrons must be scaled and smeared to match the energy scale and resolution measured in data.

11.3 Tau ID Scale Factors

The efficiency of each DeepTau discriminant may vary between data and Monte Carlo and corrections must be derived to bring the efficiencies into agreement. Corrections are derived separately for the DeepTau ID against jets, against electrons, and against muons.

11.3.1 Against Jets ID Scale Factor

The DeepTau against jet ID scale factors are measured using the tag-and-probe method in $Z/\gamma^* \to \tau_h\tau_\mu$ events. The isolated muon coming from the τ_μ decay is used as a tag and the τ_h is used as the probe. A control region enriched in $Z \to \mu\bar{\mu}$ events is used to constrain the Drell-Yan contribution. The ID scale factor for the embedded samples is derived in the exact same way, but substituting the $\mu \to \tau$ embedded sample for Drell Yan Monte Carlo. A maximum likelihood fit is used to extract the data to Monte Carlo corrections in τ_h p_T and decay mode bins.

11.4 Against Electron ID Scale Factor

To measure the DeepTau against electron discriminator efficiency, the tag-and-probe method is utilized in the SingleElectron dataset and all relevant Monte Carlo samples. A well-identified electron is used as the tag while a loosely identified τ is used as the probe. Events are split into two categories, passing and failing, based on whether the τ passes the discriminant. The fake rate is then defined as the number of $Z \to ee$ events in the pass region over the total number of $Z \to ee$ events (Eq. 11.1)

$$FR = \frac{N^{pass}_{Z\to ee}}{N^{pass}_{Z\to ee} + N^{fail}_{Z\to ee}} \tag{11.1}$$

A maximum likelihood fit is then performed simultaneously on the pass and fail regions. The ratio between prefit and postfit fake rates is used as the DeepTau against electron discriminator scale factor. The scale factor is determined in different decay mode bins for the barrel and endcap regions separately.

11.5 Against Muon ID Scale Factor

The against muon discriminator scale factors are derived following the same procedure used for against electron discriminator scale factors. The probe is changed from an electron to a muon and the SingleMuon dataset is used instead of the SingleElectron datasets. The scale factor is determined in decay mode and η_τ bins.

11.6 Recoil Corrections

Recoil corrections are applied to correct the p_T^{miss} spectrum in Drell-Yan, W+Jets, and Higgs production where neutrinos are produced in the decay of the boson. The vectorial difference between the measured p_T^{miss} and the total p_T of neutrinos produced in the decay is defined as $\vec{U}$. To correct the p_T^{miss} spectrum, $Z \rightarrow \mu\bar{\mu}$ events are used because the recoil does not contain any neutrinos and the Z boson four vector can be measured precisely. $\vec{U}$ is projected onto the axes parallel (U_1) and perpendicular (U_2) to the Z boson p_T and then U_1 and U_2 are fit separately. The fits are conducted in bins of Z p_T and jet multiplicity. The mean and resolution are taken from the fits and used to correct $\vec{U}$, and indirectly p_T^{miss}, in Drell-Yan, W+Jets, and Higgs production events.

11.7 Pileup Reweighting

Simulated events must be reweighted in order to reproduce the pileup conditions observed in data. To do this, the number of pileup events is measured in data using a minimum bias sample. The pileup distribution in Monte Carlo is then reweighted to reproduce the distribution from the minimum bias sample.

11.8 Prefiring Weights

During 2016 and 2017 data taking, an issue was discovered related to the prefiring of the L1 trigger. The effect is simulated in Monte Carlo and residual effects are addressed using an event-dependent correction. The correction is about 95% in topologies with very forward jets, like VBF production, and very close to unity for events without forward jets.

11.9 Muon ID/Iso/Trigger Efficiency

Similar to the DeepTau ID efficiency, the muon ID, isolation, and trigger efficiencies can differ between data and Monte Carlo. The total correction for these efficiencies is factored as

$$\epsilon^{\mu}_{ID|TRK} \cdot \epsilon^{\mu}_{Iso|ID} \cdot \epsilon^{\mu}_{Trigger|Iso} \tag{11.2}$$

where each term is computed using the tag and probe method. The subscripts show that each subsequent term uses the numerator of the previous term as the denominator of the current term. For example, the second term uses events passing the muon ID as the denominator then events passing muon ID and muon isolation as the numerator. This allows a single efficiency correction to be derived that accounts for all sources of disagreement. This must be done separately for the single triggers and for the muon leg of the cross triggers.

11.10 Electron ID/Iso/Trigger Efficiency

The electron ID, isolation, and trigger efficiencies vary in the same way as muon efficiencies and the corrections are derived in largely the same manner using the tag and probe method.

11.11 Tau Trigger Efficiency

Corrections are also required for the tau leg of the cross triggers. These corrections are only applied to events which fire the cross trigger and not to events which fire one of the single triggers. The corrections are derived largely in the same manner as the muon and electron legs.

11.12 B Tagging Efficiency

Because this analysis vetoes events based on the presence of b-tagged jets, it is necessary to correct for differences in b-tagging efficiency between data and Monte Carlo. To correct the b-tagging efficiency, Monte Carlo events are reweighted to reproduce the DeepCSV discriminant distribution in data. This requires a weight for every jet within an event as a function of jet p_T , η, and flavor. The overall event weight is then the product of weights for all jets in the event.

11.13 Higgs p_T Reweighting

In order to achieve a better description of the Higgs p_T spectrum, we reweight ggH events produced with MadGraph (NLO) to the NNLO prediction[84–86]. The weights depend on the generated Higgs p_T , the number of jets with $p_T > 30$ GeV, and the p_T of the lead jet.

11.14 Z p_T Reweighting

The Drell-Yan Monte Carlo samples are generated by MadGraph at LO. This means that the generator-level p_T and $m_{\ell\ell}$ distributions need to be corrected to match what is observed in data. The weights are derived to bring agreement between data and Monte Carlo in a pure $Z \to \mu\bar{\mu}$ control region. The weights change the shape of the p_T and $m_{\ell\ell}$ distributions, but are normalized to avoid changing the yield. Because Drell-Yan samples generated in 2016 use a different tune than those generated in 2017 and 2018, weights are calculated separately for 2016 and 2017+2018 data periods.

11.15 Top p_T Reweighting

Similar to the Higgs p_T spectrum, we want to correct the top quark p_T spectrum in $t\bar{t}$ from NLO to NNLO prediction. The corrections are derived as a function of top quark p_T. The total weight is the square root of the product of the corrections for the individual top quarks. $t\bar{t}$ simulations also use different tunes in 2016 (CUETP8M2T4) versus 2017+2018 (CP5) and must also have separate corrections. Because the CP5 tune is used in 2017 and 2018, the weights are first derived for this tune. To apply these weights to 2016 samples, weights are measured to reweight the top p_T spectrum in CUETP8M2T4 to that of CP5. Then, the CP5 weights can be applied directly to the 2016 $t\bar{t}$ samples.

11.16 Generator Weights and Luminosity

Monte Carlo generators provide weights on an event-by-event basis used to scale the contribution of that event. In MadGraph generated samples, these event weights can even be negative effectively reducing the statistics of the sample. The generator weights are applied per event and then each sample is scaled by it's cross section and the luminosity to get the effective yield (Eq. 11.3).

$$yield = w_{gen} \cdot \frac{\sigma \cdot \mathcal{L}}{N_{gen}} \tag{11.3}$$

To account for negative weights from MadGraph samples, the number of generated events is scaled by the sum of the generator weights to get the effective number of generated events.

Chapter 12

Observables

12.1 Ditau Mass

The CMS detector can not provide the information necessary to fully reconstruct the ditau mass ($m_{\tau\tau}$) due to the presence of neutrinos in the decay. While each tau lepton will decay to at least one neutrino, the detector can only provide the transverse momentum of the vectorial sum of all neutrinos. This vectorial sum will also include any other particles that evade detection for any reason. Dedicated algorithms have been designed to reconstruct the most likely $m_{\tau\tau}$ accounting for the incomplete and noisy neutrino information. This analysis uses a simplified version of the SVFit algorithm[87] called FastMTT.

In order to reconstruct $m_{\tau\tau}$, we must first derive a parameterization for the ditau system. For a single tau decay, we can combine the information from all visible decay products into a single four-momentum ($E_{vis}, \vec{p_{vis}}$). Then, to account for the neutrinos, we include the fraction of the tau energy carried by visible decay products ($x = \frac{E_{vis}}{E_{tot}}$) and a description of the neutrino system. The neutrino system can be described using the difference between the tau four momentum and the visible four momentum by defining two angles: the Gottfried-Jackson angle, θ_{GJ}, defined as the angle between the tau and the visible four momentum, and the azimuthal angle from a cone centered on the visible momentum to the tau, denoted ϕ. In addition to these angles, the invariant mass of the neutrino system ($m_{\nu\nu}$) is required to fully describe the neutrino system. The tau decay is now fully parameterized in terms of $(E_{vis}, \vec{p_{vis}})$, x, and the three parameter neutrino system. Returning to the case of two taus decaying, it is easy to see there are six unknown parameters, $\vec{a} = (x_1,\ \phi_1,\ m_{\nu\nu,1},\ x_2,\ \phi_2,\ m_{\nu\nu,2})$ and five measured parameters, $\vec{y} = (E_{vis,1},\ \vec{p_{vis,2}},\ E_{vis,1},\ \vec{p_{vis,2}},\ \vec{E}_T^{missreco})$

The SVFit algorithm determines the most likely $m_{\tau\tau}$ by maximizing the likelihood given in Eq. 12.1

$$\mathcal{L}(m_{test}|event\ data) = \int p(m_{\tau\tau}|\vec{y}, \vec{a})\delta(m_{\tau\tau} - m_{test})d\vec{a} \tag{12.1}$$

where the integral runs over all unknown variables for a given mass hypothesis m_{test}. In practice, the probability $p(m_{\tau\tau}|\vec{y}, \vec{a})$ is written as a product of three independent terms (Eq. 12.2): the matrix element for each tau decay (ME), the transfer function (TF) discussed later, and a regularization term (REG) of the form $m_{\tau\tau}^{\kappa}$ with $\kappa \sim 5$. The transfer function is defined in Eq. 12.3

$$p(m_{\tau\tau}|\vec{y}, \vec{a}) = ME \cdot TF \cdot REG \tag{12.2}$$

$$\begin{aligned} TF_{MET} &= \mathcal{L}(\vec{E}_T^{miss\ reco}|\vec{E}_T^{miss\ hypo}) \\ &= \frac{1}{2\pi\sqrt{|V|}} \exp\left[-\frac{1}{2}\left((\vec{E}_T^{miss\ reco} - \vec{E}_T^{miss\ hypo})^T V^{-1} (\vec{E}_T^{miss\ reco} - \vec{E}_T^{miss\ hypo})\right)\right] \end{aligned} \tag{12.3}$$

where $\vec{E}_T^{miss\ hypo}$ is constructed for each tau from the triplet of unknown parameters. This function is designed to give the likelihood of the measured parameters given a hypothesis for $\vec{a}$.

SVFit performs a brute-force search evaluating the integral from Eq. 12.1 for each point in $(\vec{y},\ \vec{a})$ space and returning the most likely m_{test} as an estimate of $m_{\tau\tau}$.

The SVFit algorithm is very costly in terms of time and memory, especially once we begin evaluating systematic uncertainties which require the calculation to be performed a number of times per event. For this reason, the FastMTT algorithm was designed to use SVFit as a starting point and attempt to simplify the calculation of Eq. 12.1 while maintaining similar performance.

The first difference between the algorithms comes from the observation that the ME term in the integrand has very small impact compared to the transfer function and the regularization terms. In FastMTT, the ME term is set to 1 leading to a much simpler integrand. Second, for taus with a sufficient boost, the Gottfried-Jackson angle becomes very small allowing us to assume the tau direction and neutrino direction are the same, called the collinear approximation. In the collinear approximation, we define $\theta_{GJ} = 0$ and we neglect ϕ because it is no longer well defined. These observations allow us to simplify Eq. 12.1 to Eq. 12.4.

$$\mathcal{L}(m_{test}|event\ data) = TF \cdot \int \delta(m_{\tau\tau} - m_{test}) d\vec{a} \tag{12.4}$$

The only remaining unknowns in $\vec{a}$ are the energy fractions x_i which are estimated using a brute-force search in $(x_1,\ x_2)$ space to find the pairing the maximizes Eq. 12.4. The regularization term is absorbed into m_{test} and is tuned by hand to give performance similar to SVFit. These simplifications lead to an estimate of $m_{\tau\tau}$ which is similar in performance to SVFit while running ~100 times faster.

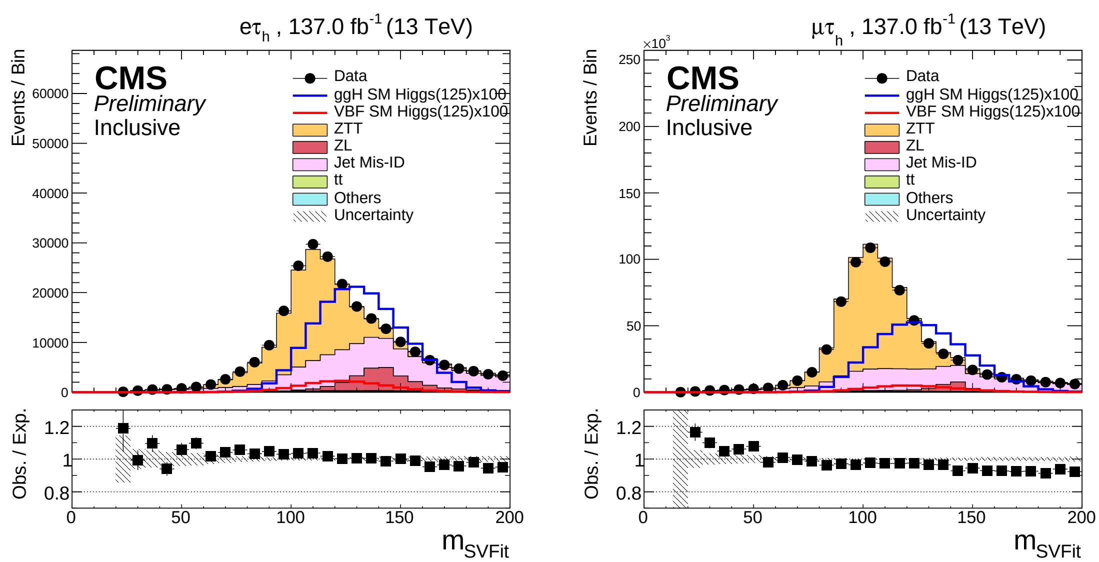

Figure 12.1: *The ditau mass reconstructed using the FastMTT algorithm in the $\tau_e\tau_h$ (left) and $\tau_\mu\tau_h$ (right) channel.*

12.2 Matrix Element Likelihood Approach (MELA)

As discussed in Chapter 3, the nature of the Higgs coupling produces a measurable effect on the other particles involved in the interaction. In the case of Higgs production, this means the coupling scenarios alter the correlations between final state jets. As a result, a good description of the Higgs + 2 jet system is crucial. Fig. 12.2 and Fig. 12.3 shows it is possible to fully describe the kinematics of the Higgs + 2 jet system in the dijet rest frame using 5 parameters (3 angles and 2 momenta)[2;3]. In order to reduce these five parameters to the minimal number of observables without losing any information, the matrix element likelihood approach (MELA)[2;3;17;28;82;83] is utilized.

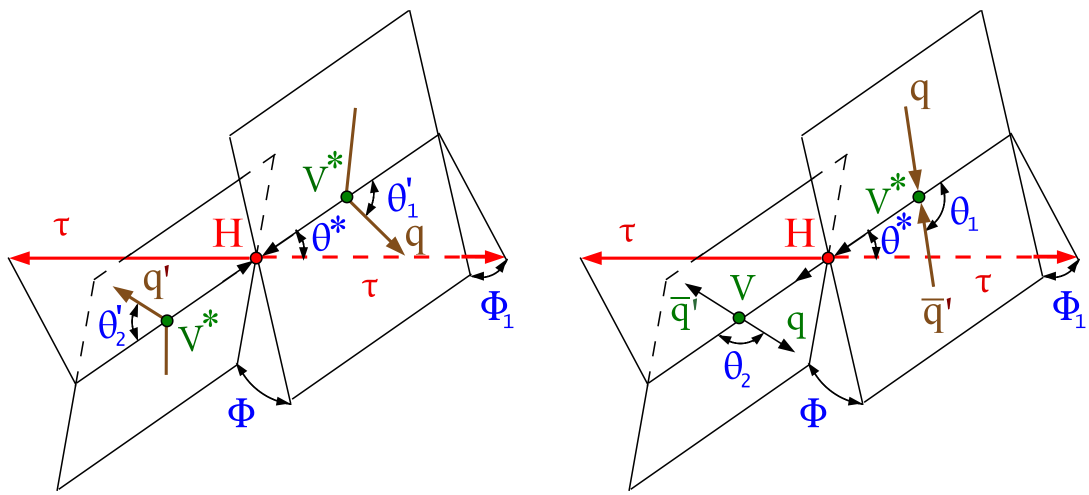

Figure 12.2: *Diagram of Higgs production in vector boson fusion (left) and associated production (right). The five MELA parameters are shown on each diagram along with θ^* which relates the dijet system to the tau decay plane*[2;3].

Given the set of parameters fully describing the system, MELA calculates the probability of the event given different LO matrix elements. This allows us to calculate the probability of any process for which we can fully define a matrix element. The probabilities can then be combined to create MELA discriminants designed to separate different classes of events. This is particularly useful for distinguishing $H \to \tau\bar{\tau}$ events produced under different coupling hypotheses. In this way, we are able to simplify the analysis by reducing the dimensionality of our observable space.

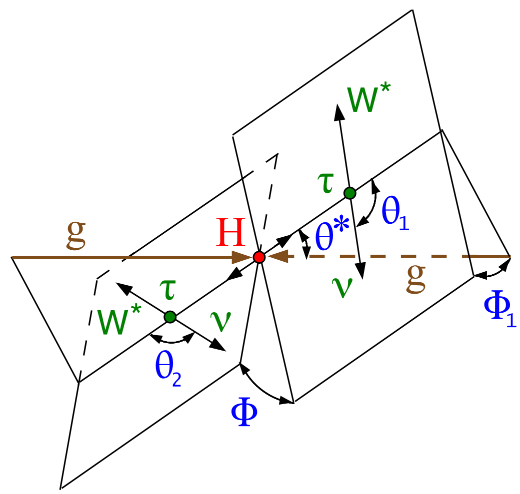

Figure 12.3: *Diagram of Higgs production via gluon-gluon fusion. The five MELA parameters are shown on each diagram along with θ^* which relates the dijet system to the tau decay plane*[2;3].

12.3 MELA Discriminants

It is possible to construct three broad categories of MELA discriminants by taking different ratios of MELA probabilities. By definition, each discriminant is conveniently bound from 0 to 1 and provides the optimal separation between processes.

The first category of discriminants is constructed to separate signal and background processes:

$$\mathcal{D}_{bkg} = \frac{\mathcal{P}_{SM}}{\mathcal{P}_{SM} + \mathcal{P}_{bkg}} \tag{12.5}$$

where $\mathcal{P}_{SM}$ is the probability of the signal process and $\mathcal{P}_{bkg}$ is the probability of a given background. Because it is generally quite difficult to write a matrix element describing the entire background composition, we do not rely on $\mathcal{D}_{bkg}$ in this analysis. Instead, we utilize other tools for distinguishing signal versus background.

It is also possible to construct discriminants that separate different signal hypotheses:

$$\mathcal{D}_{BSM} = \frac{\mathcal{P}_{SM}}{\mathcal{P}_{SM} + \mathcal{P}_{BSM}} \tag{12.6}$$

In this discriminant, $\mathcal{P}_{SM}$ is the probability of the signal process under the Standard Model hypothesis while $\mathcal{P}_{BSM}$ is the probability of the signal process under a beyond the Standard Model hypothesis. This analysis makes extensive use of this type of discriminant for separating signal processes produced with different couplings.

The last type of discriminant that can be constructed is designed to isolate the interference contribution:

$$\mathcal{D}_{int} = \frac{\mathcal{P}^{int}_{SM-BSM}}{\mathcal{P}_{SM} + \mathcal{P}_{BSM}} \tag{12.7}$$

The new probability here, $\mathcal{P}^{int}_{SM-BSM}$, is the interference part of the probability distribution containing a mixture of SM and BSM contributions.

12.4 HVV and Hgg Discriminants

The ggH analysis defines a discriminant to separate Standard Model Higgs coupling from the pure pseudoscalar coupling hypothesis, $\mathcal{D}^{\mathrm{ggH}}_{0-}$, and a pure CP-odd discriminant sensitive to the interference between couplings, $\mathcal{D}^{\mathrm{ggH}}_{\mathrm{CP}}$. These discriminants are defined in Eq. 12.8 and Eq. 12.9 and shown in Fig. 12.4.

$$\mathcal{D}^{\mathrm{ggH}}_{0-} = \frac{\mathcal{P}^{\mathrm{ggH}}_{\mathrm{SM}}}{\mathcal{P}^{\mathrm{ggH}}_{\mathrm{SM}} + \mathcal{P}^{\mathrm{ggH}}_{\mathrm{PS}}} \tag{12.8}$$

$$\mathcal{D}^{\mathrm{ggH}}_{\mathrm{CP}} = \frac{\mathcal{P}^{\mathrm{ggH}}_{\mathrm{SM-PS}}}{\mathcal{P}^{\mathrm{ggH}}_{\mathrm{SM}} + \mathcal{P}^{\mathrm{ggH}}_{\mathrm{PS}}}. \tag{12.9}$$

The VBF analysis similarly defines discriminants to separate coupling hypotheses. In this case, four discriminants shown in Eq. 12.10 are constructed to target the four coupling parameters defined in Chapter 3. Another discriminant sensitive to interference effects is defined in Eq. 12.11: $\mathcal{D}^{\mathrm{VBF}}_{\mathrm{CP}}$. Because CP effects are only observable in the f_{a3} coupling, $\mathcal{D}^{\mathrm{VBF}}_{\mathrm{CP}}$ is only used in conjunction with $\mathcal{D}^{\mathrm{VBF}}_{0-}$ for measuring the f_{a3} parameter. The discriminants used to measure f_{a3} are shown in Fig. 12.4.

$$\mathcal{D}_{0-}^{\mathrm{VBF}} = \frac{\mathcal{P}_{\mathrm{SM}}^{\mathrm{VBF}}}{\mathcal{P}_{\mathrm{SM}}^{\mathrm{VBF}} + \mathcal{P}_{\mathrm{PS}}^{\mathrm{VBF}}} \qquad \mathcal{D}_{\mathrm{a2}} = \frac{\mathcal{P}_{\mathrm{SM}}^{\mathrm{VBF}}}{\mathcal{P}_{\mathrm{SM}}^{\mathrm{VBF}} + \mathcal{P}_{\mathrm{a2}}}$$
$$\mathcal{D}_{\Lambda 1} = \frac{\mathcal{P}_{\mathrm{SM}}^{\mathrm{VBF}}}{\mathcal{P}_{\mathrm{SM}}^{\mathrm{VBF}} + \mathcal{P}_{\Lambda 1}} \qquad \mathcal{D}_{\Lambda 1}^{Z\gamma} = \frac{\mathcal{P}_{\mathrm{SM}}^{\mathrm{VBF}}}{\mathcal{P}_{\mathrm{SM}}^{\mathrm{VBF}} + \mathcal{P}_{\Lambda 1}^{Z\gamma}} \tag{12.10}$$

$$\mathcal{D}_{\mathrm{CP}}^{\mathrm{VBF}} = \frac{\mathcal{P}_{\mathrm{SM-PS}}^{\mathrm{VBF}}}{\mathcal{P}_{\mathrm{SM}}^{\mathrm{VBF}} + \mathcal{P}_{\mathrm{PS}}^{\mathrm{VBF}}}. \tag{12.11}$$

Both analyses utilize the $\mathcal{D}_{\mathrm{2jet}}^{\mathrm{VBF}}$ discriminant defined in Eq. 12.12 and shown in Fig. 12.5. $\mathcal{D}_{\mathrm{2jet}}^{\mathrm{VBF}}$ is designed to separate ggH production from VBF production with Standard Model couplings. Having a good separation between production mechanisms becomes important in the final fit because the signal strength parameters for each production mechanism are allowed to float.

$$\mathcal{D}_{\mathrm{2jet}}^{\mathrm{VBF}} = \frac{\mathcal{P}_{\mathrm{SM}}^{\mathrm{ggH}} + \mathcal{P}_{\mathrm{PS}}^{\mathrm{ggH}}}{\mathcal{P}_{\mathrm{SM}}^{\mathrm{ggH}} + \mathcal{P}_{\mathrm{PS}}^{\mathrm{ggH}} + \mathcal{P}_{\mathrm{SM}}^{\mathrm{VBF}}} \tag{12.12}$$

12.5 Neural Network

A neural network is used to separate signal process from all background processes. To do this, a fully connected, feed-forward network is trained using the Keras[88] framework for binary classification. Because the kinematics in the $\tau_e\tau_h$ and $\tau_\mu\tau_h$ channel are so similar, a single network can be trained on the combination of channels to increase the training statistics by roughly a factor of two. The change in kinematics is significant enough between different data periods that we choose to have a network per data period instead of combining into a single network.

The network is trained using events where a Higgs boson is produced via vector-boson fusion and then decays to a ditau pair. This process is chosen because HVV is the most sensitive production mode. For the Hgg coupling, the same signal sample is used due to the fact that the most interesting gluon-gluon fusion events are the events with kinematics most similar to vector-boson fusion events. This allows us to train a single network that

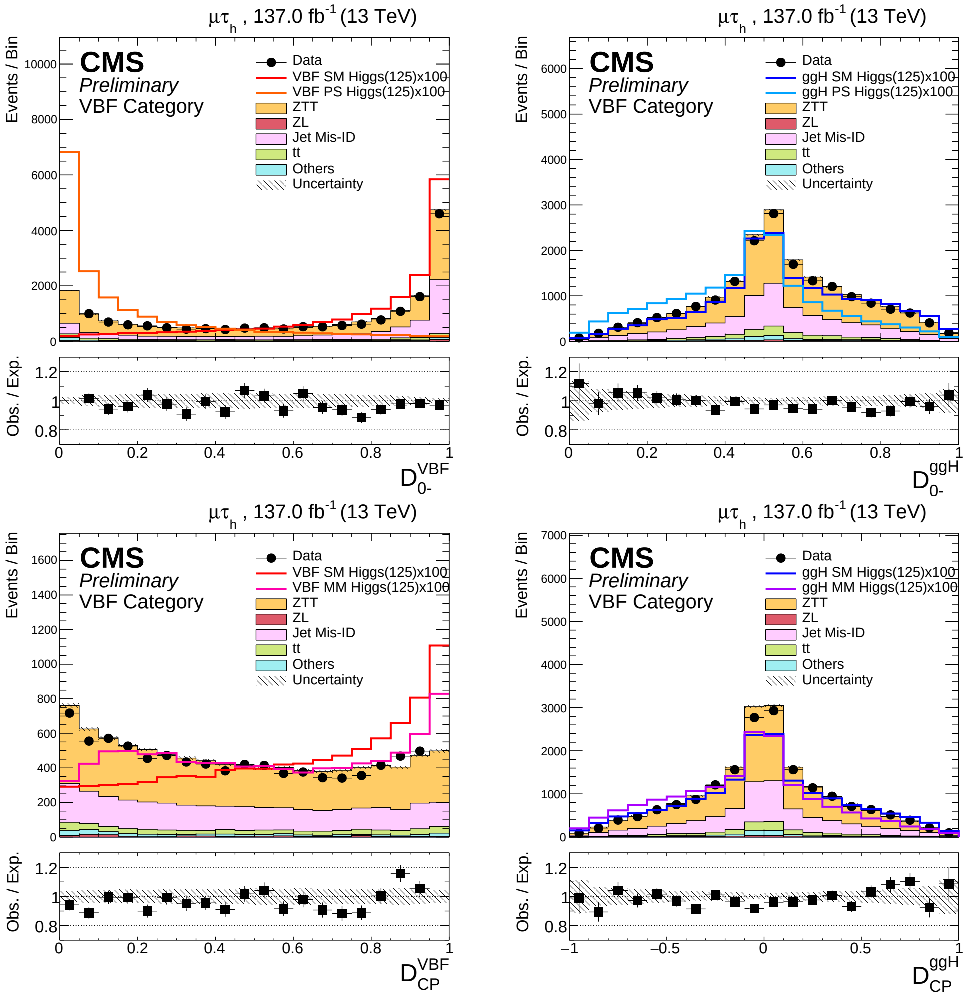

Figure 12.4: *MELA discriminants targeting the f_{a3} parameter in the $\tau_\mu\tau_h$ channel. The top row shows the $\mathcal{D}_{0-}$ discriminants designed to separate the pure scalar (SM) and pure pseudoscalar (PS) couplings. The $\mathcal{D}_{CP}$ discriminants are shown on the bottom row where the pure scalar (SM) coupling is separated from a mixed state (MM) with interference between CP-even and CP-odd states.*

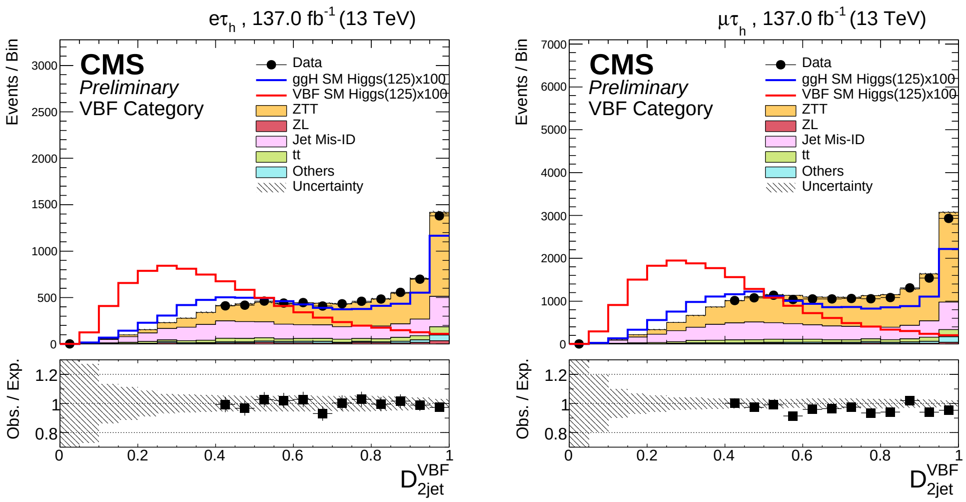

Figure 12.5: $\mathcal{D}_{\text{2jet}}^{\text{VBF}}$ *for the* $\tau_e\tau_h$ *(left) and* $\tau_\mu\tau_h$ *(right) channel. Here, the VBF production (red) is separated from ggH production (blue).*

can be used for both analyses. Events where a Z boson decays to a ditau pair are used as a background for training the network. The network is seen to do a good job rejecting other backgrounds without explicitly including them in the training. Therefore, we keep the network as simple as possible by only using $Z \to \tau\bar{\tau}$ events as the background during training.

As input variables to the network, we provide the ditau mass ($m_{\tau\tau}$), the dijet mass (m_{JJ}), the visible Higgs pT (p_T^H), and the seven MELA input variables which are all shown in Fig. 12.6, Fig. 12.7, and Fig. 12.8. The MELA input variables give us a complete description of the system in the dijet rest frame. In order to account for the boost of the entire system, we include m_{JJ} and p_T^H. Lastly, $m_{\tau\tau}$ is included to separate Higgs to ditau events from Z to ditau events. These events have very similar kinematics and may only be distinguished by $m_{\tau\tau}$. All input variables are normalized to mean-zero variance-one. Events are properly weighted with respect to other events in the same sample and then an additional weight is applied to account for the different statistics between the two samples.

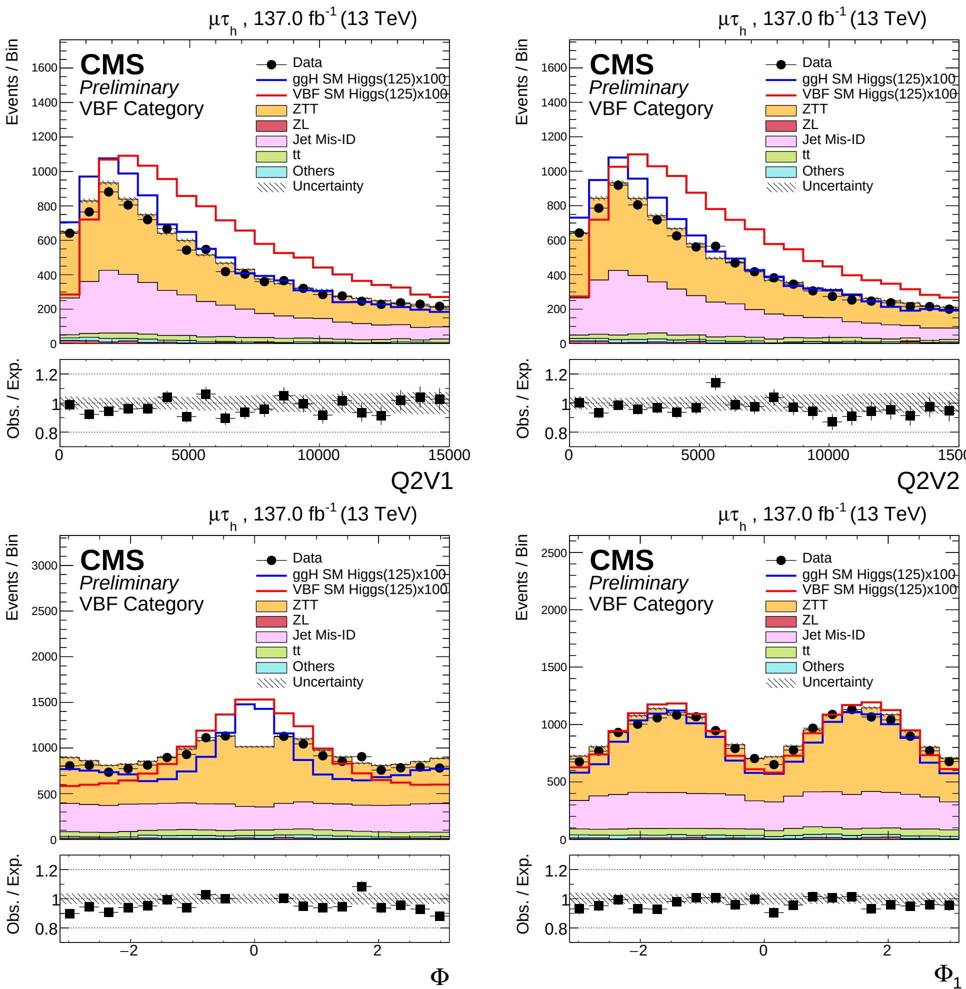

Figure 12.6: *MELA input variables in the $\tau_\mu\tau_h$ channel used for training the network.*

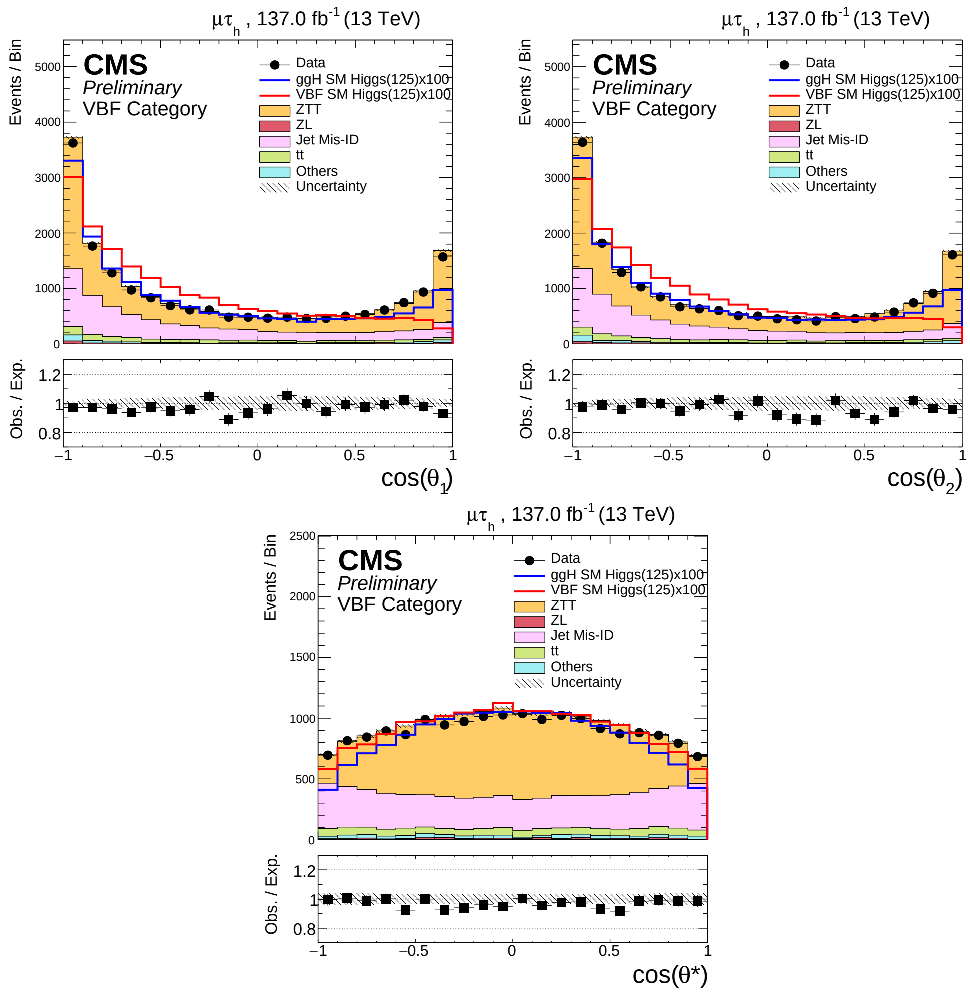

Figure 12.7: *Remaining MELA input variables in the $\tau_\mu\tau_h$ channel used for training the network.*

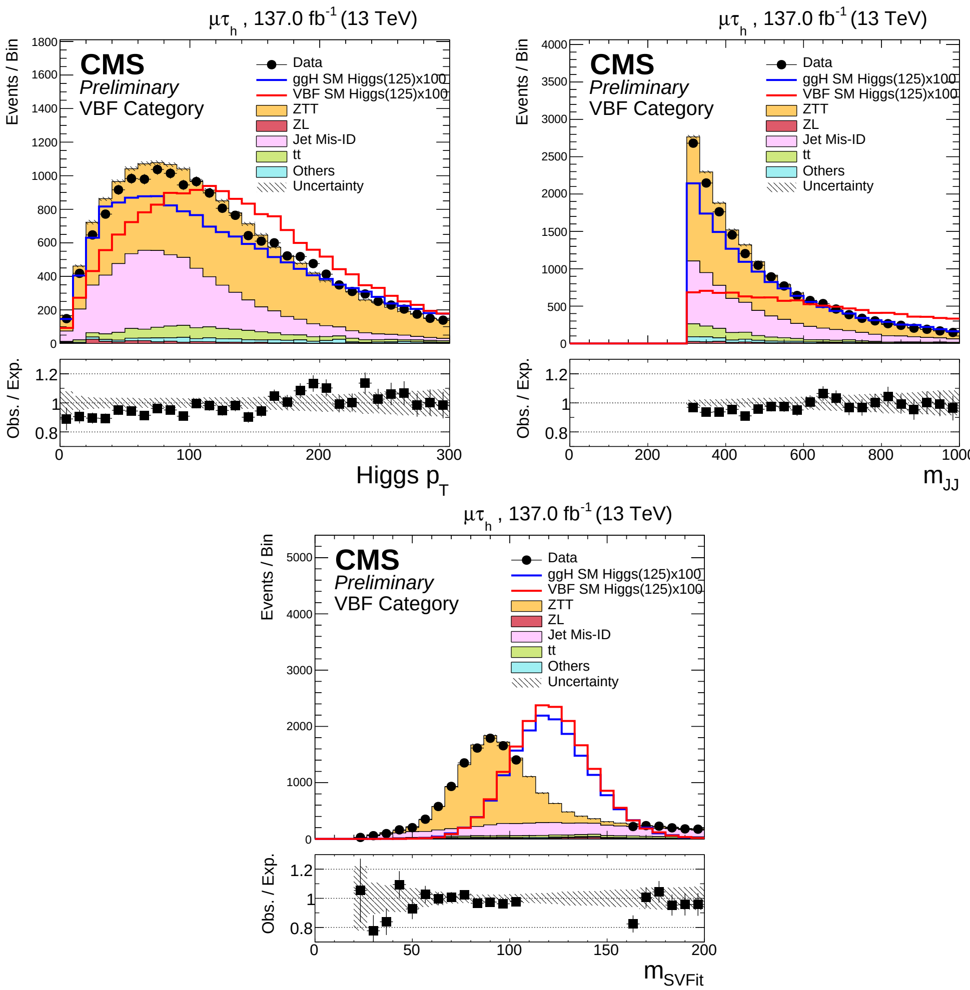

Figure 12.8: *Kinematic variables provided in addition to the MELA input variables for network training.*

The network architecture consists of two hidden layers. The first containing a number of nodes equal to twice the number of input variables (20). The second layer contains a number of nodes equal to the number of input variables (10). These choices are made to keep the network as simple as possible while still providing high separation power. After optimization studies, the ReLU activation, Eq. 12.13, function was seen to provide the best performance when used on the hidden layers.

$$f(x) = \max(0, x) \tag{12.13}$$

The sigmoid function, Eq. 12.14, is used in conjunction with the binary cross-entropy loss function in the output layer. The similarity between the cross-entropy and the definition of entropy from statistical mechanics can be seen in Eq. 12.15, where p_i refers to the probability of the true class while q_i is the probability of the predicted class. Binary cross-entropy is a special case of the cross-entropy used for binary classification where the probabilities of true classes (y) and predicted classes ($\hat{y}$) are constrained to $p_i \in \{y, 1-y\}$ and $q_i \in \{\hat{y}, 1-\hat{y}\}$. The activation functions are shown in Fig. 12.9.

$$f(x) = \frac{1}{1+e^{-x}} \tag{12.14}$$

$$H(p,q) = -\sum_i p_i \log q_i = -y \log \hat{y} - (1-y)\log(1-\hat{y}) \tag{12.15}$$

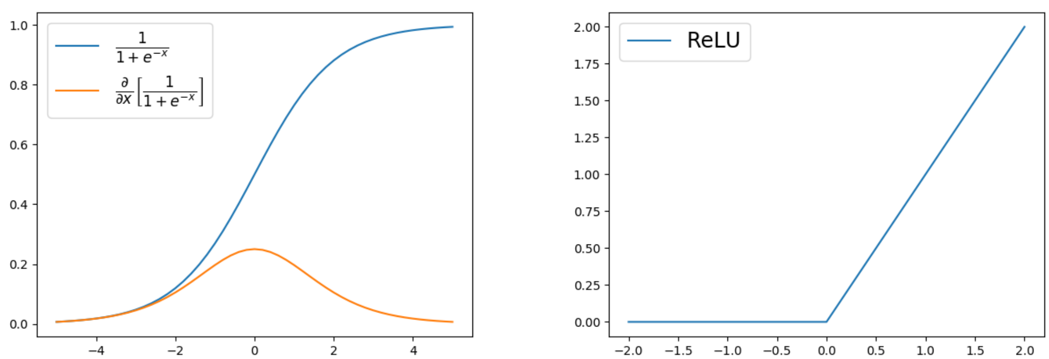

Figure 12.9: *The sigmoid (left) and ReLU (right) activation functions. The sigmoid is shown along with its derivative which is used during backpropogation.*

The loss function is monitored for overtraining and the training process is concluded when the validation loss has converged for fifty epochs. This monitoring is shown in Fig. 12.10. The resulting $\mathcal{D}_{NN}$ distributions are shown in Fig. 12.11.

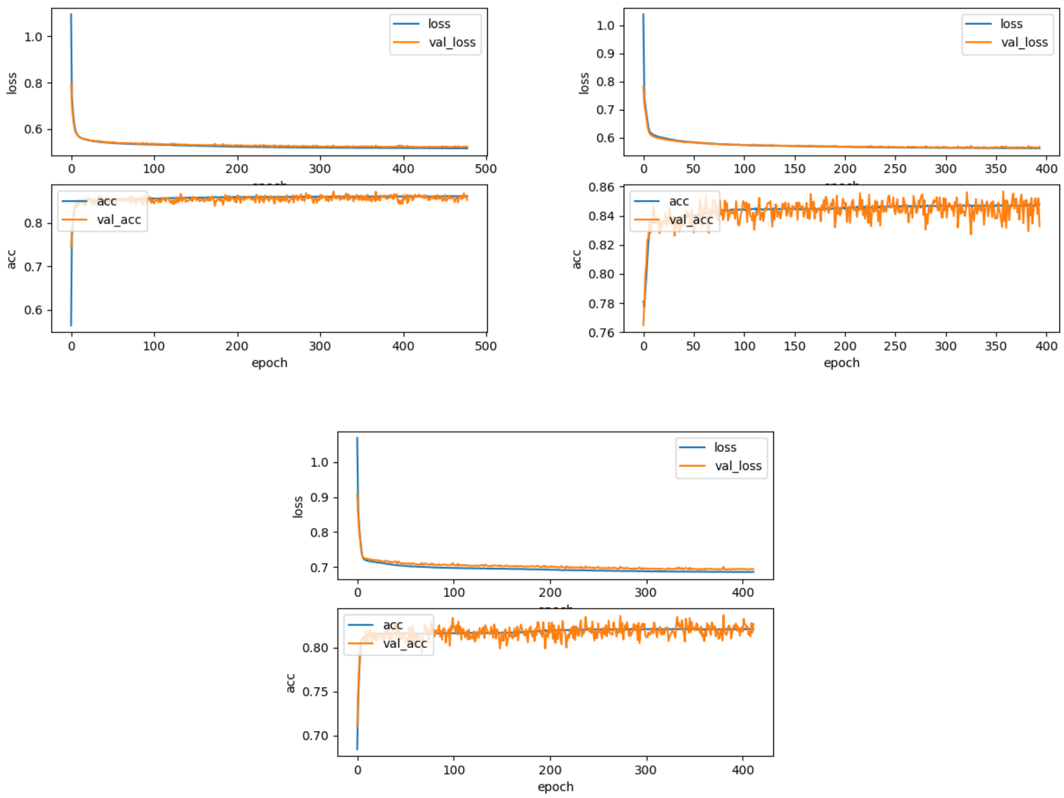

Figure 12.10: *Training and validation loss for 2016 (left), 2017 (right), and 2018 (bottom). In all cases, the training and validation loss converge to a similar value. A divergence between the losses where the training loss continues to decrease while the validation loss does not would indicate overtraining of the network.*

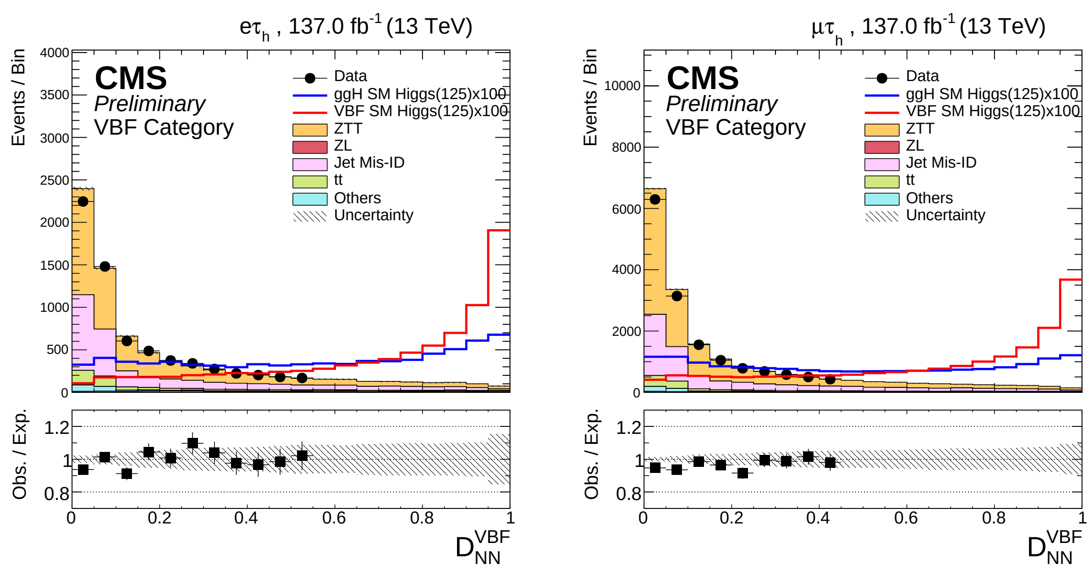

Figure 12.11: *$\mathcal{D}_{NN}$ distributions in the $\tau_e\tau_h$ (left) and $\tau_\mu\tau_h$ (right) channels. The network is trained to only separate VBF and ZTT processes, but is observed to separate all background processes from signal processes.*

Chapter 13

Systematics

The following section describes all systematics uncertainties considered in the analysis and includes a summary in table 13.1. The table includes the correlation between simulated processes and the predictions of the embedded samples. In the cases where the correlation is nonzero, the uncertainty is applied separately to the embedded sample to create an "embedded-only" uncertainty. The correlation is then handled by scaling the MC component by unity, the correlated embedded component by ρ, and the "embedded-only" component by $\sqrt{1-\rho^2}$.

13.1 τ_h energy scale

A decay mode based correction is applied to all real τ_h s to correct the measured τ_h energy scale. This effects the shape of many distributions and is therefore treated as a shape uncertainty. The corrections and corresponding uncertainties are different between Monte Carlo and embedded samples. The uncertainties are uncorrelated between decay modes and between data periods.

The Monte Carlo corrections are measured separately for the low p_T region using $Z \to \tau\bar{\tau}$ events and the high p_T region using $W^* \to \tau\nu_\tau$ events. While the measured correction is consistent within one standard deviation for both measurements, the uncertainties have a larger variance. To account for this, the uncertainty on the τ_h energy scale is split by p_T as well as decay mode. The uncertainty for events with $p_T^\tau < 34$ GeV comes directly from the $Z \to \tau\bar{\tau}$ measurement, while the uncertainty for events with $p_T^\tau > 170$ GeV comes directly from $W^* \to \tau\nu_\tau$ events. The uncertainty for events with $34 <= p_T^\tau <= 170$ GeV comes from the linear interpolation between the two measurements.

For the embedded samples, the uncertainties only depend on the τ decay mode. The effect of the τ_h energy scale in embedded events is treated as 50% correlated with the uncertainty from Monte Carlo.

13.2 e $\to \tau_h$ energy scale

The uncertainty on the energy scale of τ_h matched to a generator level electron is binned in decay mode as well as barrel versus endcap. The corresponding uncertainty changes the shape of all distributions with an electron faking a τ_h and thus is treated as a shape uncertainty. The correction is measured separately for Monte Carlo and embedded samples so the uncertainties are treated as 50% correlated.

13.3 $\mu \to \tau_h$ energy scale

A decay mode based correction is also applied to correct the energy scale of τ_h candidates matched to a muon at the generator level. Again, this uncertainty is treated as 50% correlated between Monte Carlo and embedded samples.

13.4 Electron energy scale

An uncertainty is assigned to account for systematic shifts in the measured electron energy. It is also possible to assign an uncertainty to the resolution of the electron energy scale, but this is found to be negligible and is therefore not considered. The electron energy scale is corrected on an event-by-event basis using the recommendation from the EGamma POG and is treated as a shape uncertainty. This uncertainty is 100% correlated between data periods.

13.5 Muon energy scale

An uncertainty is assigned to measurements of the muon energy scale and is binned in muon pseudorapidity then treated as a shape uncertainty. The uncertainty is uncorrelated in pseudorapidity bins, but is 100% correlated between data periods.

13.6 Jet energy scale

Event-by-event jet energy scale corrections are applied to correct the jet energy scale and are propagated to the p_T^{miss}. These corrections contain 27 separate sources of uncertainty which we are able to merge into 11 combined sources based on correlations between individual sources. These combinations follow the recommendation of the JetMET group and are documented in table 13.2

13.6.1 Jet energy resolution

Jet energies in simulation must be smeared in order to accurately model the jet energy resolution in data. A shape uncertainty is assigned to the smearing process which is uncorrelated between data periods.

13.7 p_T^{miss} energy scale

To account for uncertainties introduced by the recoil corrections, six shape systematics are assigned to processes that have recoil corrections applied. The six systematics are split into two groups which each contain three shapes with one shape per jet multiplicity bin. The two groups are split based on whether the shape is the result of uncertainty in the resolution of the correction or the scale.

For processes that don't require recoil corrections, a single shape is used to model uncertainty in the measured p_T^{miss}.

13.8 τ_h ID

Uncertainty in the DeepTau ID's anti-jet scale factors are modeled using a single shape uncertainty split into uncorrelated bins based on the tau decay mode and p_T bin. It is also uncorrelated between different data periods. This uncertainty is only applied to events containing a genuine tau lepton at the generator level.

13.9 τ_h ID against e

A shape uncertainty is assigned to the DeepTau ID's anti-electron discriminant. The uncertainty is split into the barrel and endcap regions and is uncorrelated between pseudorapidity bins and data periods.

13.10 τ_h ID against μ

A shape uncertainty is assigned also to the DeepTau ID's anti-muon discriminant. The uncertainty is split into five, uncorrelated pseudorapidity bins and is uncorrelated between year.

13.11 e ID

A flat 1% systematic is assigned to account for uncertainty in electron tracking, reconstruction, and efficiency. It is uncorrelated in data periods.

13.12 μ ID

Similarly, a flat 1% systematic is assigned to account for uncertainty in muon tracking, reconstruction, and efficiency. It is uncorrelated in data periods.

13.13 Triggers

The uncertainty in trigger efficiency is 2% per light lepton leg and is treated as a shape effect to account for the fact that single triggers and cross triggers are combined to cover the full phase space. In the region where the single trigger fires, there is only the 2% uncertainty. But, in the region of the cross trigger, there is additionally an uncertainty in the tau leg that is p_T-dependent based on a fit to the tau trigger turn ons. The single and cross trigger uncertainties are uncorrelated resulting in the shape effect that is uncorrelated between data periods.

13.14 Other Uncertainties

The prefiring corrections are assigned a single shape uncertainty that is correlated between 2016 and 2017 and between $\tau_e\tau_h$ and $\tau_\mu\tau_h$ channels. There is no uncertainty in 2018 due to the prefiring issue not being present.

Variations in the QCD scale result in a <1% uncertainty in VBF and VH production cross sections in addition to a 2.1% (1.9%, 1.3%) uncertainty in VBF (WH, ZH) production due to variations in the PDFs and α_s. The PDF+α_s uncertainty is 3.2% in ggH production while the QCD scale uncertainty is factored into nine shapes. These shapes account for things like migration between jet multiplicity bins due to QCD scale variations.

A flat uncertainty is assigned to the cross section for each background process. 4.2% for $t\bar{t}$, 5% for diboson, 5% for single top production, and 2% for Drell-Yan.

Uncertainty in the integrated luminosity results in a 2-3% effect in all simulated processes that is partially correlated between data periods. Similarly, the uncertainty in the $H \rightarrow$

Uncertainty	Implementation	Year Correlation (%)	Emb. Correlation (%)
τ_h energy scale	p_T and DM dependent	0	50
e $\to \tau_h$ energy scale	η and DM dependent	0	50
$\mu \to \tau_h$ energy scale	DM dependent	0	50
Electron energy scale	single shape	100	0
Muon energy scale	η dependent	100	0
Jet energy scale	6 grouped shapes	0-50	0
p_T^{miss} energy scale	single shape	0	0
τ_h ID	p_T dependent	0	50
τ_h ID against e	η dependent	0	50
τ_h ID against μ	η dependent	0	50
e ID	lnN - 15%	0	50
μ ID	lnN - 20%	0	50
Prefiring	single shape	100	0
STXS ggH theory	9 shapes	100	0
p_T^{miss} recoil correction	N(jet) dependent	0	0
Trigger Light Leg	2% per e or μ	0	0
Trigger Tau Leg	p_T dependent	0	0
b-jet veto	lnN - 0.5-5%	0	0
Luminosity	lnN - 2-3%	partial	0
B($H \to \tau\tau$)	lnN - XX%	100	0
Drell-Yan cross section	lnN - 2%	100	0
$t\bar{t}$ cross section	lnN - 4.2%	100	0
Diboson cross section	lnN - 5%	100	0
Single Top cross section	lnN - 5%	100	0

Table 13.1: *A summary of all systematics considered in this analysis.*

$\tau\bar{\tau}$ branching fraction is treated as a flat uncertainty that is fully correlated between data periods. The uncertainty is split into a 1.7% uncertainty from high-order corrections that are not included in the calculation along with <1% uncertainties due to the quark masses and the measurement of α_s.

The limited statistics available from simulation or data-driven estimation lead to statistical uncertainty in background and signal predictions. This is accounted for by a bin-by-bin uncertainty using the Barlow-Beeston approach. In essence, this approach allows the content of each bin in the final distributions to float and adds additional terms to the likelihood function quantifying the likelihood to measure the given content.

Group	Component(s)	Correlated
Absolute	AbsoluteMPFBias, AbsoluteScale, Fragmentation, PileUpDataMC, PileUpPtRef, RelativeFSR, SinglePionECAL, SinglePionHCAL	yes
Absolute Year	AbsoluteStat, RelativeStatFSR, TimePtEta	no
BBEC1	PileUpPtBB, PileUpPtEC1, RelativePtBB	yes
BBEC1 Year	RelativeJEREC1, RelativePtEC1, RelativeStatEC	no
EC2	PileUpPtEC2	yes
EC2 Year	RelativeJEREC2, RelativePtEC2	no
FlavorQCD	FlavorQCD	yes
HF	PileUpPtHF, RelativeJERHF, RelativePtHF	yes
HF Year	RelativeStatHF	no
RelativeBal	RelativeBal	yes
RelativeSample	RelativeSample (2017 and 2018)	no

Table 13.2: *Groupings of JES systematics based on JetMET POG recommendation. The correlated column tells whether the uncertainty is treated as correlated between data periods.*

Chapter 14

Results

For both analyses, the results are extracted using a 2D binned maximum likelihood fit. In order to reduce the dimensionality of our observables for the 2D fit, $\mathcal{D}_{NN}$ and $\mathcal{D}_{0-}^{VBF}$ are unrolled into a 1D observable. Fig. 14.1 provides an example of an unrolled distribution. This observable is combined with the remaining MELA discriminant to form the 2D distribution provided to the fit. The fit is performed by minimizing the test statistic Eq. 14.1 for each parameter of interest.

$$q(r) = -2\Delta \ln \mathcal{L} = -2\Delta \ln \frac{\mathcal{L}(data|s(r) + b, \theta_r)}{\mathcal{L}(data|s(\hat{r}) + b, \theta_{\hat{r}})} \tag{14.1}$$

In the test statistic, s and b are the signal and background distributions while r represents the best estimate of the signal parameters being profiled and $\hat{r}$ represents a freely floating value of the signal parameters. θ represents the best estimate of the nuisance parameters given a set of signal parameters, $\hat{r}$. The likelihood is the product over all bins used in the analysis of the likelihood:

$$\mathcal{L} = \prod_i f(data_i|s(r)_i + b_i) \cdot \mathcal{C}(\theta_i(r)) \tag{14.2}$$

where $\mathcal{C}(\theta_i(r))$ are the constraints per bin, i, from nuisance parameters, $\theta_i(r)$, and $f(\dots)$ represents the Poisson uncertainties derived for the data given the signal parameters. The

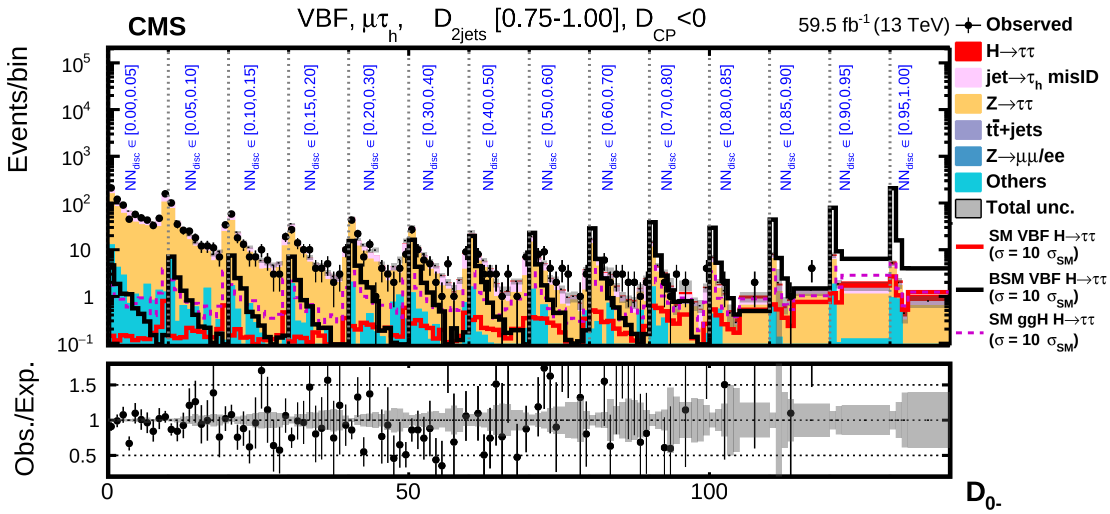

Figure 14.1: *An example of an unrolled distribution. This histogram shows how the 2D $\mathcal{D}_{NN}$ versus $\mathcal{D}_{0-}^{VBF}$ distribution is unrolled into a 1D distribution for the VBF category in the $\tau_\mu\tau_h$ channel using the 2018 data period. The distribution only contains events in which $\mathcal{D}_{\text{2jet}}^{\text{VBF}}$ is in the range $[0.75-1.]$ and $\mathcal{D}_{CP}^{VBF} < 0$. The blue text labels the value of $\mathcal{D}_{NN}$ between each vertical dashed line which shows the edge of each $\mathcal{D}_{NN}$. The bins within each region map to bins of $\mathcal{D}_{0-}^{VBF}$ within that $\mathcal{D}_{NN}$ bin.*

Poisson uncertainties are derived using the statistics of the given bin. Nuisance parameters are categorized as shape effects and normalization effects as described in Chapter 13. Normalization effects are modeled as a log-normal distribution centered at the expected value of the given process according to which the normalization is allowed to vary whereas the process's shape remains invariant. The shape of a given process is allowed to morph under the influence of a shape effect.

A scan over $\hat{r}$ is performed to determine the values that minimize the test statistic. To avoid introducing bias, the analysis is constructed initially without the use of data in sensitive regions. Expected limits, shown in Fig. 14.2 and Fig. 14.3, are calculated using only signal and background samples to estimate the sensitivity of the analysis. The parameter of interest is shown on the x-axis and the test statistic is shown on the y-axis. The location of minimum value of the test statistic on the x-axis corresponds to the best fit value for the parameter of interest. The dashed lines at $q(r) = 1$ and $q(r) = 3.84$ mark the one and two standard deviation regions. Points at which the test statistic exceeds the dashed lines corresponds to a point along the scan that can be ruled out at a 68% or 95% confidence level. Respectively, the sensitivity of the analysis can be inferred from the sharpness of the minimum.

In all cases, the expected best fit value corresponds to the effective cross section for each coupling being zero. This corresponds to the SM-only scenario indicating the data is not consistent with the presence of anomalous couplings. The sensitivity for each coupling scenario is found to be the highest in the $\tau_\mu\tau_h$ channel for the 2018 data period. This is expected because the analysis is statistics-limited, the 2018 period corresponds to the highest integrated luminosity, and the $\tau_\mu\tau_h$ channel has higher statistics than the $\tau_e\tau_h$ channel. Despite that, the 2017 period has larger statistics than 2016 data period, but the 2016 period is more sensitive due to detector conditions which decreased signal acceptance during 2017 data taking. The $\tau_\mu\tau_h$ channel is consistently more sensitive than the $\tau_e\tau_h$ channel, as expected.

Also, as expected, the sensitivity to the Hgg vertex is much lower than the HVV vertex. While the anomalous couplings in the HVV vertex can be excluded for $f_{a3} = 0.1$ at $> 2\sigma$ in data period 2018 for the $\tau_\mu\tau_h$ channel, anomalous couplings in the Hgg vertex at $f_{a3}^{ggH} = 1.0$ are still far from reaching the 1σ level for the same data.

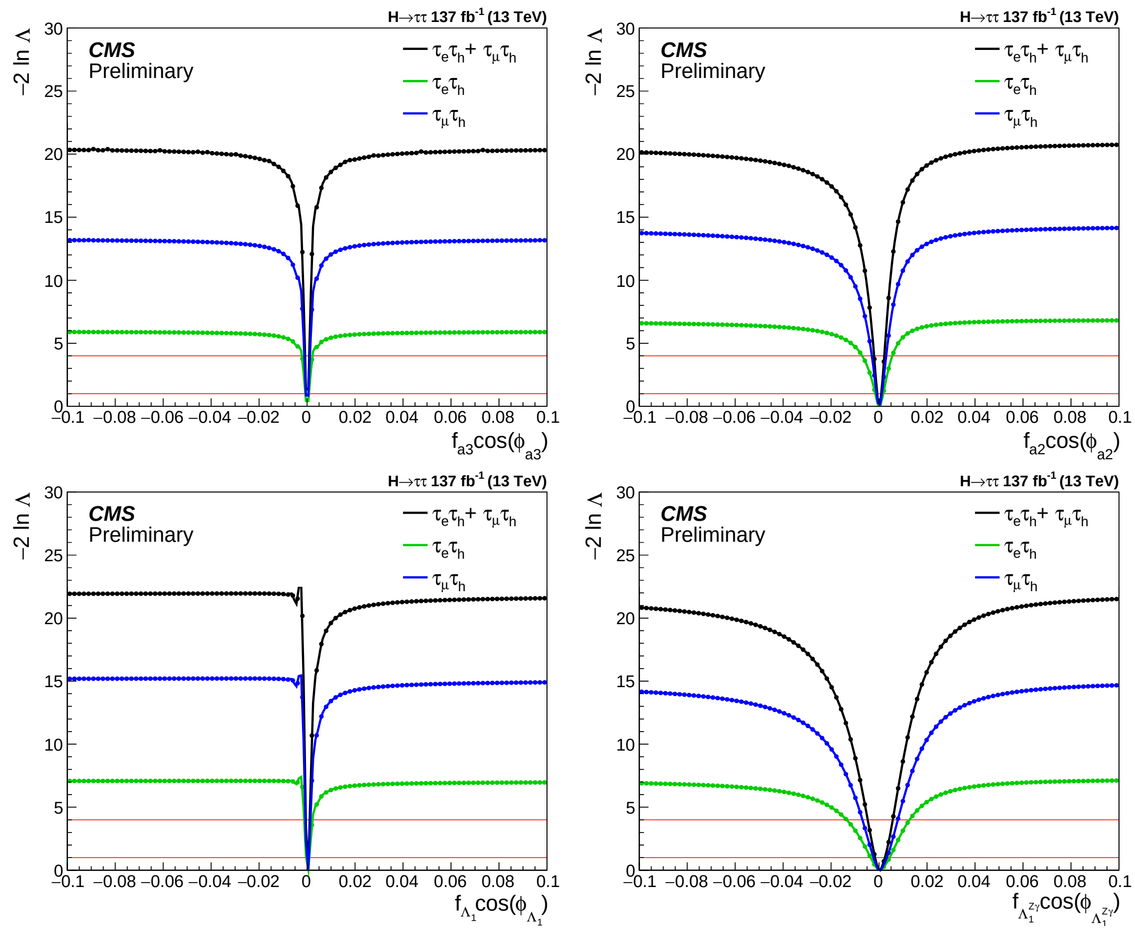

Figure 14.2: *The HVV expected likelihood scan over the parameter of interest f_{a3} (top left), f_{a2} (top right), $f_{\Lambda 1}$ (bottom left), and $f_{\Lambda 1}^{Z\gamma}$ (bottom right) are shown in all data periods. The $\tau_e\tau_h$ channel is shown in green, $\tau_\mu\tau_h$ is shown in blue, and the combination is shown in black.*

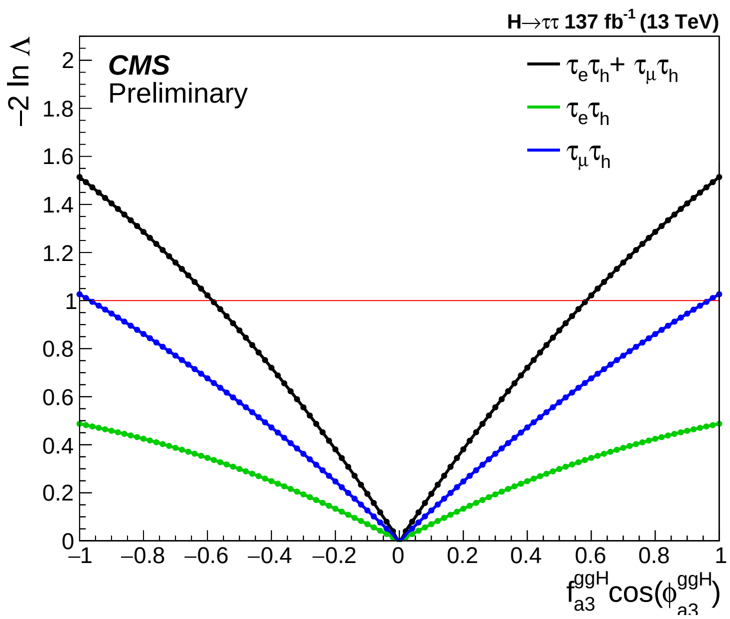

Figure 14.3: *The Hgg expected likelihood scans over f_{a3}^{ggH}. The $\tau_e\tau_h$ channel is shown in green, $\tau_\mu\tau_h$ is shown in blue, and the combination is shown in black.*

Chapter 15

Summary

I have presented a study of the Higgs couplings in the HVV and Hgg vertices using 158.7 fb^{-1} data collected at $\sqrt{s} = 13$ TeV by the CMS experiment. The study was conducted using the $H \to \tau\bar{\tau}$ decay mode, specifically where one tau lepton decays leptonically and the other decays hadronically.

Both studies utilize the correlation between jets produced in association with the Higgs boson to probe the couplings for CP-violation. The HVV vertex is also probed for anomalous CP-conserving couplings that result in correlations between jets. The matrix element likelihood approach (MELA) is used to optimally utilize the correlation between jets and construct discriminants to separate signal processes. Additionally, a neural network is trained to separate background processes from Higgs boson production allowing the MELA discriminants to perform in signal-enriched regions. The result is the most sensitive analysis of the HVV vertex in the $H \to \tau\bar{\tau}$ channel to date and the first study of the Hgg vertex using $H \to \tau\bar{\tau}$ events.

This analysis is combined with the other $H \to \tau\bar{\tau}$ decays to produce a full study of anomalous couplings using the $H \to \tau\bar{\tau}$ decay. In the future, the $H \to \tau\bar{\tau}$ channels will be added to the HZZ analysis to further constrain anomalous couplings in the HVV and Hgg vertices. As the Higgs boson's couplings are further probed, either the constraints on anomalous couplings will tighten to exclude the possibility of BSM physics in the coupling or anomalous effects will be observed opening the door for many BSM scenarios. Regardless the outcome, understanding the nature of the Higgs boson's coupling to gauge bosons is crucial to completing our understanding of fundamental physics.

Bibliography

[1] J. Ellis. Higgs physics. Technical report, July 2017. URL https://cds.cern.ch/record/1638469/.

[2] Yanyan Gao, Andrei V. Gritsan, Zijin Guo, Kirill Melnikov, Markus Schulze, and Nhan V. Tran. Spin determination of single-produced resonances at hadron colliders. *Phys. Rev. D*, 81:075022, 2010. doi: 10.1103/PhysRevD.81.075022.

[3] Ian Anderson, Sara Bolognesi, Fabrizio Caola, Yanyan Gao, Andrei V. Gritsan, Christopher B. Martin, Kirill Melnikov, Markus Schulze, Nhan V. Tran, Andrew Whitbeck, and Yaofu Zhou. Constraining anomalous HVV interactions at proton and lepton colliders. *Phys. Rev. D*, 89:035007, 2014. doi: 10.1103/PhysRevD.89.035007.

[4] CMS Collaboration. https://twiki.cern.ch/twiki/bin/view/cmspublic/lumipublicresults, Dec 2019.

[5] I. Neutelings. How to draw diagrams in latex with tikz. URL https://wiki.physik.uzh.ch/cms/latex:tikz.

[6] Tai Sakuma and Thomas McCauley. Detector and event visualization with SketchUp at the CMS experiment. *Journal of Physics: Conference Series*, 513(2):022032, jun 2014. doi: 10.1088/1742-6596/513/2/022032. URL https://doi.org/10.1088%2F1742-6596%2F513%2F2%2F022032.

[7] CMS Collaboration. Cms physics: Technical design report volume 1: Detector performance and software. Technical report, CERN, 2006. URL https://cds.cern.ch/record/922757.

[8] CMS Collaboration. Image of all ecal. URL https://cms-project-ecal-p5.web.cern.ch/images/ecal_all.jpeg.

[9] Andrea Benaglia. The cms ecal performance with examples. Technical Report CMS-CR-2013-430, CERN, Geneva, Nov 2013. URL https://cds.cern.ch/record/1632384.

[10] CMS Collaboration. Performance of the CMS hadron calorimeter with cosmic ray muons and LHC beam data. *Journal of Instrumentation*, 5(03):T03012–T03012, mar 2010. doi: 10.1088/1748-0221/5/03/t03012. URL https://doi.org/10.1088%2F1748-0221%2F5%2F03%2Ft03012.

[11] CMS Collaboration. Precise mapping of the magnetic field in the CMS barrel yoke using cosmic rays. *Journal of Instrumentation*, 5(03):T03021–T03021, mar 2010. doi: 10.1088/1748-0221/5/03/t03021. URL https://doi.org/10.1088%2F1748-0221%2F5%2F03%2Ft03021.

[12] CMS Collaboration. Performance of the cms muon detectors in early 2016 collision runs, 2016. URL https://twiki.cern.ch/twiki/bin/view/CMSPublic/MuonDPGPublic160729.

[13] Sirunyan Albert M. et al. An embedding technique to determine $\tau\tau$ backgrounds in proton-proton collision data. *Journal of Instrumentation*, 14(06):P06032–P06032, jun 2019. doi: 10.1088/1748-0221/14/06/p06032.

[14] P.A. Zyla et al. Review of Particle Physics. *PTEP*, 2020(8):083C01, 2020. doi: 10.1093/ptep/ptaa104.

[15] D. de Florian, C. Grojean, F. Maltoni, and et al. *Handbook of LHC Higgs Cross Sections: 4. Deciphering the Nature of the Higgs Sector*. CERN Yellow Reports: Monographs. Oct 2016. doi: 10.23731/CYRM-2017-002. URL https://cds.cern.ch/record/2227475. 869 pages, 295 figures, 248 tables and 1645 citations. Working Group web page: https://twiki.cern.ch/twiki/bin/view/LHCPhysics/LHCHXSWG.

[16] Georges Aad et al. Observation of a new particle in the search for the Standard Model Higgs boson with the ATLAS detector at the LHC. *Phys. Lett. B*, 716:1, 2012. doi: 10.1016/j.physletb.2012.08.020.

[17] Serguei Chatrchyan et al. Observation of a new boson at a mass of 125 GeV with the CMS experiment at the LHC. *Phys. Lett. B*, 716:30, 2012. doi: 10.1016/j.physletb.2012.08.021.

[18] Serguei Chatrchyan et al. Observation of a new boson with mass near 125 GeV in pp collisions at $\sqrt{s} = 7$ and 8 TeV. *JHEP*, 06:081, 2013. doi: 10.1007/JHEP06(2013)081.

[19] S. L. Glashow. Partial-symmetries of weak interactions. *Nucl. Phys.*, 22:579, 1961. doi: 10.1016/0029-5582(61)90469-2.

[20] F. Englert and R. Brout. Broken Symmetry and the Mass of Gauge Vector Mesons. *Phys. Rev. Lett.*, 13:321, 1964. doi: 10.1103/PhysRevLett.13.321.

[21] Peter W. Higgs. Broken symmetries, massless pARTICLEs and gauge fields. *Phys. Lett.*, 12:132, 1964. doi: 10.1016/0031-9163(64)91136-9.

[22] Peter W. Higgs. Broken symmetries and the masses of gauge bosons. *Phys. Rev. Lett.*, 13:508, 1964. doi: 10.1103/PhysRevLett.13.508.

[23] G. S. Guralnik, C. R. Hagen, and T. W. B. Kibble. Global conservation laws and massless particles. *Phys. Rev. Lett.*, 13:585, 1964. doi: 10.1103/PhysRevLett.13.585.

[24] Steven Weinberg. A model of leptons. *Phys. Rev. Lett.*, 19:1264, 1967. doi: 10.1103/PhysRevLett.19.1264.

[25] Abdus Salam. Weak and Electromagnetic Interactions. In *8th Nobel Symposium Lerum, Sweden, May 19-25, 1968*, volume C680519, pages 367–377, 1968.

[26] Serguei Chatrchyan et al. On the mass and spin-parity of the Higgs boson candidate via its decays to Z boson pairs. *Phys. Rev. Lett.*, 110:081803, 2013. doi: 10.1103/PhysRevLett.110.081803.

[27] Serguei Chatrchyan et al. Measurement of the properties of a Higgs boson in the four-lepton final state. *Phys. Rev. D*, 89:092007, 2014. doi: 10.1103/PhysRevD.89.092007.

[28] Vardan Khachatryan et al. Constraints on the spin-parity and anomalous HVV couplings of the Higgs boson in proton collisions at 7 and 8 TeV. *Phys. Rev. D*, 92:012004, 2015. doi: 10.1103/PhysRevD.92.012004.

[29] Vardan Khachatryan et al. Limits on the Higgs boson lifetime and width from its decay to four charged leptons. *Phys. Rev. D*, 92:072010, 2015. doi: 10.1103/PhysRevD.92.072010.

[30] Vardan Khachatryan et al. Combined search for anomalous pseudoscalar HVV couplings in VH(H $\to$ b$\bar{\text{b}}$) production and H $\to$ VV decay. *Phys. Lett. B*, 759:672, 2016. doi: 10.1016/j.physletb.2016.06.004.

[31] Albert M Sirunyan et al. Constraints on anomalous Higgs boson couplings using production and decay information in the four-lepton final state. *Phys. Lett. B*, 775:1, 2017. doi: 10.1016/j.physletb.2017.10.021.

[32] A.M. Sirunyan, A. Tumasyan, W. Adam, F. Ambrogi, E. Asilar, T. Bergauer, J. Brandstetter, M. Dragicevic, J. Erö, A. Escalante Del Valle, and et al. Measurements of the higgs boson width and anomalous hvv couplings from on-shell and off-shell production in the four-lepton final state. *Physical Review D*, 99(11), 2019. ISSN 2470-0029. doi: 10.1103/physrevd.99.112003. URL `http://dx.doi.org/10.1103/PhysRevD.99.112003`.

[33] Albert M Sirunyan et al. Constraints on anomalous HVV couplings from the production of Higgs boson decaying to τ lepton pairs. *Phys. Rev. D*, 100:112002, Dec 2019. doi: 10.1103/PhysRevD.100.112002. URL `https://link.aps.org/doi/10.1103/PhysRevD.100.112002`.

[34] Georges Aad et al. Study of the spin and parity of the Higgs boson in diboson decays with the ATLAS detector. *Eur. Phys. J. C*, 75:476, 2015. doi: 10.1140/epjc/s10052-015-3685-1.

[35] Albert M Sirunyan et al. Observation of the Higgs boson decay to a pair of τ leptons with the CMS detector. *Phys. Lett. B*, 779:283, 2018. doi: 10.1016/j.physletb.2018.02.004.

[36] Oliver Sim Brüning, Paul Collier, P Lebrun, Stephen Myers, Ranko Ostojic, John Poole, and Paul Proudlock. *LHC Design Report*. CERN Yellow Reports: Monographs. CERN, Geneva, 2004. doi: 10.5170/CERN-2004-003-V-1. URL https://cds.cern.ch/record/782076.

[37] CERN. The cern accelerator complex complexe des accélérateurs du cern. Technical report, Dec. 2008. URL https://cds.cern.ch/record/1260465.

[38] CERN. Linear accelerator 2. Technical report, Dec. 2019. URL https://cds.cern.ch/record/1260465.

[39] CERN. The proton synchrotron booster. Technical report, Dec. 2019. URL https://cds.cern.ch/record/1260465.

[40] CERN. The proton synchrotron. Technical report, Dec. 2019. URL https://cds.cern.ch/record/1260465.

[41] CERN. The super proton synchrotron. Technical report, Dec. 2019. URL https://cds.cern.ch/record/1260465.

[42] CMS Collaboration. CMS technical design report, volume II: Physics performance. *J.Phys.G*, 34:995, 2007. doi: 10.1088/0954-3899/34/6/S01.

[43] CMS Collaboration. Technical proposal for the upgrade of the CMS detector through 2020. Technical Report CERN-LHCC-2011-006. LHCC-P-004, Jun 2011. URL https://cds.cern.ch/record/1355706.

[44] J Mans, J Anderson, B Dahmes, P de Barbaro, J Freeman, T Grassi, E Hazen, J Mans, R Ruchti, I Schimdt, T Shaw, C Tully, J Whitmore, and T Yetkin. CMS Technical Design Report for the Phase 1 Upgrade of the Hadron Calorimeter. Technical Report CERN-LHCC-2012-015. CMS-TDR-10, Sep 2012. URL https://cds.cern.ch/record/1481837. Additional contact persons: Jeffrey Spalding, Fermilab, spalding@cern.ch, Didier Contardo, Universite Claude Bernard-Lyon I, contardo@cern.ch.

[45] A Dominguez, D Abbaneo, K Arndt, N Bacchetta, A Ball, E Bartz, W Bertl, G M Bilei, G Bolla, H W K Cheung, M Chertok, S Costa, N Demaria, Daniel Dominguez Vazquez, K Ecklund, W Erdmann, K Gill, G Hall, K Harder, F Hartmann, R Horisberger, W Johns, H C Kaestli, K Klein, D Kotlinski, S Kwan, M Pesaresi, H Postema, T Rohe, C Schäfer, A Starodumov, S Streuli, A Tricomi, P Tropea, J Troska, F Vasey, and W Zeuner. CMS Technical Design Report for the Pixel Detector Upgrade. Technical Report CERN-LHCC-2012-016. CMS-TDR-11, Sep 2012. URL https://cds.cern.ch/record/1481838. Additional contacts: Jeffrey Spalding, Fermilab, Jeffrey.Spalding@cern.ch Didier Contardo, Universite Claude Bernard-Lyon I, didier.claude.contardo@cern.ch.

[46] A Tapper and Darin Acosta. CMS Technical Design Report for the Level-1 Trigger Upgrade. Technical Report CERN-LHCC-2013-011. CMS-TDR-12, Jun 2013. URL https://cds.cern.ch/record/1556311. Additional contacts: Jeffrey Spalding, Fermilab, Jeffrey.Spalding@cern.ch Didier Contardo, Universite Claude Bernard-Lyon I, didier.claude.contardo@cern.ch.

[47] S. Chatrchyan et al. The CMS experiment at the CERN LHC. *JINST*, 3:S08004, 2008. doi: 10.1088/1748-0221/3/08/S08004.

[48] Vardan Khachatryan et al. The CMS trigger system. *JINST*, 12:P01020, 2017. doi: 10.1088/1748-0221/12/01/P01020.

[49] Albert M. Sirunyan et al. PARTICLE-flow reconstruction and global event description with the CMS detector. *JINST*, 12:P10003, 2017. doi: 10.1088/1748-0221/12/10/P10003.

[50] R. Frühwirth. Application of Kalman filtering to track and vertex fitting. *Nucl. Instrum. Meth. A*, 262:444, 1987. doi: 10.1016/0168-9002(87)90887-4.

[51] S. Baffioni et al. Electron reconstruction in CMS. *Eur. Phys. J. C*, 49:1099, 2007. doi: 10.1140/epjc/s10052-006-0175-5.

[52] Vardan Khachatryan et al. Performance of electron reconstruction and selection with the CMS detector in proton-proton collisions at $\sqrt{s} = 8$ TeV. *JINST*, 10:P06005, 2015. doi: 10.1088/1748-0221/10/06/P06005.

[53] Albert M. Sirunyan et al. Performance of the CMS muon detector and muon reconstruction with proton-proton collisons at $\sqrt{s} = 13$ TeV. *JINST*, 13:P06015, 2018. doi: 10.1088/1748-0221/13/06/P06015.

[54] Serguei Chatrchyan et al. Performance of CMS muon reconstruction in pp collision events at $\sqrt{s} = 7$ TeV. *JINST*, 7:P10002, 2012. doi: 10.1088/1748-0221/7/10/P10002.

[55] CMS Collaboration et al. Performance of tau-lepton reconstruction and identification in CMS. *JINST*, 7:P01001, 2012. doi: 10.1088/1748-0221/7/01/P01001.

[56] Vardan Khachatryan et al. Reconstruction and identification of τ lepton decays to hadrons and ν_τ at CMS. *JINST*, 11:P01019, 2016. doi: 10.1088/1748-0221/11/01/P01019.

[57] A. M. Sirunyan et al. Performance of reconstruction and identification of τ leptons decaying to hadrons and ν_τ in pp collisions at $\sqrt{s} = 13$ TeV. *JINST*, 13:P10005, 2018. doi: 10.1088/1748-0221/13/10/P10005.

[58] CMS Collaboration. Performance of the deeptau algorithm for the discrimination of taus against jets, electron, and muons. CMS Physics Analysis Summary CMS-DP-2019-033, 2019. URL https://cds.cern.ch/record/2694158.

[59] Matteo Cacciari, Gavin P. Salam, and Gregory Soyez. The anti-k_t jet clustering algorithm. *JHEP*, 04:063, 2008. doi: 10.1088/1126-6708/2008/04/063.

[60] M. Cacciari, G. P. Salam. Dispelling the N^3 myth for the k_t jet-finder. *Phys. Lett. B*, 641:57, 2006. doi: 10.1016/j.physletb.2006.08.037.

[61] Matteo Cacciari, Gavin P. Salam, and Gregory Soyez. FastJet user manual. *Eur. Phys. J. C*, 72:1896, 2012. doi: 10.1140/epjc/s10052-012-1896-2.

[62] M. Cacciari, G. P. Salam, G. Soyez. Fastjet user manual. 2011.

[63] Matteo Cacciari and Gavin P. Salam. Pileup subtraction using jet areas. *Phys. Lett. B*, 659:119, 2008. doi: 10.1016/j.physletb.2007.09.077.

[64] Matteo Cacciari, Gavin P. Salam, and Gregory Soyez. The Catchment Area of Jets. *JHEP*, 04:005, 2008. doi: 10.1088/1126-6708/2008/04/005.

[65] A. M. Sirunyan et al. Identification of heavy-flavour jets with the CMS detector in pp collisions at 13 TeV. *JINST*, 13:P05011, 2018. doi: 10.1088/1748-0221/13/05/P05011.

[66] CMS Collaboration. Performance of missing transverse momentum in pp collisions at $\sqrt{s}$ = 13 TeV using the CMS detector. CMS Physics Analysis Summary CMS-PAS-JME-17-001, 2018. URL http://cds.cern.ch/record/2628600?ln=en.

[67] A. M. Sirunyan, A. Tumasyan, W. Adam, F. Ambrogi, E. Asilar, T. Bergauer, J. Brandstetter, E. Brondolin, M. Dragicevic, and et al. Measurement of the $Z/\gamma^* \to \tau\tau$ cross section in pp collisions at $\sqrt{s} = 13$ TeV and validation of τ lepton analysis techniques. *The European Physical Journal C*, 78(9), Sep 2018. ISSN 1434-6052. doi: 10.1140/epjc/s10052-018-6146-9. URL http://dx.doi.org/10.1140/epjc/s10052-018-6146-9.

[68] Torbjorn Sjostrand, Stefan Ask, Jesper R. Christiansen, Richard Corke, Nishita Desai, Philip Ilten, Stephen Mrenna, Stefan Prestel, Christine O. Rasmussen, and Peter Z. Skands. An introduction to PYTHIA 8.2. *Comput. Phys. Commun.*, 191:159, 2015. doi: 10.1016/j.cpc.2015.01.024.

[69] Torbjörn Sjöstrand, Stephen Mrenna, and Peter Skands. PYTHIA 6.4 physics and manual. *JHEP*, 05:026, 2006. doi: 10.1088/1126-6708/2006/05/026.

[70] Vardan Khachatryan et al. Event generator tunes obtained from underlying event and multiparton scattering measurements. *Eur. Phys. J. C*, 76:155, 2016. doi: 10.1140/epjc/s10052-016-3988-x.

[71] Richard D. Ball, Valerio Bertone, Francesco Cerutti, Luigi Del Debbio, Stefano Forte, Alberto Guffanti, Jose I. Latorre, Juan Rojo, and Maria Ubiali. Unbiased global determination of parton distributions and their uncertainties at NNLO and at LO. *Nucl. Phys. B*, 855:153, 2012. doi: 10.1016/j.nuclphysb.2011.09.024.

[72] R. D. Ball, L. Del Debbio, S. Forte, A. Guffanti, J. I. Latorre, J. Rojo and M. Ubiali. A first unbiased global NLO determination of parton distributions and their uncertainties. *Nucl. Phys*, B(838):136, 2010.

[73] Sirunyan Albert M. et al. Extraction and validation of a new set of cms pythia8 tunes from underlying-event measurements. *Eur. Phys. J. C*, 80:4, 2020. doi: 10.1140/epjc/s10052-019-7499-4.

[74] S. Agostinelli et al. GEANT4—a simulation toolkit. *Nucl. Instrum. Meth. A*, 506:250, 2003. doi: 10.1016/S0168-9002(03)01368-8.

[75] J. Alwall, Michel Herquet, Fabio Maltoni, Olivier Mattelaer, and Tim Stelzer. MadGraph 5: going beyond. *JHEP*, 06:128, 2011. doi: 10.1007/JHEP06(2011)128.

[76] Johan Alwall et al. MadGraph/MadEvent v4: The New Web Generation. *JHEP*, 09:028, 2007. doi: 10.1088/1126-6708/2007/09/028.

[77] Gionata Luisoni, Paolo Nason, Carlo Oleari, and Francesco Tramontano. $HW^{\pm}$/HZ + 0 and 1 jet at NLO with the POWHEG BOX interfaced to GoSam and their merging within MiNLO. *JHEP*, 10:083, 2013. doi: 10.1007/JHEP10(2013)083.

[78] E. Bagnaschi, G. Degrassi, P. Slavich, and A. Vicini. Higgs production via gluon fusion in the POWHEG approach in the SM and in the MSSM. *JHEP*, 02:088, 2012. doi: 10.1007/JHEP02(2012)088.

[79] Stefano Frixione, Paolo Nason, and Carlo Oleari. Matching NLO QCD computations with parton shower simulations: the POWHEG method. *JHEP*, 11:070, 2007. doi: 10.1088/1126-6708/2007/11/070.

[80] Paolo Nason and Carlo Oleari. NLO Higgs boson production via vector-boson fusion matched with shower in POWHEG. *JHEP*, 02:037, 2010. doi: 10.1007/JHEP02(2010)037.

[81] Andrei V. Gritsan, Jeffrey Roskes, Ulascan Sarica, Markus Schulze, Meng Xiao, and Yaofu Zhou. New features in the JHU generator framework: constraining Higgs boson properties from on-shell and off-shell production. 2020.

[82] Sara Bolognesi, Yanyan Gao, Andrei V. Gritsan, Kirill Melnikov, Markus Schulze, Nhan V. Tran, and Andrew Whitbeck. Spin and parity of a single-produced resonance at the LHC. *Phys. Rev. D*, 86:095031, 2012. doi: 10.1103/PhysRevD.86.095031.

[83] Andrei V. Gritsan, Raoul Röntsch, Markus Schulze, and Meng Xiao. Constraining anomalous Higgs boson couplings to the heavy flavor fermions using matrix element techniques. *Phys. Rev. D*, 94:055023, 2016. doi: 10.1103/PhysRevD.94.055023.

[84] V. Ravindran, J. Smith, and W. L. van Neerven. NNLO corrections to the total cross section for Higgs boson production in hadron-hadron collisions. *Nucl. Phys. B*, 665:325, 2003. doi: 10.1016/S0550-3213(03)00457-7.

[85] Robert V. Harlander and William B. Kilgore. Next-to-next-to-leading order Higgs production at hadron colliders. *Phys. Rev. Lett.*, 88:201801, 2002. doi: 10.1103/PhysRevLett.88.201801.

[86] Charalampos Anastasiou and Kirill Melnikov. Higgs boson production at hadron colliders in NNLO QCD. *Nucl. Phys. B*, 646:220, 2002. doi: 10.1016/S0550-3213(02)00837-4.

[87] Lorenzo Bianchini, John Conway, Evan Klose Friis, and Christian Veelken. Reconstruction of the Higgs mass in $H \to \tau\tau$ events by dynamical likelihood techniques. *J. Phys. Conf. Ser.*, 513:022035, 2014. doi: 10.1088/1742-6596/513/2/022035.

[88] François Chollet et al. Keras. https://keras.io, 2015.